



Balkan Journal of Electrical & Computer Engineering

An International Peer Reviewed, Referred, Indexed and Open Access Journal

www.bajece.com

Vol : 5
No : 2
Year : 2017
ISSN : 2147 - 284X



This journal is supported by the Istanbul Technical University. It is abstracted and indexed in, Index Google Scholarship, the PSCR, Cross ref, DOAJ, Research Bible, Indian Open Access Journals (OAJ), Institutional Repositories (IR), J-Gate (Informatics India), Ulrich's, International Society of Universal Research in Sciences, DRJI, EyeSource, Cosmos Impact Factor, Cite Factor, SIS Scientific Indexing Service, IJIF, iiiFactor.



General Publication Director & Editor-in-Chief
Ş.Serhat Seker, Istanbul Technical University, Turkey

Associate Editors

Abdoulkader Ibrahim Idriss, University of Djibouti, Djibouti
Amir Tokić, University of Tuzla, Bosnia and Herzegovina
Tahir Çetin Akıncı, Istanbul Technical University, Turkey
Veselina Nedeva, Trakia University, Bulgaria

Scientific Committee

Abhishek Shukla (India)
Abraham Lomi (Indonesia)
Aleksandar Georgiev (Bulgaria)
Arunas Lipnickas (Lithuania)
Audrius Senulis (Lithuania)
Belle R. Upadhyaya (USA)
Brijender Kahanwal (India)
Chandar Kumar Chanda (India)
Daniela Dzhonova-Atanasova (Bulgaria)
Deris Stiawan (Indonesia)
Emel Onal (Turkey)
Emine Ayaz (Turkey)
Enver Hatimi (Kosovo)
Ferhat Sahin (USA)
Gursel Alici (Australia)
Hakan Temeltaş (Turkey)
Ibrahim Akduman (Turkey)
Jan Izykowski (Poland)
Javier Bilbao Landatxe (Spain)
Jelena Dikun (Lithuania)
Karol Kyslan (Slovakia)
Kunihiko Nabeshima (Japan)
Lambros Ekonomou (Greece)
Lazhar Rahmani (Algerie)
Marcel Istrate (Romania)
Marija Eidukeviciute (Lithuania)
Milena Lazarova (Bulgaria)
Muhammad Hadi (Australia)
Muhamed Turkanović (Slovenia)
Mourad Houabes (Algerie)
Murari Mohan Saha (Sweden)
Nick Papanikolaou (Greece)
Okyay Kaynak (Turkey)
Osman Nuri Ucan (Turkey)
Ozgur E. Mustecaplioglu (Turkey)
Padmanaban Sanjeevikumar (India)
Ramazan Caglar (Turkey)
Rumen Popov (Bulgaria)
Tarek Bouktir (Algeria)
Sead Berberovic (Croatia)
Seta Bogosyan (USA)
Savvas G. Vassiliadis (Greece)
Suwarno (Indonesia)
Tulay Adali (USA)
Yogeshwarsing Calleecharan (Mauritius)
YangQuan Chen (USA)
Youcef Soufi (Algeria)

Aim & Scope

The journal publishes original papers in the extensive field of Electrical-Electronics and Computer engineering. It accepts contributions which are fundamental for the development of electrical engineering, computer engineering and its applications, including overlaps to physics. Manuscripts on both theoretical and experimental work are welcome. Review articles and letters to the editors are also included.

Application areas include (but are not limited to): Electrical & Electronics Engineering, Computer Engineering, Software Engineering, Biomedical Engineering, Electrical Power Engineering, Control Engineering, Signal and Image Processing, Communications & Networking, Sensors, Actuators, Remote Sensing, Consumer Electronics, Fiber-Optics, Radar and Sonar Systems, Artificial Intelligence and its applications, Expert Systems, Medical Imaging, Biomedical Analysis and its applications, Computer Vision, Pattern Recognition, Robotics, Industrial Automation.



ISSN: 2147- 284X
Vol: 5
No : 2
Year: September 2017

CONTENTS

A. Bosakova-Ardenska, One Approach for Parallel Algorithms Representation, **30-33**

H. Ozkan, Rapid Diagnostic Lateral Flow Strip Test Reader,**34-39**

E. Oguz, Y. Oğuz and H.Çimen, Simulation and Power Flow Control Using Switching's Method of Isolated Wind-Solar Hybrid Power Generation System with Battery Storage,**40-49**

B. Fincan, M. Yilmaz, A. Goynusen, and K. Erenay, Design and Optimization of a High Power Density and Efficiency Boost PFC,..... **50-59**

D. Taskin, Design of Bluetooth Low Energy Based Indoor Positioning System,**60-65**

F. Bulut, and S. Osmani, Scene Change Detection using Different Color Pallets and Performance Comparison,**66-72**

M. Aydın, and G. Erdemir, An Object Detection and Identification System for a Mobile Robot Control,**73-76**

J. A. Corea-Araujo, G. Guerra, J. A. Martínez-Velasco, and F. González-Molina, Generation of Bifurcation Diagrams for Ferroresonance Characterization Using Parallel Computing,.....**77-85**

B.B. Alagoz, A Note on Commensurate-Order Characteristic Root Equivalency Class of Linear Time Invariant Systems,**86-96**

O. Ülker, G. Gökmen and E. Kaplanoğlu, Emg Signal Classification Using Fuzzy Logic, **97-101**

**BALKAN
JOURNAL OF
ELECTRICAL & COMPUTER ENGINEERING**
(An International Peer Reviewed, Indexed and Open Access Journal)

Contact

Istanbul Technical University
Department of Electrical Engineering
Ayazaga Campus, Maslak, Istanbul-Turkey

Web: <https://www.bajece.com>
<http://dergipark.gov.tr/bajece>
e-mail: editor@bajece.com

One Approach for Parallel Algorithms Representation

A. Bosakova-Ardenska


Abstract— This paper presents one approach for parallel algorithms representation. The proposed model is practice oriented and its name is AMPA (Agenda Model for Parallel Algorithms) due to basic blocks organization like a schedule. The model uses classical Master/Slave paradigm. One parallel merge sorting algorithm based on quick sort is presented with the discussed AMPA model and also three known representation approaches (description with natural language, pseudo code and PRAM). A survey of professional opinion about AMPA and other approaches is conducted. The results show that most of the interviewed people choose AMPA as the best way to understand the algorithm.

Index Terms— Master-slave, Merge sort, Parallel algorithms, PRAM, Programming model, Pseudo code, Quicksort.

I. INTRODUCTION

DURING THE LAST YEARS the parallel programming becomes one of the most popular techniques in application development. Development of processors architectures (SoC and Multi-core architectures) leads to significant advancement in software technologies. The possibilities lot of us to have multi processors on a small chip leads to the development of parallel applications which could effectively use these hardware resources. The scientific evolution also needs of computational resources and effective parallel programs. The complexity of software also increases and this is the reason that new usage models for program design are wanted. Some new parallel programming models for specific multi-thread architectures were designed to last year's [1,2,3]. They are useful for designing parallel algorithms for specific architectures like NVidia GPU.

The main idea behind this research is to be proposed a practice oriented high-level model for parallel algorithms representation. The proposed model uses well known Master/Slave paradigm.

A.BOSAKOVA-ARDENSKA is with Department of Computer Systems and Technologies University of Food Technologies, Plovdiv, Bulgaria (e-mail: a_bosakova@uft-plovdiv.bg) 

Manuscript received March 3, 2017; accepted June 26, 2017.
DOI: [10.17694/bajece.334294](https://doi.org/10.17694/bajece.334294)

II. AGENDA MODEL FOR PARALLEL ALGORITHMS (AMPA)

AMPA is a simple to practice oriented model for parallel algorithm representation. The name is Agenda Model for Parallel Algorithms due to its structure. According to this model, there are 6 basic elements and traditional Master/Slave code organization logic. The Master/Slave code organization logic is a variant of SPMD (Single Program Multiple Data) models which are successfully applied in parallel algorithms developing [4, 5, 6, 7, 8, 9, 10, 11, 12, 13, 14, 15, 16]. The operations are located in their exact positions depends on parallel execution. This organization is like a schedule and that is the reason for the name Agenda in AMPA.

The AMPA defines two types of processes- Master and Slave. Master is always one but Slaves are many. The model consists of six graphical elements:

- 1) Process block (Master or Slave). If the algorithm contains only Master process this is not a parallel algorithm;
- 2) Operation block – this block contains some operations: calculations or data exchanging;
- 3) Vertical arrow – this is a line which presents execution's flow in one process;
- 4) Horizontal arrow – this is a line which presents communications among processes;
- 5) Execution type block – this is block which groups other blocks to point sequential or parallel execution part;
- 6) Parallel steps block – this block groups other blocks whose parallel execution has to be repeated and it shows how many times the execution will be repeated.

The blocks of Master and Slave processes are situated in parallel lines. If two blocks of Master and Slave processes are at the same level, this means that these operations could be executed simultaneously. I.e. the position of every block shows when the block could be executed. Figure 1 shows an example of the parallel algorithm presented with AMPA.

Execution type blocks and Parallel steps block are drawn with dashed line. The AMPA model could be applied for multi-thread application. In this case:

- the Master process is “Process” but “Slave” processes are implemented as threads;
- horizontal arrows will be replaced with “read/write global data” (i.e. threads will work with data of its own process).

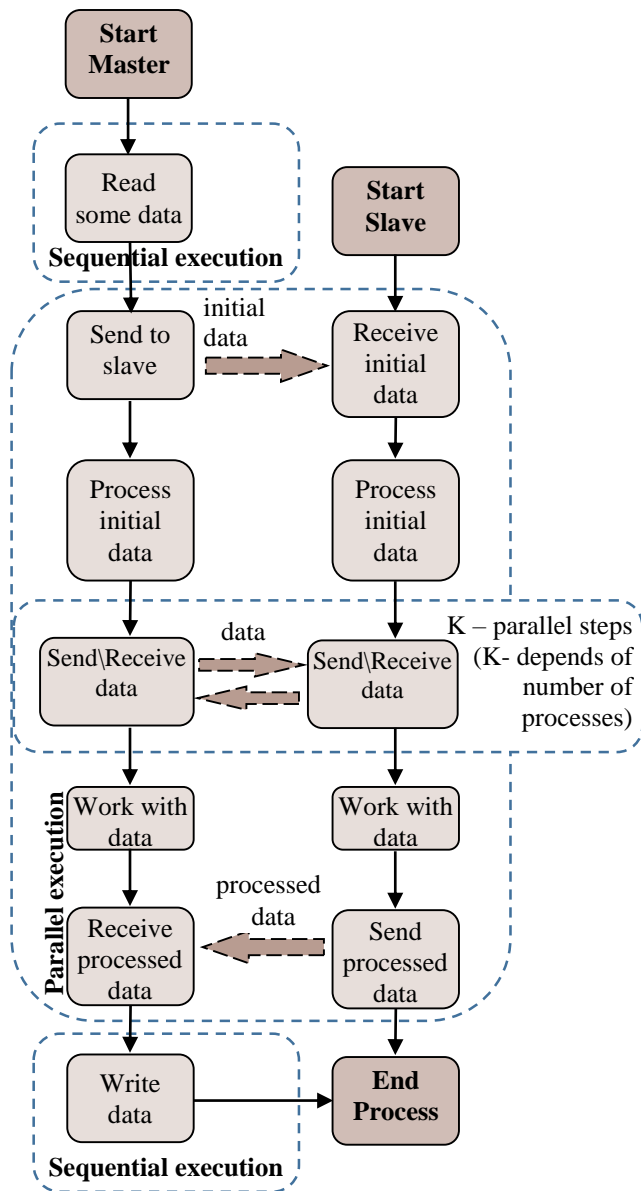


Fig.1. Sample algorithm presented with AMPA

III. APPLICATION OF AMPA

Parallel merge sort uses a “divide and conquers” approach and data distribution maps into a binary tree [6]. Data are divided into sub-lists and the process continues while lists reach size one. The proposed model is used for the representation of one modification of parallel merge sort algorithm. This modification uses quicksort algorithm [17] to sort sub-lists. The number of sub-lists is equal to the number of parallel processes (processors). The sub-lists are the same size. After their sorting with quicksort sub-lists are merged. The next figures (fig. 2, fig. 3, fig. 4 and fig. 5) present this algorithm using respectively a description of the natural language, pseudo code, PRAM model [18] and proposed AMPA model.

The numbers that need to be sorted are distributed equally to the parallel processes (processors). Each process sorts its part of the numbers using the quicksort algorithm. Finally, the sorted parts are merged.

Fig.2. Parallel merge sort – described by natural language

```

for i=1 to M-1 do in parallel
  myarr <= P0 (arr[i*n/m])
  qsort(myarr)
  merge (myarr => P0 (arr[i*n/m]))
end parallel
    
```

Fig.3. Parallel merge sort – described by pseudo code

```

begin
  global read(arr[i*n/m], myarr);
  qsort(myarr);
  merge (global write(myarr, arr[i*n/m]))
end
    
```

Fig.4. Parallel merge sort – described by PRAM

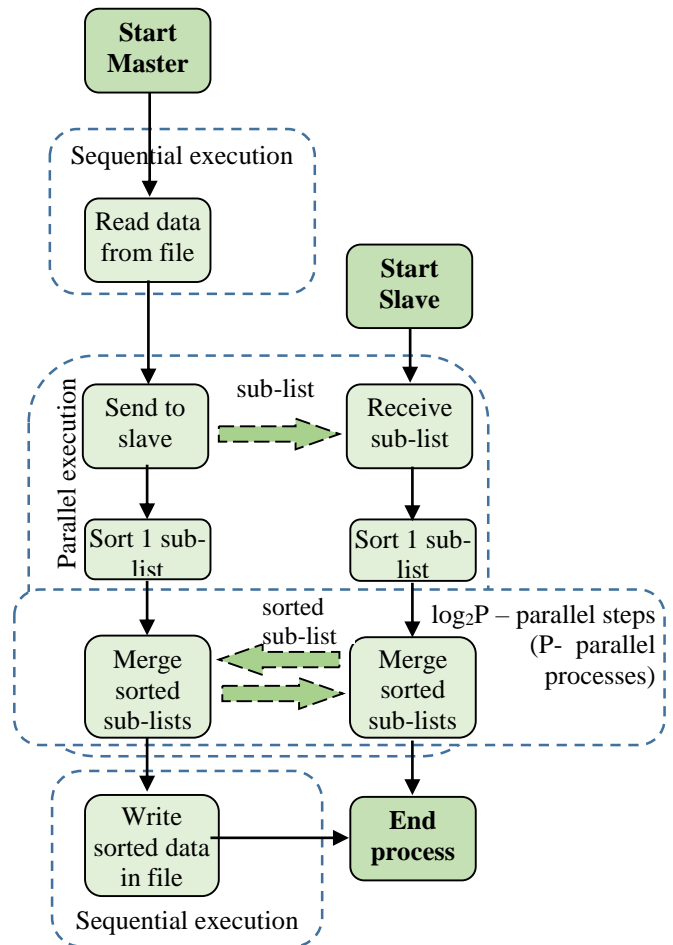


Fig.5. Parallel merge sort – AMPA described

The variables and operations which are used in fig. 3 and fig. 4 are:

- M – number of parallel processes (processors);
- N – size of the array for sorting (count of all numbers);
- arr – array for sorting;
- myarr – local array for sub-list;
- global read() – operation for global memory reading;
- global write() – operation for global memory writing;
- => and <= - operations for data reading/writing.

The main assumption for pseudo code description is that unsorted array belongs to process (processor) P0. The main assumption for PRAM description is that unsorted array is allocated into global memory.

The number of merge operations is equal to $\log_2 P$, where P is a number of parallel processes, i.e. the number of sub-lists. This means that after first merge operation the number of processors which execute merge operation will decrease twice. For example:

P = 8, number of parallel merge operations = 3

1 parallel merge operation: 4 processes will receive sorted sub-lists of other 4 processes and will execute merge operation;

2 parallel merge operation: 2 processes will receive sorted sub-lists of other 2 processes and will execute merge operation;

3 parallel merge operation: 1 process will receive sorted sub-lists of other process and will execute merge operation. After this step, a final sorted list will be reached.

IV. RESULTS

Discussed parallel sorting algorithm and its four representations are used for the short survey of opinion among:
 - students which study course Supercomputers, part of Computer Systems and Technologies speciality at University of Food Technologies, Plovdiv (Bulgaria);

Centre for Supercomputing Applications) in assistance with
 - participants of training school “Practical Programming Models and Skills on INTEL Xeon Phi for Scientific Research

Engineers”. This course was organized by NCSA (National Science and Technology Facilities Council (STFC) and Bayncore (U.K.).

More than fourteen people were included in the survey. The questions listed in current survey are:

- 1) Which of the four representations of the parallel algorithm helps you best to understand its idea?
 - (a) Description with natural language
 - (b) pseudo code
 - (c) PRAM
 - (d) AMPA
- 2) Which of the models for presentation of the parallel algorithm would you use if you need to implement it? Why?

The figures six and seven present results of the survey. Some of the answers to question “Why?” of question 2 (Which of the models for presentation of the parallel algorithm would you use if you need to implement it? Why?) are presented in Table 1.

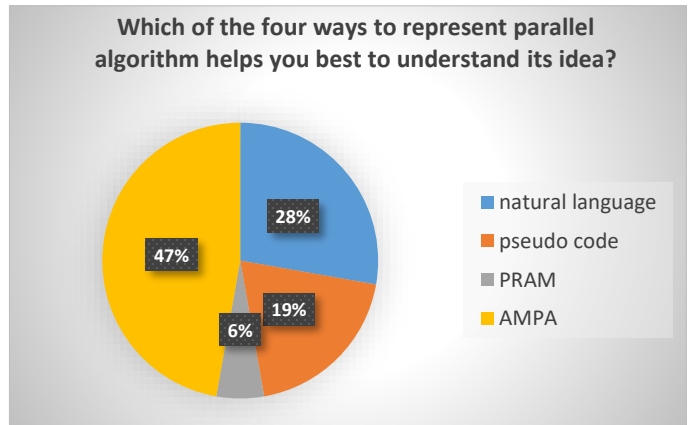


Fig.6 Results for question 1 of conducted survey

TABLE I.
PREFERRED MODEL FOR IMPLEMENTATION

Preferred model for implementation	Reasons
Natural language	This representation tells me just what needs to be done.
pseudo code	This representation is most understandable for me.
	This representation is “universal” code and could be used as a basic for a parallel program.
	This representation is shortest and clearly described.
PRAM	The source code in this representation could be used for the skeleton of a program.
	This representation is short.
AMPA	This representation is the best for idea understanding.
	The detailed description of the parallel algorithm is suitable for its precise implementation.
	This model gives a good visual idea and thus it will decrease the count of the logical errors in implementation.

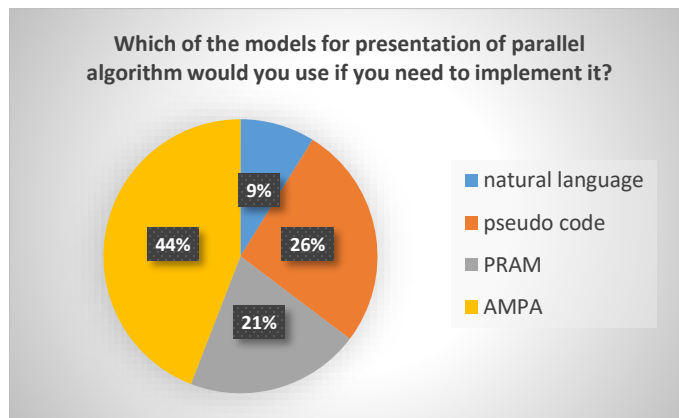


Fig.7. Results for question 2 of conducted survey

V. CONCLUSIONS AND FUTURE WORK

A novel approach for parallel algorithms representation with graphical elements is presented in this paper. One parallel merge sort algorithm is described using natural language, pseudo code, PRAM and AMPA. These four presentations were evaluated by students and participants of professional course for parallel programming. The results show that:

- Preferred model is AMPA because it gives is good visual idea about algorithm (47% of interviewed people choose AMPA as the best way to understand the algorithm);
- When the algorithm has to be implemented the AMPA and pseudo code models are most preferred (44%- AMPA and 26%- pseudo code).

In the future, the research will continue with developing a software tool for AMPA modelling. This tool will facilitate the use of the model.

ACKNOWLEDGMENT

The author would like to thanks to NCSA and Prof. Stoyan Markov for their assistance in the survey of opinions about the proposed model.

REFERENCES

- [1] Kirtzic J. S., O. Daescu, A parallel algorithm development model for the GPU architecture, Proc. of International Conference on Parallel and Distributed Processing Techniques and Applications (PDPTA), 2012
- [2] Valiant L., A bridging model for multi-core computing, Journal of Computer and System Sciences, vol. 77, no. 1, pp. 154–166, 2011.
- [3] Luebke D., CUDA: Scalable parallel programming for high-performance scientific computing, 5th IEEE International Symposium on Biomedical Imaging: From Nano to Macro, Paris, pp. 836-838, 2008
- [4] Yukiya Aoyama, Jun Nakano, "RS/6000 SP: Practical MPI Programming", International Technical Support Organization, IBM, 1999

- [5] Seyed H. Roosta, Parallel Processing and Parallel Algorithms: theory and computation, Springer, ISBN 0-387-98716-9, 2000
- [6] Wilkinson B. and Allen M., Sorting Algorithms, Parallel Programming: Techniques and Applications Using Networked Workstations and Parallel Computers, Prentice-Hall, 1999
- [7] Sahni S. and G. Vairaktarakis, The master-slave paradigm in parallel computer and industrial settings, Journal of Global Optimization, 9, pp. 357–377, 1996
- [8] Baldo L., L. Brenner, L. G. Fernandes, P. Fernandes, A. Sales, Performance Models For Master/Slave Parallel Programs, Electronic Notes in Theoretical Computer Science, 2004
- [9] Mostaghim S., J. Branke, A. Lewis, H. Schneck, Parallel Multi-objective Optimization using Master-Slave Model on Heterogeneous Resources, Proceedings of the IEEE Congress on Evolutionary Computation, 2008
- [10] Cazenave T., Nicolas Jouandea, A Parallel Monte-Carlo Tree Search Algorithm, Computers and Games, 2008
- [11] Shuping LIU, Yanliu CHENG, The Design and Implementation of MPI Master-Slave Parallel Genetic Algorithm, International Conference on Education Technology and Computer (ICETC2012), 2012
- [12] Depolli M., R. Trobec, B. Filipi'c, Asynchronous Master-Slave Parallelization of Differential Evolution for Multiobjective Optimization, Evolutionary Computation 21 (2), pp. 261–291, 2013
- [13] Krichene H., M. Baklouti, Jean-Luc Dekeyser, Ph. Marquet, M. Abid, Master-Slave Control structure for massively parallel System on Chip, DSD SEAA - 16th Euromicro Conference on Digital System Design, Sep 2013, Santander, Spain, 2013
- [14] Scrucca L., On some extensions to GA package: Hybrid optimisation, parallelisation and islands evolution, The R Journal 9(1), pp.187-206, 2017
- [15] Jiaxing Qu, Guoyin Zhang, Zhou Fang, Jiahui Liu, A Parallel Algorithm of String Matching Based on Message Passing Interface for Multicore Processors, International Journal of Hybrid Information Technology, Vol.9, No.3, pp. 31-38, 2016
- [16] Jiahui Liu, Dahua Song, Yiqiu Xu, A Parallel Encryption Algorithm for Dual-core Processor Based on Chaotic Map, Proceedings of SPIE - The International Society for Optical Engineering SPIE Proceedings, 2012
- [17] Hoare C.A.R., Quicksort, The Computer Journal, vol. 5, pp 10-16, 1962
- [18] JaJa Joseph, An Introduction to Parallel Algorithms, Addison-Wesley publishing company, 1992

BIOGRAPHIES



ATANASKA D. BOSAKOVA-ARDENSKA was born in 1980. She received the M.Sc. degree of Computer Systems and Technologies at Technical University of Sofia, Plovdiv branch 2004. She receives Ph.D. in 2009 with thesis "Parallel information processing in image processing systems". From 2010 she is assistant in the department of Computer Systems and Technologies in University of Food Technologies. From 2014 she is associated professor by "Synthesis and Analysis of Algorithms" in Department of Computer Systems and Technologies in the University of Food Technologies in Plovdiv, Bulgaria. She is a member of USB (The Union of Scientist in Bulgaria) and head of Club of Young Scientists in Plovdiv (USB – Plovdiv in Bulgaria). Her research interests include: parallel algorithms, sorting algorithms, image processing, MPI (Message Passing Interface), C/C++ programming.

Rapid Diagnostic Lateral Flow Strip Test Reader

H. Ozkan

Abstract—Non-invasive rapid diagnostic tests (RDT) are commonly used to detect some kind of viruses or bacteria instead of invasive methods. *Helicobacter pylori* (*H. Pylori*) which causes gastric cancer, peptic ulcer, gastritis, mucosa-associated lymphoid tissue lymphoma diseases can be detected easily with lateral flow strip (LFS) that is one of the RDT types. The tests are evaluated whether there are control line and test line at the region of interest (ROI) by users or microbiology technicians manually. Once the test line is tentative, despite the test must be reported positive, it can be resulted as negative incorrectly. This incorrect diagnose causes incorrect treatment planning. In this work, to mitigate this problem which will be able to occur by human based, an automatic LFS-RDT reading system is developed. The computer laptop based system firstly takes image utilizing the holders that are designed with 3D printer. Whether the test have the control-test lines or not are carried out by image processing techniques straightforwardly. After feature extraction from line areas, k -NN classification method is used to evaluate the test results automatically. 100 LFS-RDTs are tested and observed that all results are correct. The system is found quite useful and approved as a second reader by medical technicians

Index Terms—Rapid diagnostic test reader, image processing, classification, k -NN.

I. INTRODUCTION

RDTs are easy to use and fast methods to detect HIV, *H. Pylori*, adeno virus, rota virus, malaria in a microbiology laboratories as non-invasive. Additionally, some physiological conditions such as pregnancy, blood glucose level, drugs of abuse, cholesterol, food poisoning are easily diagnosed by user themselves [1]. There are different types RDTs such as microfluidic Chip immunoassay [2], dipstick [3], pads [4], cassette test [5], and LFS [6-8]. Especially, RDTs are implemented in any developing countries even bad and inadequate conditions easily [9, 10]

To diagnose *H. Pylori*, LFS-RDT is used routinely. *H. Pylori* is a type of gram-negative bacteria and causes peptic ulcer, gastric cancer, gastritis, mucosa-associated lymphoid tissue lymphoma diseases [11-13]. Gaita, urea-breath or urine samples are used to detect *H. pylori* [14]. While urea-breath samples are being used at the test process with high sensitivity, urea-breath and gaita tests can be implemented together at the same time. However, gaita test is just the most economic methods among them. So it is preferred to use routinely [15].

H. OZKAN, Department of Biomedical Engineering, Faculty of Engineering, Fatih Sultan Mehmet Vakıf University, Istanbul, Turkey, (e-mail: hozkan@fsm.edu.tr; haydarozkan79@gmail.com). 

Manuscript received March 24, 2017; accepted June 07, 2017.
DOI: 10.17694/bajece.334337

Besides the improving of fast and practical medical test technologies, computer or smartphone based automatic diagnostic systems have been progressing expeditiously. These systems help physicians for evaluating the tests with accurate and certain results by saving time. This situation increases the quality of health systems positively. Routinely, RDTs are evaluated with visual inspections by medical technicians or users manually. Human based or illumination based incorrect evaluations can be encountered. To mitigate these problems, nowadays automatic reading systems have been developed by researchers. Generally, quantity tests are realized by checking whether there are control and test lines and reported the result with cell phone based RDT readers [1, 16, 17]. Also, the smart phone or Google Glass based RDTs, which can be done quantity tests, report the amount of the sample that is tested [18-20]. The mentioned cell phone based RDT readers have such electronic component for illumination. This condition is advantage for them but the components increase the cost and disinfection is not easy after the testing due to the external components. Also motion artefact on the captured images can arise because of shaking of hand. So we developed a laptop or tablet based RDT reader in our previous work [21]. There is no motion artefact since the system is stable on the table. Beside the designed RDT holder does not have any external component for illumination, disinfection is very easy. However, it is a disadvantage that there is no external illumination tools because the image quality can change with different illumination. So, in our previous work all images were captured with fixed indoor illumination

In this work, newly different system is developed to mitigate the illumination problem. New offered computer based system can work under different illumination conditions without external electronic illumination tools. First of all, using the RDT holders that are created from 3D printer, different images are captured under indoor illumination and sun light conditions. The images of each conditions different than each other in terms of background or brightness. After segmenting of ROI from taken image, each ROIs randomly are enhanced with the new preferred system. The control and test lines are segmented from the ROI. Then features are extracted from the line areas. Using k -NN classification method the tests are read as invalid, positive or negative. 100 LFS-RDT are tested to diagnose *H. pylori* and it is observed that all results under every condition are correct.

II. MATERIAL AND METHOD

In this study, dataset was taken from Medical school of Istanbul University, microbiology laboratory. In the laboratory, to detect *H. Pylori* LFS-RDTs are used. While the

test is preparing the gaita samples are used. Small samples from gaita are picked by touching a pin of extraction tube. The gaita samples are injected to the extraction tube and the tube is shaken to achieve homogeneity solution. The tube is waited during a few minutes vertically. So, solid particles fall down. A few drop of homogeneity solution is instilled to the LFS-RDT.

There are two lines area on the ROI of LFS-RDT: control and test lines. In case test line is appeared the result is positive otherwise the test is negative. Appearing the test line means that the sample has *H. pylori*. In the ROI, to signalize the test line, a monoclonal antibody is fixed to the membrane of ROI of LFS-RDT. If there is *H. pylori* antigen, a complex structure comprises by combining the antigen with the fixed antibody and a line appears. Otherwise, if there is no *H. pylori* the test line does not appear since the complex structure does not comprise. In the ROI, second antibody is used for control line. So, during the test, control line appears for any condition whether there is *H. pylori* or not. The control line has to appear for any condition, otherwise the test is invalid.

In this work 100 LFS-RDTs are used. 25 of them, which have tentative test line, are positive, 15 of them, that seem well test and control line, are positive, 53 are negative, and 7 are invalid. In Fig. 1., the tested LFS-RDTs are given. All of them are valid because they have control lines explicitly. Fig. 1.a. is reported as negative easily by medical technicians since there is no test line. Fig. 1.b is read as positive because there are both lines. But in Fig. 1.c., there is a tentative test line. The tentative test line sometimes is not noticed by technicians or users and they report the test as negative although it is positive. This incorrect diagnose follows incorrect treatment. In this work, to overcome the human based incorrect evaluation, a new automatic RDT reading system is preferred.

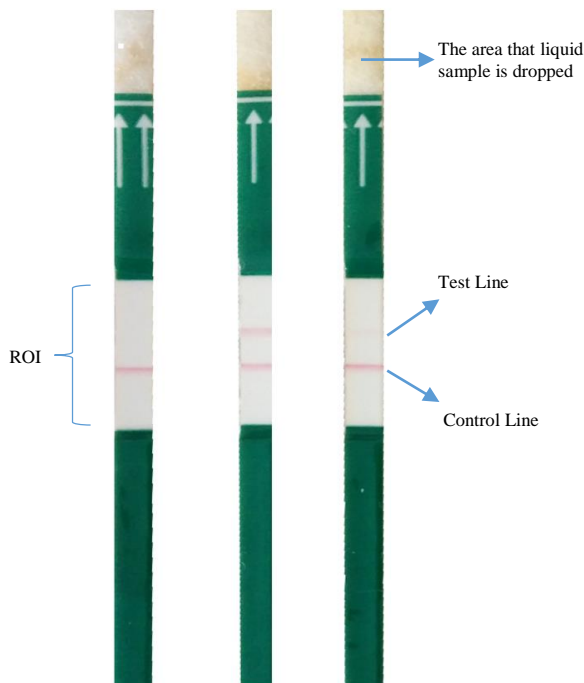


Fig. 1. LFS-RDTs that are used to diagnose *H. Pylori* a) The test which have negative result b-c) The tests which have positive results

This study is basically performed at three steps which are imaging, image processing, and classification. The detailed flow chart is shown in Fig. 2.

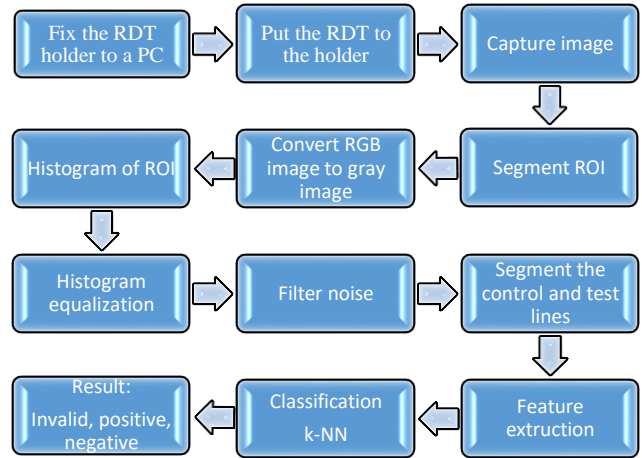


Fig. 2. The steps of proposed system

The designed RDT holders consist of two parts. First one is to hold LFS-RDT and looks like cassette RDT. Second one is to fix LFS-RDT in front of camera of PC (Fig. 3.) [21, 22].

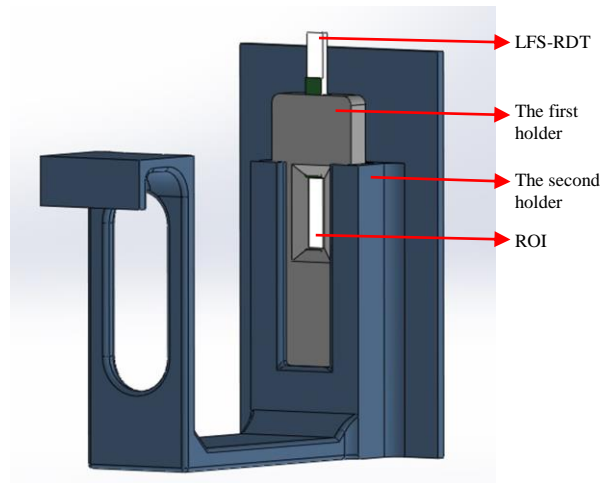


Fig. 3. LFS-RDT holders

After fixing the holders to the PC, The LFS-RDT is put to the holder as seen in Fig. 4. While the holders are designing, the ROI is arranged to be stable in front of the laptop camera



Fig 4. Fixing the LFS-RDT and holder to the PC laptop

After stabilizing the LFS-RDT and holders, image is captured. For every tests, all images have been taken both under daily light and indoor illumination. Then, image processing techniques using MATLAB are applied to the images to evaluate the tests with high accuracy.

First of all, ROI area are easily segmented since every LFS-RDT stand same position via fixed holders during the all test processes. In Fig. 5, different images of ROIs that have the results from negative to positive are given respectively. Each background of ROI is different than others as the images are captured under different illumination conditions. Some of them have white background, some of them have grey and the others have yellow.

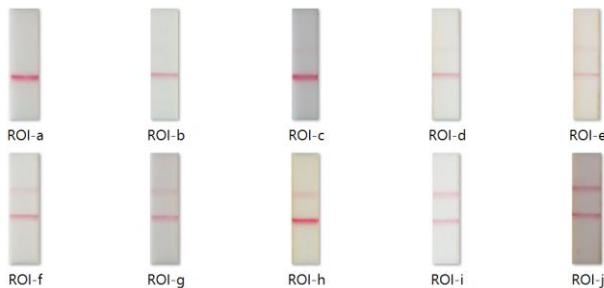


Fig. 5. ROI images that are taken in different illumination conditions a-b negative, c-d-e positive that have tentative test lines, f-g-h-i-j positive that have distinct test lines.

In Fig. 5.a.-b., ROIs have just control line, test lines does not appear. So, their test results are negative. Medical technicians or self-users can evaluate them as negative easily with visual inspections. However, in Fig. 5.c-d-e, despite control lines appear clearly, test lines are not seen obviously. Essentially, there are test lines on them but they are tentative. Users can report the test as negative incorrectly. They all are positive actually. In Fig. 5. f-g-h-i-j, the ROIs have both control and test lines that seem clearly. So their reporting process is quite easy. The problem is to report incorrectly the tests which have tentative test lines. By enhancing the tentative test lines to see clearly is quite important to have more accurate results.

RGB images are converted to gray scale images to use 8-bit image instead of 24-bit image. In Fig. 6, all gray level ROIs can be seen which are converted from Fig. 5. respectively.



Fig. 6. The ROIs images that are converted gray images from RGB images of Fig. 5

To enhance the images, the histograms of ROIs are carried out. A histogram shows frequencies of intensity values in an image. In Fig. 7, the histogram of Fig. 6.d. is shown. Horizontal axis gives intensity values; vertical axis shows frequencies of any intensity values. As it can be seen clearly the image is low contrast image since intensity values are just sorted between 180 to 225. So, the test line looks like grey and nearly white colour but actually it should be seen nearly black.

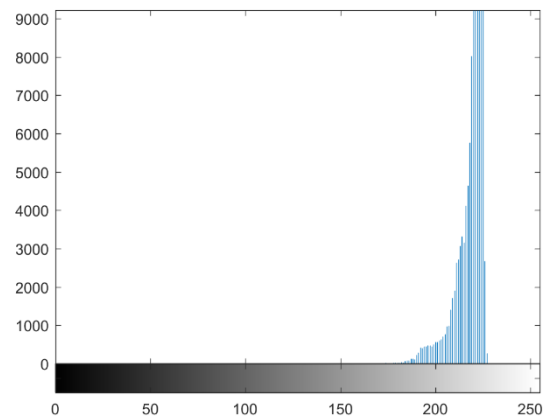


Fig. 7. The histogram of Fig. 6.d. image

To increase the contrast, histogram equalization technique is implemented. It is proposed that the intensity levels scatter between 0 to 255. To equalize the histogram firstly probability of any intensity level has to be calculated with Equation 1.

$$p_r(r_k) = \frac{n_k}{MN}, \quad k = 0,1,2, \dots L - 1 \tag{1}$$

Where r_k is intensity value, p_r probability, n_k the number of pixel that has r_k intensity value, L maximum intensity level, MN total number of pixel. Then Equation 2. or 3. are used for intensity transformation

$$s_k = T(r_k) = (L - 1) \sum_{j=0}^k p_r(r_j) \tag{2}$$

$$s_k = \frac{(L-1)}{MN} \sum_{j=0}^k n_j \tag{3}$$

All probabilities are gathered cumulatively and they are multiplied with one mines maximum intensity level. After transformation, decimally numbers are achieved and they are rounded. The obtained s_k that are integer numbers, are assigned to a new intensity values and the histogram distributes equally between 0 to 255. The new histogram of Fig. 6.d. after histogram equalization can be seen in Fig. 8.

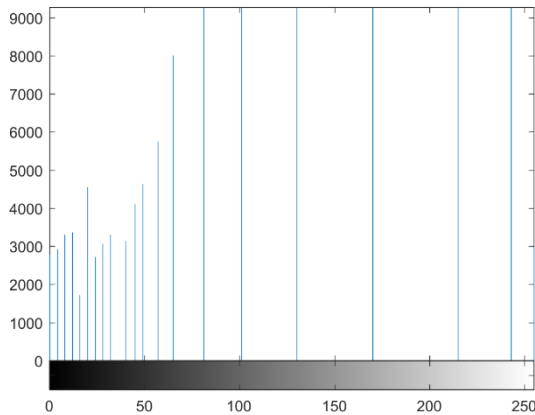


Fig. 8 The high contrast histogram of Fig. 6.d. that is carried out after histogram equalization technique

When Fig. 7 and Fig. 8. are compared, it is obviously seen that the low contrast histogram turns the high contrast histogram. In Fig. 9, the histogram equalized ROIs of Fig. 6 are given from a. to j. respectively.

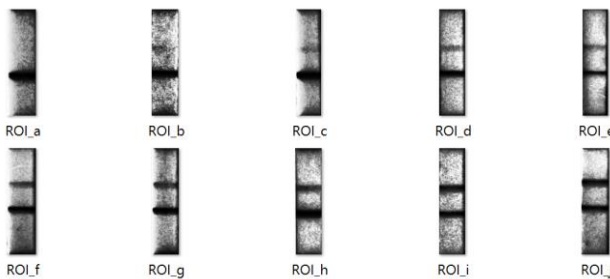


Fig. 9. The ROIs that are acquired after histogram equalization process from ROIs of Fig. 6

In Fig 5. a. and 6. a., the given RGB and gray level images are evaluated as negative since the test line does not appear. After histogram equalization, the result is verified (Fig. 9.a). Although The ROIs in Fig. 5.b. and 6.b does not have test line, In Fig. 9.b, there is small quantities in the test line area but it is not found enough to decide as positive by medical technicians. Especially, in Fig. 5. c-d-e. and 6. c-d-e. the nonvisible test lines, after histogram equalization, appear as visible as it can be seen in Fig. 9. c-d-e. So, they are easily resulted as positive. The ROIs in Fig 9. from f. to j. can be evaluated positive since all the test lines appear clearly. In Fig. 10. The zoomed ROIs are shown. In Fig. 10.a. has zoomed ROIs of Fig. 5.a, 6.a. and 9.a. In Fig. 10.b. shows zoomed ROIs of Fig. 5.d, 6.d. and 9.d. In Fig. 10.c. indicates zoomed ROIs of Fig 5.i, 6.i. and 9.i. It can be seen that tentative test line can be clearly read with the

improved reading system. Besides, it is observed that the system can work with different illumination conditions.

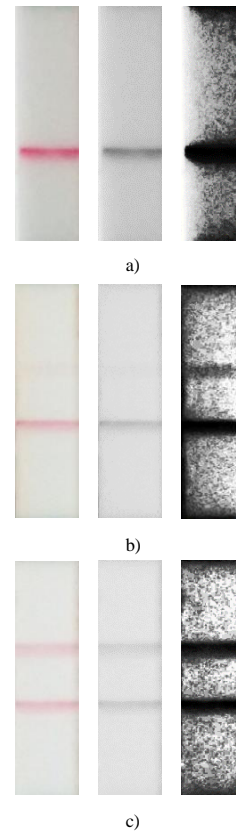


Fig. 10. a) Zoomed ROIs of Fig. 5.a, 6.a. and 9.a. b) zoomed ROIs of Fig. 5.d, 6.d. and 9.d. c) zoomed ROIs of Fig 5.i, 6.i. and 9.i

Before feature extraction, median filter is implemented the histogram equalized ROIs to remove noise. The coordinates of control and test lines are stable during the test, they are segmented from ROIs. Six different features are extracted from both test and control lines in Table 1.

TABLE I.
THE EXTRACTED FEATURES

Features
Average intensity value
Maximum intensity value
Minimum intensity value
Difference between minimum and maximum intensity value
Standard deviation
Entropy

Using the k -NN classification method with two steps, firstly control line is classified to report the test valid or not and then the test line is classified to report the test positive or negative. If the first classification result is valid, then the second step starts. Otherwise, the system reports the test result as invalid. 5 neighbours are used for k -NN classification. It is observed that all classification results are correct with the highest accuracy as 100%.

III. CONCLUSION AND DISCUSSION

In this study, an automatic LFS-RDT reading system is developed. The images are captured from RDTs and image processing techniques are implemented to the ROIs for enhancing the image, features are extracted from control and test lines and the tests are classified with k -NN method firstly the test is evaluated in terms of valid or invalid, and if the system valid secondly the test is resulted as positive or negative. If the test is invalid, the result is reported and second step does not continue.

To verify the accuracy of the result, first of all, the test results have been read by medical technicians' with visual inspection and they have been compared with the results that have been taken from the designed LFS-RDT reader platform. It has been observed that the system is run efficiently having all correct results as 100% accuracy. The designed LFS-RDT reader platform has been evaluated and validated by testing the total of 100 *H. pylori* RDT tests. 25 of 100 are tentative positive, 15 of 100 are positive, 53 of 100 are negative and the rest (7) are invalid.

In the literature, some cell phone based RDT reader platforms [1, 16, 17, 18, 19] and a Google Glass based RDT reader platform [20] are designed by researchers. Carrio et al. have classified their tests with multilayer perceptron artificial neural network technique and declared 96% accuracy [1]. Mudanyali et al. have used colour intensity level of test and control line to analyse the RDT automatically and reported 100% accuracy [16]. Dell et. al. reported approximately 97% accuracy by using threshold based decision system in their RDT reader platform [17]. You et al. have measured intensity level of test end control line and classify their reading system having 97% accuracy [18]. Mudanyali et al. Carrio et al., and You et al. designed an external illumination platform on their cell phones including some LEDs, batteries to decrease environmental light effect [1, 16, 18]. The illumination platform provides good benefit to increase the image quality but it also increases the cost of reader system. Our RDT reader platform does not have an external illumination source this situation was disadvantage for our earlier study. However, in this work, this mentioned disadvantage is extinguished with improving new image processing technique. In our earlier study, Gaussian filter was used to smooth the image and then sigmoid function is used to release the lines for taken image under just indoor illumination [21]. However, in this work, low contrast images are converted to high contrast images with histogram equalization technique and noises are removed with median filter for images that are captured with different illumination conditions such as sun light or indoor illumination. This result provides us to have low cost RDT reader platform since having holder without external illumination source. Shen et al. have quantified the colours by using colorimetric diagnostic assays. They have not declared specific number of their system accuracy but they reported that they have high accuracy [19]. Feng et al. have had 100% accuracy using their Google Glass based platform. They have designed QR code to crop ROI and used SVM for classifying the RDT. Their RDT platform need to have internet connection since their reader platform sends the captured image to a server and gets the result back to the Google Glass from the server [20]. Our platform runs real time on the computer without

internet connection as an advantage of the designed RDT reader platform. Another advantage of our RDT reader platform is not to have motion artefacts on the capturing image since computer laptop is stand as fixedly. On the other hand, cell phone and Google Glass based RDT reader platforms can have motion artefacts since they are held by user hand or head that can be shaken. Besides, the cell phone or Google Glass based RDT reader platforms can be used point of care tools but cannot be adapted to a hospital computer network system. However, the designed RDT reader platform in this work both can be easily used as a point of care diagnostic tool or connected to an existing hospital computer network systems and used routinely in the hospital. When all these advantages are considered, the medical technicians declared that the designed new automatic LFS-RDT reader platform can be used as a second reader.

ACKNOWLEDGEMENT

The author would like to thank Professor Dr. Betigul Ongen who is Chief of the Microbiology Laboratory of Istanbul University Hospital, in Istanbul, Turkey

REFERENCES

- [1] Carrio, A. Sampedro, C. Sanchez-Lopez, J. L. Pimienta M. and Campoy, P. Automated low-cost smartphone-based lateral flow saliva test reader for drugs-of-abuse detection, *Sensors*, 15, 29569-29593, 2015.
- [2] Li, J. J., Ouellette, A. L., Giovannardi, L., Cooper, D. E., Ricco, A. J., and Kovacs, G. T. A., "Optical scanner for immunoassays with up-converting phosphorescent labels," *IEEE Transactions on Biomedical Engineering*, vol. 55, no. 5, pp. 1560-1571, 2008.
- [3] Nuriman, B. K., Huskens, J. and Verboom, W. "Optical sensing systems for microfluidic devices: a review," *Analytica Chimica Acta*, vol. 601, no. 2, pp. 141-155, 2007.
- [4] Lee, D.-S. Jeon, B. G. Ihm, C. Park, J.-K. and Jung, M. Y. "A simple and smart telemedicine device for developing regions: a pocket-sized colorimetric reader," *Lab on a Chip—Miniaturisation for Chemistry and Biology*, vol. 11, no. 1, pp. 120-126, 2011.
- [5] Zhu, H. Isikman, S. O. Mudanyali, O. Greenbaum, A. and Ozcan, A. "Optical imaging techniques for point-of-care diagnostics," *Lab on a Chip*, vol. 13, no. 1, pp. 51-67, 2013.
- [6] Zhang, X. Li, D. Wang C. et al., "A CCD-based reader combined quantumdots-labeled lateral flow strips for ultrasensitive quantitative detection of anti-HBs antibody," *Journal of Biomedical Nanotechnology*, vol. 8, no. 3, pp. 372-379, 2012.
- [7] Li, Z. Wang, Y. Wang, J. Tang, Z. Pounds, J. G. and Lin, Y. "Rapid and sensitive detection of protein biomarker using a portable fluorescence biosensor based on quantumdots and a lateral flow test strip," *Analytical Chemistry*, vol. 82, no. 16, pp. 7008-7014, 2010.
- [8] Hou, Y., Wang, K., Xiao, K., Qin, W., Lu, W., Tao, W., & Cui, D., Smartphone-Based Dual-Modality Imaging System for Quantitative Detection of Color or Fluorescent Lateral Flow Immunochromatographic Strips. *Nanoscale Research Letters*, 12, 291. 2017, <http://doi.org/10.1186/s11671-017-207>
- [9] Sista, R.; Hua, Z.; Thwar, P.; Sudarsan, A.; Srinivasan, V.; Eckhardt, A.; Pollack, M.; and Pamula, V. "Development of a digital microfluidic platform for point of care testing", *Lab Chip*, 8, pp.2091-2104, 2008.
- [10] Lee, W. G.; Kim, Y.G.; Chung, B.G.; Demirci, U.; and Khademhosseini, A. "Nano/Microfluidics for diagnosis of infectious diseases in developing countries", *Adv. Drug Delivery Rev.*, 62, pp. 449-457, 2010.
- [11] Saez, J., Belda, S., Santibáñez, M., Rodríguez, J. C., Sola-Vera, J., Galiana, A., Royo, G., "Real-Time PCR for Diagnosing Helicobacter pylori Infection in Patients with Upper Gastrointestinal Bleeding: Comparison with Other Classical Diagnostic Methods." *Journal of Clinical Microbiology*, vol. 50, no. 10, pp. 3233-3237, 2012, <http://doi.org/10.1128/JCM.01205-12>.
- [12] Ribeiro, M. L., Ecclissato, C. C., Mattos, R. G., Mendonca, S., and Pedrazzoli Jr., J., "Quantitative real-time PCR for the clinical detection of Helicobacter pylori." *Genetics and Molecular Biology*, vol. 30, no. 2, pp. 431-434, 2007, <https://dx.doi.org/10.1590/S1415-47522007000300022>.

- [13] Schabereiter-Gurtner, C., Hirschl, A. M., Dragosics, B., Hufnagl, P., Puz, S., Kováč, Z., Rotter, M., and Makristathis, A., "Novel Real-Time PCR Assay for Detection of *Helicobacter pylori* Infection and Simultaneous Clarithromycin Susceptibility Testing of Stool and Biopsy Specimens." *Journal of Clinical Microbiology*, vol.42, no.10, pp. 4512–4518, 2004, <http://doi.org/10.1128/JCM.42.10.4512-4518.2004>
- [14] Burucoa, C., Delchier, J.-C., Courillon-Mallet A., et al., "Comparative evaluation of 29 commercial *Helicobacter pylori* serological kits," *Helicobacter*, vol. 18, no. 3, pp. 169–179, 2013.
- [15] Muhammad M. and Yoshio Y., "Diagnostic Methods of *Helicobacter pylori* Infection for Epidemiological Studies: Critical Importance of Indirect Test Validation," *BioMed Research International*, Article ID 4819423, vol. 2016, pp. 1-15, 2016. doi:10.1155/2016/4819423
- [16] Mudanyali, O. Dimitrov, S. Sikora, U. Padmanabhan, S. Navruz, I. and Ozcan, A. "Integrated rapid-diagnostic-test reader platform on a cellphone," *Lab on a Chip*, vol. 12, no. 15, pp. 2678–2686, 2012.
- [17] Dell N. and Borriello, G. "Mobile tools for point-of-care diagnostics in the developing world," in *Proceedings of the 3rd ACM Symposium on Computing for Development (ACM DEV '13)*, Bangalore, India, January 2013.
- [18] You, D. J. Park, T. S. and Yoon, J.-Y. "Cell-phone-based measurement of TSH using Mie scatter optimized lateral flow assays," *Biosensors and Bioelectronics*, vol. 40, no. 1, pp. 180–185, 2013.
- [19] Shen, L. Hagen, J. A. and Papautsky, I. "Point-of-care colorimetric detection with a smartphone," *Lab on a Chip*, vol. 12, no. 21, pp. 4240–4243, 2012.
- [20] Feng, S. Caire, R. Cortazar, B. Turan, M. Wong A., and Ozcan, A. "Immunochromatographic diagnostic test analysis using Google glass," *ACS Nano*, vol. 8, no. 3, pp. 3069–3079, 2014.
- [21] Ozkan, H. and Kayhan, O. S. "A Novel Automatic Rapid Diagnostic Test Reader Platform," *Computational and Mathematical Methods in Medicine*, vol. 2016, Article ID 7498217, 10 pages, 2016. doi:10.1155/2016/7498217.
- [22] Kayhan, O. S. "Automatic reading of rapid diagnostic tests and informing the clinicians with e-report", M.Sc. Thesis, Istanbul Technical University, Biomedical Engineering Department, 2016.

BIOGRAPHY



Haydar OZKAN was born in Mucur-Kırşehir, Turkey in 1979. He received the B.Sc. degree from Frat University Electric Department, in 2000. He completed his M.Sc. in 2004 at Marmara University Electric Department and Ph.D. in 2011 at Sakarya University, Electronic and Computer Department. He participated in Bio and Nano photonics laboratory in University of California, Los Angeles, Electrical Department USA between 2014-2015 as a Postdoctoral researcher. He is currently Assist. Prof. Dr. at Fatih Sultan Mehmet Vakıf University, Biomedical Engineering Department. His research areas are telemedicine, image processing, signal processing and machine learning.

Simulation and Power Flow Control Using Switching's Method of Isolated Wind-Solar Hybrid Power Generation System with Battery Storage


E. Oguz, Y. Oğuz and H.Çimen


Abstract—In this paper, a battery-supported hybrid wind-solar energy generation system with switching power flow control is presented to supply stable electrical power to two laboratories at the Electric & Electronic Engineering Department. For this purpose, 600W 3-phase permanent magnet synchronous generator (PMSG) based on the wind power generation system (WPGS) and the solar power generation system (SPGS) consisting of 190W 3 pieces mono crystal solar panel were combined to build a 1170W hybrid wind-solar power generation system (HWSPGS). The solar and wind power generation systems were used as the main energy sources while 100 Ah 12V 6 pieces gel jeep cycle accumulator groups were used as the energy storage device to ensure continuity of energy. Also dynamic modeling and switching power flow control of the battery supported the HWSPGS were performed using Matlab/Simulink in this study. Determining the switching positions of the charge control unit according to loading and battery charge situations of the HWSPGS, power flow control between the generation unit and consumer was made in planned manner. When the curves of electrical magnitudes obtained from simulation results were examined, it was determined that no big difference existed in electrical and mechanical magnitudes in parallel to dynamic behavior of the installed hybrid power generation system.


Index Terms—Wind power generation, solar power generation, hybrid power generation, battery storage, switching power flow control.

I. INTRODUCTION

NOWADAYS, electrical energy from day to day is known more as needed. Additionally, the amount of energy needed for generation and consumption and whether it is economic, productive and environmental friendly are the elements that increase the countries level development [1].

E. OGUZ, Çanakkale Onsekiz Mart University, Biga Vocational School, Department of Electrical and Energy, Çanakkale, Turkey. (e-mail: emrahoguz@comu.edu.tr) 

Y. OĞUZ, Afyon Kocatepe University, Technology Faculty, Department of Electrical & Electronic Engineering, Afyonkarahisar, Turkey. (e-mail: yukseloguz@aku.edu.tr) 

H. ÇİMEN, Afyon Kocatepe University, Technology Faculty, Department of Electrical & Electronic Engineering, Afyonkarahisar, Turkey. (e-mail: hcimen@aku.edu.tr) 

The energy need of the world has been met mostly by fossil base fuels. For this reason, countries increasingly depend on such fuels. However, as the negative effects of fossil base fuels on environment have reached the peak levels, reserves are almost consumed, and foreign-source dependency of countries increases, researches on new energy sources have been inevitable. In this process, the most important researches have been on renewable energy sources that do not have negative effects on environment and renew themselves permanently [2].

In general, the renewable energy sources comprise mainly wind and solar energies, and also the non-fossil base energy sources such as hydroelectric, geothermal, biomass (wood, solid wastes, ethanol, etc).

The biggest share in renewable energy sources and electric energy generation of Turkey belongs to hydroelectric and wind energy. Though the share of wind and solar energies in electric generation is very small when compared to other world countries, it is expected that these shares will increase in the future. However, other countries have made contribution to electric energy generation using the wind turbine and solar cell together or separately since 1970s. In general, hybrid power generation systems installed using the renewable energy sources are used to meet the electric energy demand of residential areas in far distance from electric distribution network. There are some hindrances for electric energy generation existing separately from wind turbine or solar cell. The most important hindrances are that the generated electric energy is interrupted, and the first installation costs are high and the sufficient technological knowledge lacks [3-6].

While the electric energy can only be generated from the sun in daytime, the load remains without energy in the rest of the day. The wind energy does not have definite limits like solar energy, while the electric energy can be generated in some hours of day. The load may remain without energy in the rest of the day. As for the power cut during the day, the consumption surplus of energy generated in time zones when the energy generation can be made is stored in the battery and in time zones when the generation is insufficient; the load is fed from the battery to meet the energy need.

Electric energy that will be obtainable from the wind and solar energy differs depending on seasons. In winter months, electric energy generation from the sun may not be possible for

day’s time. Similarly, electric energy generation from wind in spring and summer months remains very low [4-8].

Solving the seasonal electric energy generation interruption problem by increasing battery capacity will increase the cost but may not be possible in many areas. Such interruptions may be removed to a great extent with the installation of hybrid power generation system by using the wind turbine and solar panel together depending on characteristics of the region [5].

The hybrid power generation systems are installed through parallel connection of two or more conventional and renewable energy generation systems to each other. The hybrid power generation systems are one of the best solution methods to meet the electric energy need of mini or micro networks far distance from energy generation and distribution centers and of small settlement units. Most commonly, the wind-solar hybrid power generation system is used [9-12].

For electric generation systems in various structures, recently, hybrid energy generation systems are realized by combining mainly the wind and the solar energy and fuel cells and soon. However, as more staff will be used for hybrid energy generation systems installed with more than one renewable energy source, the cost and installation area need will increase and structure and inspection of the system will become complicated [13].

In this paper, teaching the topic will start with the description of a battery-supported hybrid wind-solar energy generation system with some general background about how the system works with solar energy, wind energy, load and energy storage. This portion is theoretical and can be explained by the instructor in the class. After that, three steps of planning and building the hybrid system involving renewable energy and load forecasting, renewable energy farm scale optimization, power flow control will be studied by using SimPowerSystems toolboxes in MATLAB. This portion would need the use of a computer lab or it can be in the form of assignments to students depending on their knowledge about power systems.

By considering the stated reasons above, a battery supported with 1170W wind-solar hybrid power generation system was installed to meet the electric energy required for small power receivers in two electric laboratories in the department of Electrical-Electronics Engineering at Afyon Kocatepe University. A hybrid power generation system related to dynamic behaviors of system components was modelled and simulated thanks to SimPowerSystems in the Matlab/Simulink program. The data obtained from the simulation block diagram of the system almost expressed the real-time electric and mechanical output magnitudes of the installed hybrid power generation system. By comparing the data from the real system to data obtained from the simulation study, the accuracy analysis and power flow control of the simulation study related to hybrid power generation system was realized in the planned manner.

II. BATTERY-SUPPORTED WIND-SOLAR HYBRID POWER GENERATION SYSTEM AND MODELING

General view of the installed battery supported wind-solar hybrid power generation system is given in Fig. 1. The installed hybrid power generation system consists of a 600W wind turbine, 190W 3 pieces’ solar panels, battery group, and 1200W hybrid charge control unit that enables the operation of these units in harmony and 3kW full sinus wave inverter for consumers fed with alternative current.

Furthermore, the data related to the energy generated by the hybrid power generation system can be followed via the charge control unit in 10 second intervals and by means of the *winpowernet* interface program; it can be followed via computer and be recorded in a Microsoft Excel file

The dynamic modeling of each unit of the installed hybrid system in conformity to its real-time behaviors was realized using the SimPowerSystems in the Matlab/Simulink program. Then, each modeled unit was combined in the DC bus bar, and simulation model of the hybrid power generation system shown in Fig. 2 was established.

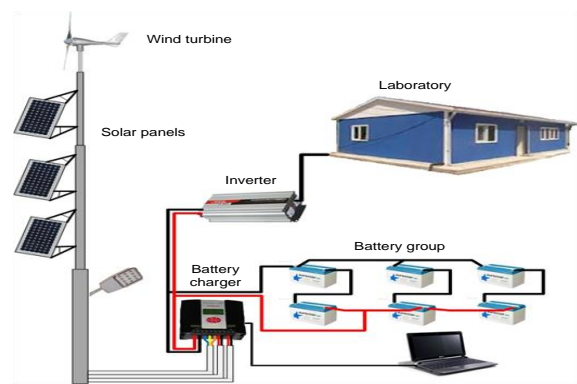


Fig. 1 General view of the installed battery powered wind-solar hybrid power generation system

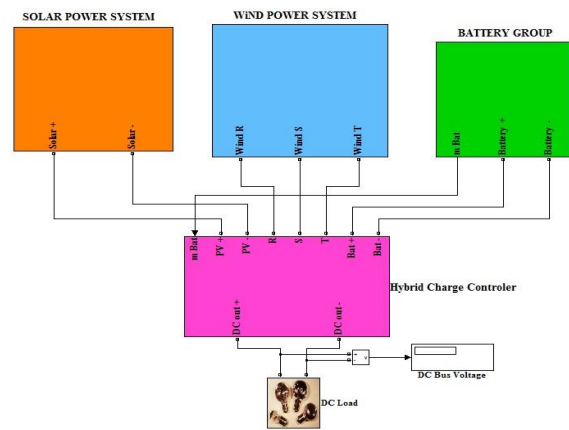


Fig. 2 Block diagram of the battery powered wind-solar power generation system

Our first generation unit is the PMSG wind generation system. Some factors are important to determine the installation place of a wind turbine. Some of them are continuous and high wind speed and absence of elevations around the turbine that may obstruct the air flow. The simple operation of a wind turbine is as follows; when air flow hits to turbine wings, it causes the turbine wings to turn and as a result of this, the shaft where the turbine wings are connected turns. In small power wind turbines, this shaft is generally connected to generator directly but in huge power wind turbines, it is generally connected to generator by means of a gear box [11-15].

Generators convert mechanic energy to electric energy. While permanent magnet generators are used mostly in lower power wind turbines, in high power turbines, synchronous and asynchronous generators are used [16-18].

The wind turbine in the installed system has three wings and a two meter wing diameter. The turbine was directly coupled to the permanent magnet synchronous generator without using of gear box. The permanent magnet synchronous generator has 3-phase 36V output voltage and 600W power. The wind power generation system starts to make a generation in speed of 2.5 m/s and its maximum power generation value is 12 m/s. At 60m/s speeds, rotor is stopped mechanically.

Additionally, it may be stopped magnetically by making manual control on the charge control unit. According to the specifications given above, a wind power generation system model was established using the SimPowerSystems in the Matlab/Simulink program.

The simulation block diagram of the wind power generation system with constant speed PM synchronous generator established is shown in Fig. 3. The parameters and values that belong to the wind turbine and PMSG are given in Table 1.

TABLE.1 WIND TURBINE AND PMSG PARAMETERS

Performance parameters	
Measured power (W)	12 V 400W – 24V 600W 3 phase AC
Wind speed measured	12
Start-up wind speed	2.5
Maximum wind speed	Max.25
Wind speed to Disarm	60
Motion parameters	
Gear box	Unavailable
Generator	Direct permanent magnet
Rotor blades	3 – carbon fiber reinforced plastic
Diameter of the rotor blade (m)	2
Rotor speed control	mechanical method
Speed	750
PMSG Electrical parameters	
Stator phase resistance R_s (Ω)	0.12
Inductances [L_d (H) L_q (H)]	8.5e-3
Flux linkage established by magnets (V.s)	0.055133
Voltage constant (Vpeak L-L/krpm)	36
Torque constant (N.m/A-peak)	0.3308
Inertia, friction factor, pole pairs [J(kg.m ²) F(N.m.s) p()]	[0.002, 0.02, 4]
Initial conditions [ω_m (rad/s) θ_{em} (deg) $i_{a,ib}$ (A)]	[60 ,0 ,0 ,0]

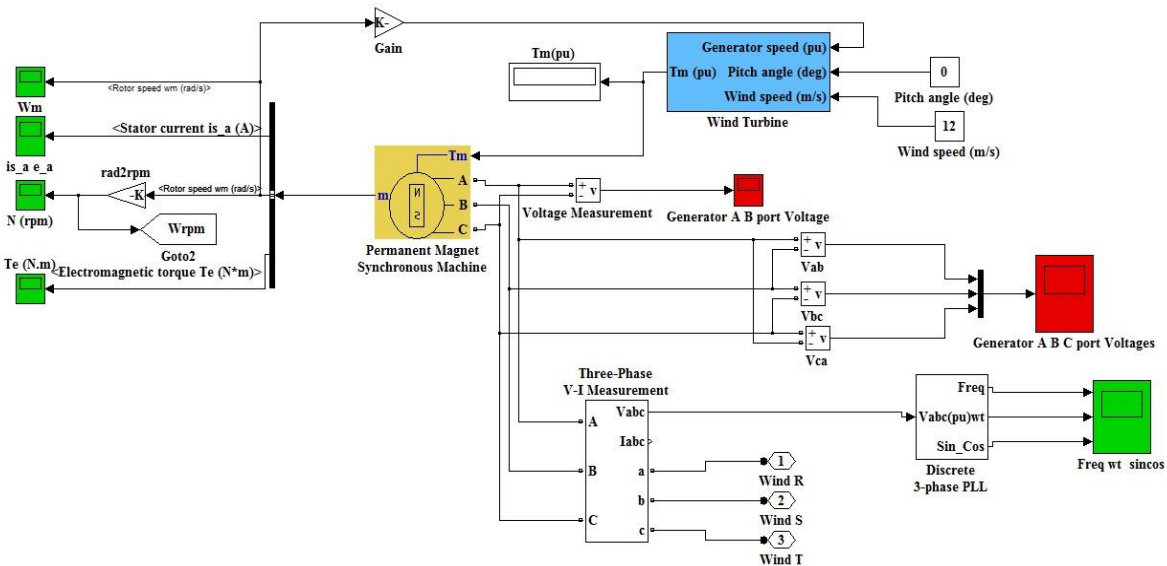


Fig. 3 Simulation Block Diagram of constant speed PMSG wind power generation system

Our second generation unit is the solar power generation system established with parallel connection of solar panels. Solar panels convert the sun light to direct current electric energy. Sufficient light level is quite important in electric generation. Operational expenses of these generation systems are very low and its reliability is very high. In today's technology, solar panels in various sizes from a few watts to 300W are manufactured. The biggest disadvantage of solar cells is their high cost. Usage period of solar panels varies between 10-25 years depending on their manufacturing technologies [19-22].

The solar power generation system in the installed hybrid system is in power of 570W and established with parallel connection of 3 pieces of mono crystal solar panels in power of 190W. The photovoltaic panels used have the same features and consist of 72 cells, and their efficiency is 18%. The electrical equivalent circuit of the photovoltaic cell is given in Fig. 4. This equivalent circuit is expressed with a mathematical formula in equation (1). The simulation block diagram of the solar panel was established in accordance with this formula. Then, a simulation block diagram of the solar power generation system was established with the parallel connection of 3 panels as shown in Fig. 5.

$$I_{pil} = I_{FV} - I_0 \left[\exp \left(\frac{e}{kT_{pil}} (V_{pil} + R_s I_{pil}) \right) - 1 \right] - \frac{V_{pil} + R_s I_{pil}}{R_{SH}} \quad (1)$$

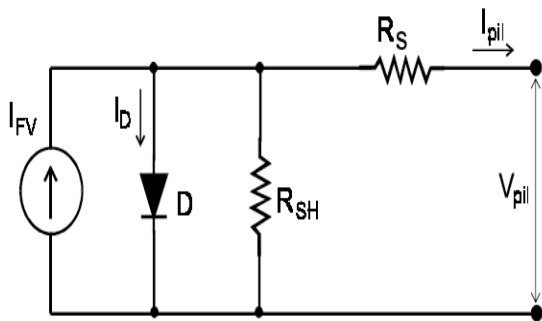


Fig. 4 Electrical equivalent circuit of a photovoltaic cell [8]

The electrical parameters and values of the solar panels used in this study are given in Table 2.

TABLE II. PARAMETERS OF PHOTOVOLTAIC PARAMETERS

Parameters	Variables	Value
Nominal Power (W)	P_{max}	190 W
Maximum Power Voltage (V)	V_{max}	37.08V
Maximum Power Current(A)	I_{max}	5.12 A
Open-Circuit Voltage (V)	V_{oc}	44.48 V
Short-Circuit Current(A)	I_{sc}	5.54 A

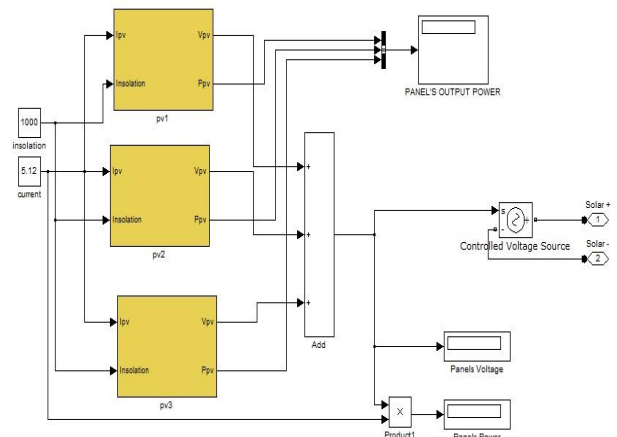


Fig. 5 Simulation Block Diagram of the Solar Power Generation System

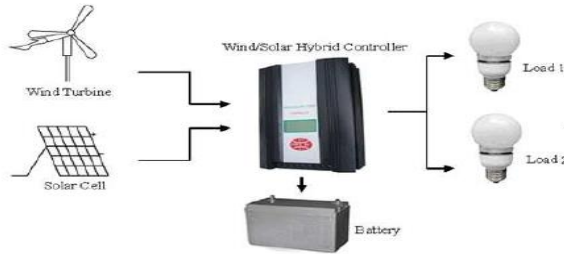
The third unit is the battery group consisting of 6 pieces of 100Ah-12V gel deep cycle accumulators that are used to store the consumer's surplus electric energy or to ensure continuousness of energy through renewable energy system in times when no generation is made. Batteries are electrochemical elements that store electric energy in chemical form. The battery types used together with renewable energy sources are lead- acid, nickel-cadmium, nickel-iron, iron-air batteries, and soon. Life of batteries varies between 1-10 years depending on operating conditions. Though the first investment costs of such batteries are low, their maintenance and renewal costs are very high. Today, gel accumulators are used in higher rates. Though their first investment costs are high, they do not have any maintenance costs. The battery capacities are expressed in kWh that is the multiple of Ah and nominal voltages [23-25].

Six pieces of 100Ah-12V gel accumulators in the installed hybrid power generation system were connected in series in two groups and so three groups in 24 V 100 Ah were established. Then, these groups by being connected as parallel among them power capacities in value of 24 V 300 Ah were obtained.

Our last unit is the charge unit, the brain of the hybrid power generation system that is used to connect the power generation units to each other as parallel on a bus bar, charge the accumulator group, and feed the receiver in a controlled manner. Electric energy coming from the PMGS wind power generation system and solar panels to the control unit may come from both when the weather is windy and sunny or only from one of them when the wind or sun is effective.

It is completely depending on whether the weather is sunny and windy at the moment of operation. Additionally, in PM generator of the wind turbine, a 3-phase alternative voltage is generated and in the solar panel, a direct voltage is generated. For parallel connection of these two systems, their energy forms and magnitudes must be the same. This is provided by the hybrid charge control unit as shown in Fig. 6. The charge controller converts 3-phase AC voltage coming from the PM generator to the desired DC form and magnitude with AC/DC converter, and the DC voltage coming from solar panels to the desired magnitude with DC/DC converter; and, it transfers them

to outside as battery charge voltage by combining the converter outputs.



Picture 1, wind&solar hybrid system wiring diagram

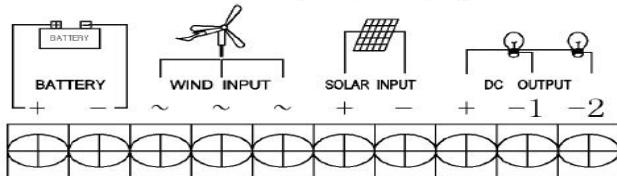


Fig. 6 The connection schema of the installed hybrid power generation system's charge control unit

The battery group is charged with the energy sent from the hybrid charge control unit. For this reason, voltage of the battery group varies depending on the energy amount coming from the system. LCD on the hybrid charge controller indicates current, voltage and power information of the electric energy generated from the wind and solar energy, accumulator and DC outputs. The data can be monitored from the computer display with the Winpowernet interface program via RS-232 and be saved as a Microsoft Excel file whenever it is desired.

Moreover, the operational security of the system is ensured through this controller with the new magnetic brake assembly designed in conformity to the characteristic of the generator.

A simulation block diagram that reflects the explanation of working features, functions and characteristics of the hybrid charge control unit above in the real time was also established. Additionally, a controller was developed to make the energy flow control and coupled inside of the charge control unit. In this way, the hybrid charge controller with a switching method was obtained which is shown in Fig. 7.

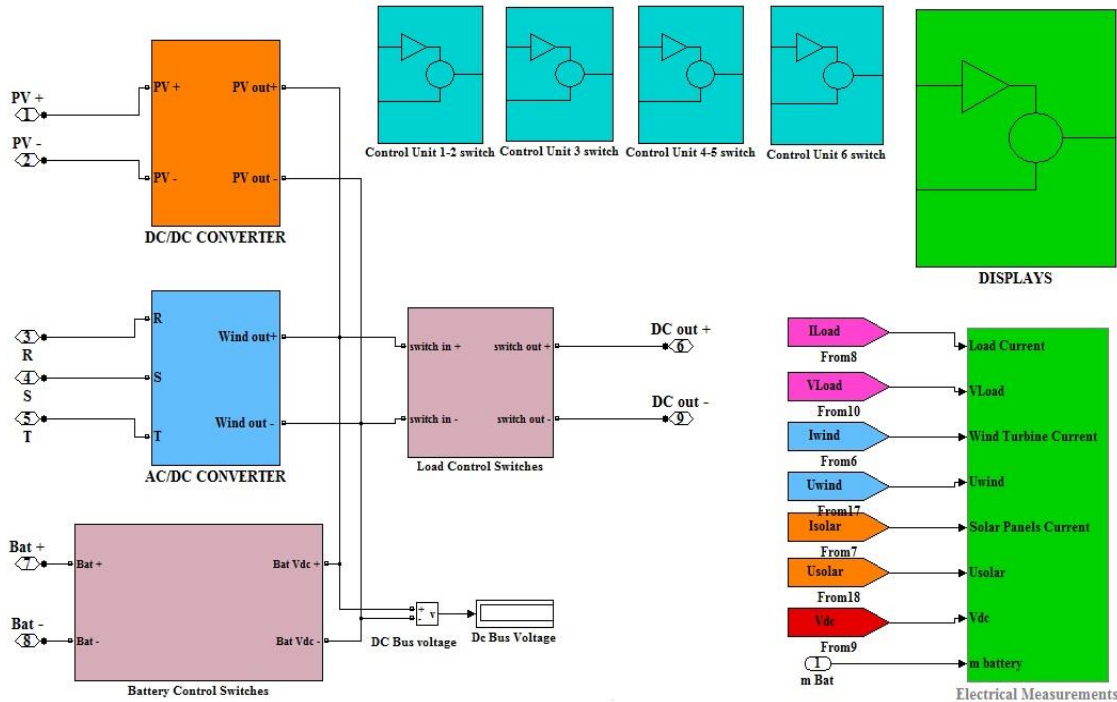


Fig. 7. Simulation block diagram of the hybrid charge controller

III. CONTROL STRATEGY FOR ENERGY MANAGEMENT AND POWER FLOW IN HYBRID POWER GENERATION SYSTEM

At this part, the negative conditions in real-time energy flow of the installed and simulated hybrid energy generation system were observed. Upon this, a switched power flow controller was designed to ensure effective use of power from the hybrid power generation system, increase its efficiency, and conserve the system more effectively; and energy flow control of the system was realized.

The working strategy of the switched controller is within the framework of 6 rules as it can be understood from the flow diagram in Fig. 8, and it shows the energy management strategy of the charge control unit in detail depending on the system loading, generation and battery charge conditions.

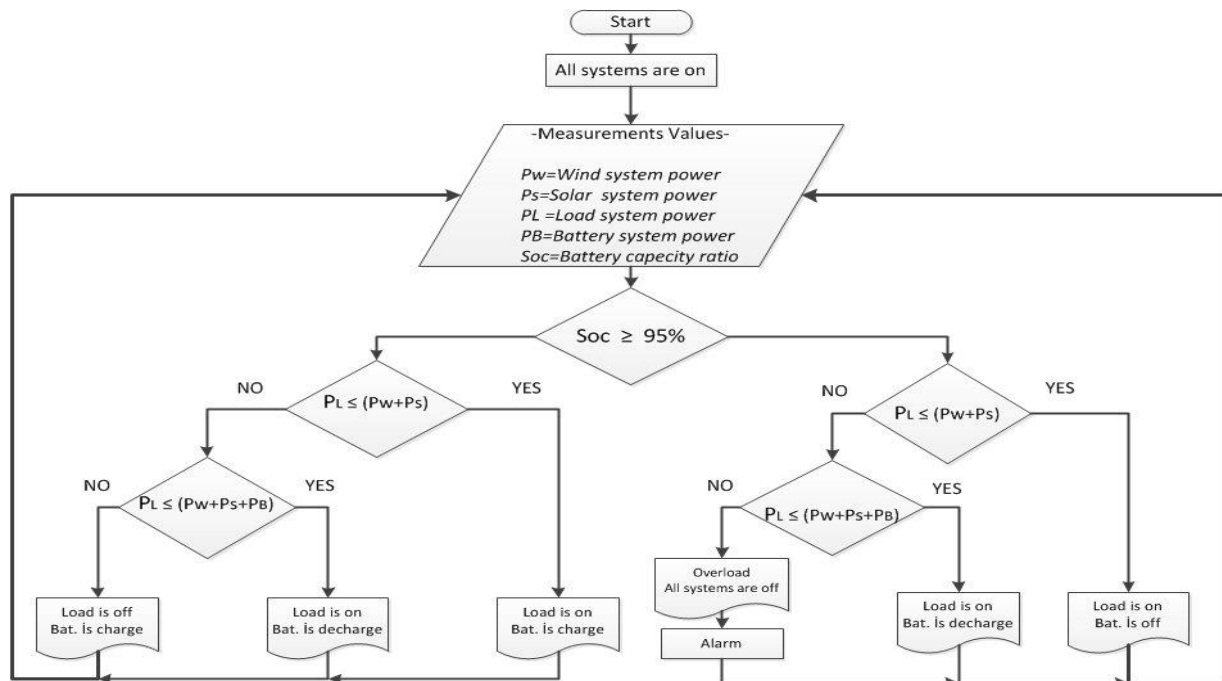


Fig. 8 Flow diagram of energy management strategy

The six rules determined for efficient and effective use of energy are given below in detail.

- a) If the battery charge rate is more than 95% and consumed power is smaller than the total generated power, receiver is powered directly through the wind-solar hybrid power generation system after the battery is deactivated.
- b) If the battery charge rate is more than 95%, and the consumed power is higher than the total generated power but smaller than the total power generated with battery, receiver is powered with battery power after all the system is activated.
- c) If the battery charge rate is more than 95%, and consumed power is higher than the total generated power and power stored in the battery, this means that excessive load is connected. All the systems must be deactivated.
- d) If the battery charge rate is less than 95%, and consumed power is smaller than the total generated power, the receiver is powered by being activated and surplus power is stored in the battery.
- e) If the battery charge rate is less than 95%, and consumed power is higher than the total generated power but smaller than the total power generated with battery power, the battery must be passed to discharge position by activating the receiver.
- f) If the battery charge rate is less than 95%, and consumed power is higher than the total generated power and the total power stored in the battery, this means that excessive load is connected. The load must be deactivated, and it must be charged by activating the battery as it is not full charged.

The main reasons why such a control strategy for the hybrid power generation system has been developed are to increase the efficiency of system by making energy flow control, prevent shortening of battery life and protect the system and receiver against the excessive loading conditions. As a matter of fact, the power generally generated in small power hybrid power generation systems is directly sent to the battery group, and receivers are powered on battery group. However, this condition increases the risk for the battery to be excessively charged or discharged, and it also decreases its lifetime. Unfortunately, energy generated in the installed real-time system is directly sent to the storing units and receivers are powered on them. The cost of batteries constitutes an important part of the system cost. Additionally, when an excessive load is connected to the system, the system elements may be damaged because of the excessive discharge and excessive current drawn from the battery group. In an ideal system, the power needed by the receiver must be directly sent to the receiver to power it up, and if there is surplus generated power, it must be stored in the battery depending on its charge condition.

A switched power flow controller design was made in a manner eliminating the negative conditions expressed above. A simulation study was realized by applying the switched power flow controller to the battery powered hybrid power generation system.

IV. THE SIMULATION RESULTS AND DISCUSSION

Energy production does not prove that the system is efficient because the transferring of energy generated in installed systems to the receiver in a controlled manner, the storing of energy in absence of a receiver, and the most importantly, making of power flow controls are also very important for efficiency and productivity of the system. For this reason, recently, a quite many studies have been made for the energy control and these works have still been going on. In general, sending of generated energy directly to the storing units and powering up receivers from there has been emphasized. However, that the storing units are continuously in active position results in decreasing in their lifetime. It should not be forgotten that costs of storing units are very important for the system. In other words, the uncontrolled use of energy decreases the lifetime of system elements and increases the risk for receivers to remain without energy.

In this paper, the simulation results of generation, and consumption powers of the installed and simulated 1170W hybrid power generation system were given separately depending on their various loading conditions, and their analyses were made.

TABLE III. SYSTEM LOADING PARAMETERS

System Loading	Wind Power System		Solar Power system		Battery Group	Load
	Wind Speed (m/s)	Pitch Angel (deg)	Current (A)	Insolation	SOC (%)	Power (W)
1.Loading situation	12	0	5.12	1000	95	480
2.Loading situation	12	0	5.12	1000	95	950
3.Loading situation	12	0	5.12	1000	95	1550
4.Loading situation	9	0	5.12	950	95	1550

The dynamic behavior of electrical magnitudes (current, voltage and power) was observed by connecting the receivers in different powers to the system. As it can be understood from Table 3, in the first three loading conditions, maximum input values were applied to the wind-solar hybrid power generation system by assuming that the battery group was full charged during full power generation (1170W). In the fourth loading condition, wind input values of the wind power generation system and radiation input values of the solar power generation system were reduced and connected to the receiver power system in the third loading condition. Generation reaction of the hybrid power generation system and reaction of the system against the receiver were observed.

As it can be understood from the simulation curves given below;

In the first loading condition, a 480W receiver is connected to the system. In that loading condition, as the consumed power is smaller than the total generated power and the battery group is in full charged condition, the hybrid charge controller deactivates the battery group. Because the hybrid power generation system can feed the consumer without battery support. The power required by the consumer can be met with a generation system that has lower power. The simulation results are shown in Fig. 9.

In the second loading condition, a receiver in power of 950W is connected to the system. In this loading condition, as the consumed power is smaller than the total generated power, and the battery group is in full charged condition, the hybrid charge controller deactivates the battery group. However, the power consumed in that loading condition is bigger than the individual generation power capacities of the generation units (wind-solar). For this reason, the power requirement of the consumer must be met through operation of the wind-solar power generation unit together. The simulation results are given in Fig. 10. Principally, 570W of the power consumed by the consumer is provided from the solar power generation system and 380W from the wind power generation system.

In the third loading condition, the hybrid power generation system is loaded by increasing the consumer power, 1550W. As the consumed power is higher than the total generated power in that loading condition, generation power of the hybrid power generation system will be insufficient. In that situation, the needed power requirement must be supported by battery group. According to the simulation results in Fig. 11, the battery group is activated by the hybrid charge controller. In this manner, the consumer is fed from the hybrid power generation with battery support. 600W of the power consumed by the consumer is met from the wind power generation system and 570W from the solar power generation system; 1170W is provided from the hybrid power generation system and 380W from the battery group.

In the fourth loading condition, the wind speed of the system is decreased to 9m/s, and solar radiation level is decreased to 950. Then reaction of the system is observed. Power generation of the hybrid system decreases due to diminishing wind speed and solar radiation. In that case, the total generated power will decrease below 1170W. To meet the power needed by the consumer, the battery group must give more power than the third loading condition. As it can be seen from the simulation results given in Fig. 12, the power consumed by the consumer is provided by 414 W wind power generation system, 495 W the solar power generation system and 640 W the battery group.

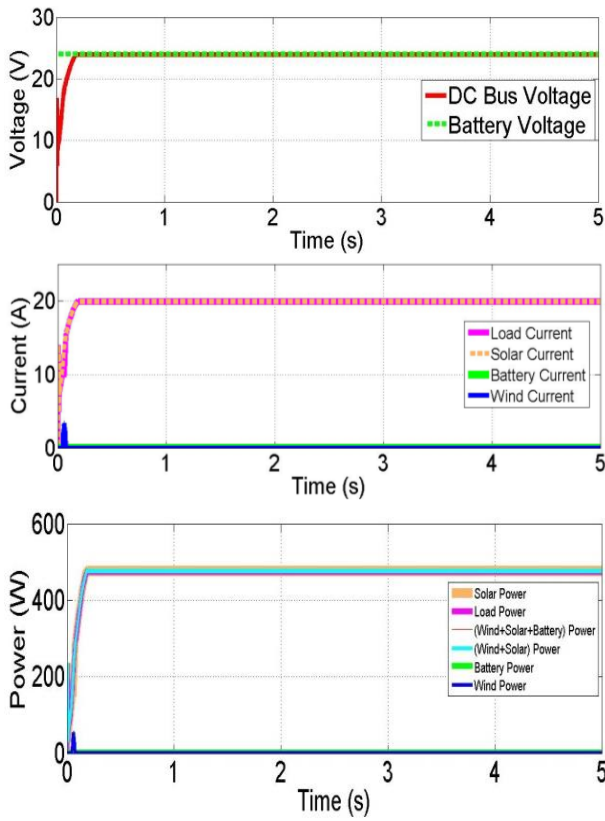


Fig. 9 First loading situation

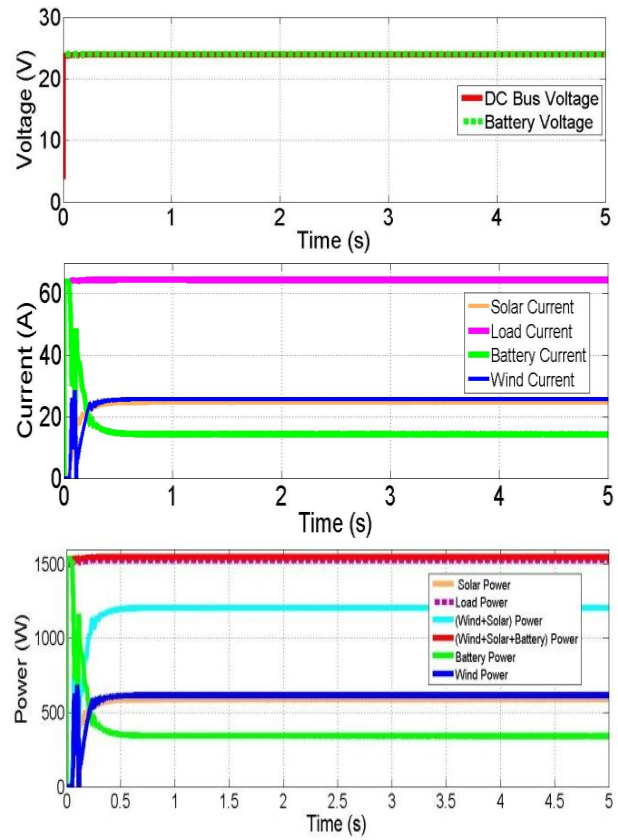


Fig. 11 Third loading situation

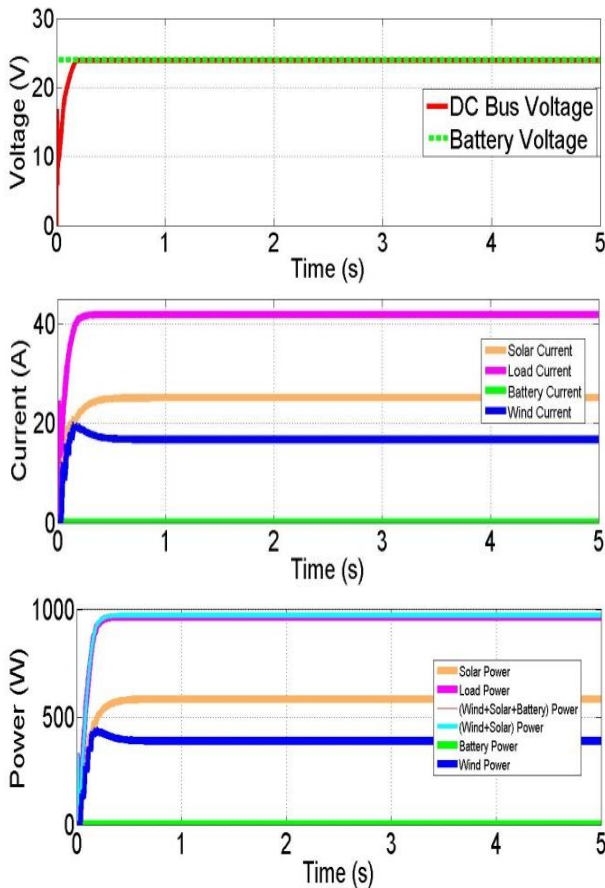


Fig. 10 Second loading situation

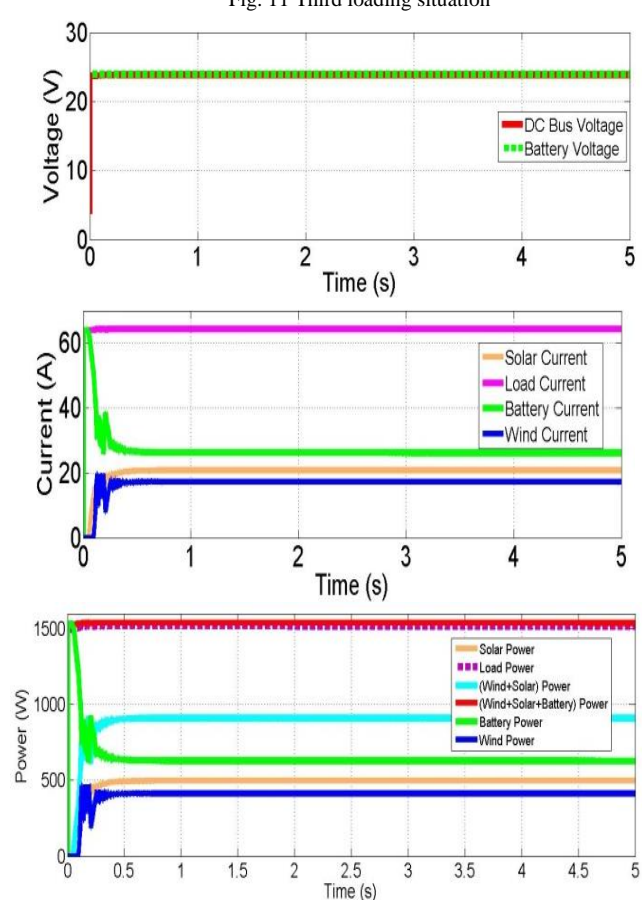


Fig. 12 Fourth loading situation

V. CONCLUSIONS

The application of studies made for energy control directly on real systems may cause occurrence of various unfavorable conditions. Mainly, conditions that give damage to the system elements and the most importantly to the human life have occurred. For this reason, making of exact simulation model of the system to be controlled and then applying control on the simulation primarily will conserve the system elements and human life first and foremost.

In this study, by considering such negative conditions, a real-time modeling of the installed wind-solar hybrid power generation system and energy flow controller to eliminate the troubles in systems were designed. When dealt with the curves obtained from the simulation results, it is seen that there are not big differences in the electrical and mechanical magnitudes in parallel to dynamic behavior of the installed hybrid power generation system. Besides, by exactly comparing the data obtained from the real system with the data obtained from the simulation study, it has been reached the conclusion that accuracy rating of the simulation study realized related to the hybrid power generation system is correct. As a matter of fact, it is seen from the simulation results that the controller designed for energy flow control operates with a very good performance. According to the simulation results, troubles that might occur in energy flow have been eliminated with the switched controller developed. The battery group is activated and deactivated according to behaviors of the system in loading condition. In this manner, decrease in lifetime of the battery is prevented. This decreases the maintenance cost of the system. Moreover, the system is protected against the excessive loading conditions.

On the other hand, students learn to understand how a hybrid power generation system works, the characters of renewable energy sources such as wind energy and solar energy, and how to utilize renewable energy sources efficiently in this study. Moreover, the simulation and experimental environments used to develop and verify the developed hybrid system can be a very effective tool to increase students' knowledge and interests about those subjects.

In the future, thanks to the installed hybrid power generation system, students at electric department will be able to carry out studies on the simulation model instead of studying on the real-time system by taking risk on subjects such as electric generation with renewable energy systems, system control and efficiency of generated energy and soon. In this way, they will develop the new energy control methods and test the controllers they develop on the simulation without any risk so that, will be able to make their applications safely on a real system.

ACKNOWLEDGMENT

The research for this article has been supported by grant number 10-TEF-05 from Afyon Kocatepe University Scientific Research Projects Coordination Unit.

REFERENCES

- [1] Chedid, R. & Rahman, S. (1997). Unit sizing and control of hybrid wind-solar power systems, *IEEE Transactions on Energy Conversion*, 12(1), pp. 79-85.
- [2] Bonanno, F., Consoli, A., Raciti, A., Morgana, B. & Nocera, U. (1999). Transient analysis of integrated diesel/wind/photovoltaic generation systems, *IEEE Transactions on Energy Conversion*, 14(2), pp. 232-238.
- [3] Habib, M. A., Said, S. A. M., El Hadidy, M. A. & Al-Zaharna, I. (1999). Optimization procedure of a hybrid photovoltaic wind energy system, *Energy*, 24(11), pp. 919-929.
- [4] Bayer, H. G. & Christian, L. (1996). A method for the identification of configurations of PV / wind hybrid systems for the reliable supply of small loads, *Solar Energy*, 57(5), pp. 381-391.
- [5] Morgan, T. R., Marshall, R. H. & Brinkworth, B. J. (1997). A refined Simulation program for the sizing and optimization of autonomous hybrid energy systems, *Solar Energy*, 59, pp. 205-215.
- [6] Rajendra, P. A. & Natarajan, E. (2006). Optimization of integrated photovoltaic-wind power generation systems with battery storage, *Energy*, 31(12), pp. 1943-1954.
- [7] Altaş, İ. H. (1993). Control strategies for maximum power tracking and energy utilization of a stand-alone photovoltaic energy system, PhD diss., The University of New Brunswick, Faculty of Engineering, Department of Electrical Engineering, Fredericton, Canada.
- [8] Diaf, S., Diaf, D., Belhamel, M., Haddadi, M. & Louche, A. (2007). A methodology for optimal sizing of autonomous hybrid PV/wind system, *International Journal of Energy Policy*, 35(11), pp. 5708-5718.
- [9] Mittal, R., Sandu, K. S. & Jain, D. K. (2010). Battery energy storage system for variable speed driven pmsg for wind energy conversion system, *Power Electronics, Drives and Energy Systems*, 1, pp. 300-304.
- [10] El Ali, A., Moubayed, N. & Outbib, R. (2007). Comparison between solar and wind energy in Lebanon, *9th International Conference on Electrical Power Quality and utilization*, pp. 1-5.
- [11] Gagliano, S., Neri, D., Pitrone, N., Savalli, N. & Tina, G. (2009). Low-cost solar radiation sensing transducer for photovoltaic systems, *WSEAS Transactions on Environment and Development*, 5(2), pp. 119-125.
- [12] Barsali, S. & Ceraolo, M. (2002). Dynamical Models of Lead-Acid Batteries: Implementation Issues, *IEEE Transactions on Energy Conversion*, 17(1), pp. 16-23.
- [13] Moubayed, N., Kouta, J., El-Ali, A., Dernayka, H. & Outbib, R. (2008). Parameter identification of the lead-acid battery model, *33rd IEEE Photovoltaic Specialists Conference*, pp. 1-6.
- [14] Onar, O. C., Uzunoglu, M. & Alam, M. S. (2006). Dynamic modeling, design and simulation of a wind/fuel cell/ultra-capacitor-based hybrid power generation system, *Journal of Power Sources*, 161(1), pp. 707-722.
- [15] Thiringer, T. & Linders, J. (1993). Control by variable rotor speed of a fixed-pitch wind turbine operating in a wide speed range, *IEEE Transactions on Energy Conversion*, 8(3), pp. 520-526.
- [16] Molina, M. G. & Juanicó, L. E. (2010). Dynamic modelling and control design of advanced photovoltaic solar system for distributed generation applications, *Journal of Electrical Engineering: Theory and Application*, 1(3), pp. 141-150.
- [17] Valenciaga, F., Puleston, P. F. & Battaiotto, P. E. (2003). Power control of a solar/wind generation system without wind measurement: a passivity/sliding mode approach, *IEEE Transactions on Energy Conversion*, 18(4), pp. 501-507.
- [18] Borowy, B. S. & Salameh, Z. M. (1994). Optimum photovoltaic array size for a hybrid wind/PV system, *IEEE Transactions on Energy Conversion*, 9(3), pp. 482-488.
- [19] Bogdan, S. B. & Salameh, Z. M. (1996). Methodology for optimally sizing the combination of a battery bank and PV array in a wind/PV hybrid system, *IEEE Transactions on Energy Conversion*, 11(2), pp. 367-375.
- [20] Elhadidy, M. A. & Shaahid, S. M. (2005). Decentralized /standalone hybrid Wind-Diesel power systems to meet residential loads of hot coastal regions, *Energy Conversion and Management*, 46(15-16), pp. 2501-2513.
- [21] Hajizadeh, A., Tesfahunegn, S. G. & Undeland, T. M. (2011). Intelligent control of hybrid photovoltaic/fuel cell/energy storage power generation system, *Journal of Renewable and Sustainable Energy*, 3(4), 043112.

- [22] Garrison, J. B. & Webber, M. E. (2011). An integrated energy storage scheme for a dispatchable solar and wind powered energy system, *Journal of Renewable and Sustainable Energy*, 043101.
- [23] Bakić, V., Pezo, M., Stevanović, Ž., Živković, M. & Grubor, B. (2012). Dynamical simulation of PV/wind hybrid energy conversion system, *The 24th International Conference on Efficiency, Cost, Optimization, Simulation and Environmental Impact of Energy*, 45(1), pp. 324–328.
- [24] Belfkira, R., Zhang, L. & Barakat, G. (2011). Optimal sizing study of hybrid wind/PV/diesel power generation unit, *Solar Energy*, 85(1), pp. 100-110.
- [25] González, I., Ramiro, A., Calderón, M., Calderón, A. J. & González, J. F. (2012). Estimation of the state-of-charge of gel lead-acid batteries and application to the control of a stand-alone wind-solar test-bed with hydrogen support”, *International Journal of Hydrogen Energy*, 37 (15), pp. 11090-11103.

BIOGRAPHIES



Emrah OGUZ was born in Çanakkale, Turkey, in 1986. He received BSc degree from the Afyon Kocatepe University Technical Education Faculty, Department of Electrical Education, Afyonkarahisar and the MSc degree in Electrical Education from the Afyon Kocatepe University, Institute of Science. He has been studying for PhD degree in Electric and Electronic Engineering Department at Pamukkale University. He has been a lecturer Electric & Energy Department at Çanakkale Onsekiz Mart University.

He has worked mainly in renewable energy, automatic control applications, power generation systems and control.



Yüksel OĞUZ was born in Afyon, Turkey, in 1971. He received BSc degrees from the Marmara University Technical Education Faculty, Department of Electrical Education, Istanbul, and the MSc and the PhD degrees in Electrical Education from the Marmara University, Institute for Graduate Studies in Pure and Applied Sciences, in 2000 and 2007, respectively. He has been an assistant professor in the Electronic and Electronic Engineering Department at Afyon Kocatepe University. He has worked mainly

in control education, automatic control applications, electrical machines, power generation systems and control, renewable energy, and intelligent control.



Hasan ÇİMEN received Bachelor and Master Degree in Electrical Education at the Marmara University, Istanbul in 1985 and 1988, respectively. In 1998, he received PhD degree in Power System Control from Sussex University, Brighton, UK. He is currently a Professor and Chairman of Electrical-Electronics Engineering at the University of Afyon Kocatepe in Turkey. His research and educational interests are power system control, intelligent electronic circuits, vocational and technical education, dispersive power generation systems that

employ solar arrays, fuel cells, etc.

Design and Optimization of a High Power Density and Efficiency Boost PFC


B. Fincan, M. Yilmaz, A. Goynusen, and K. Erenay


Abstract—Nowadays electrical appliances have been becoming more and more popular every day in our life, and the systems that have more power density and that use energy efficiently and that improve the quality of the energy are required more. Especially with the decisions and regulation changes of the United States and the European Union in recent years, it has become compulsory to replace low efficiency electric motor drive systems with high efficiency permanent magnet electric motors and drivers, and as a result permanent magnet motors that have high efficient field orientation control algorithms technologies have begun to be chosen. Low cost uncontrolled rectifiers that have high power factor have become a necessity with the need for DC bus. In such systems with inherently nonlinear characteristics, the need for Power Factor Correction (PFC) circuit has been increasing, and Boost PFC (BPFC) which increase the input voltage are widely preferred for low/medium power applications. Therefore, distortion harmonics and high frequency noises are reduced according to standards such as CS RIP Class B – TS EN 61000-3-2 and also output voltage remains constant, becoming more than peak amount of the input grid voltage. In that study, it is designed that BPFC that has 1,150W output power level by increasing system's power density and efficiency. The system cost is reduced by decreasing the requirement of EMI filters and heatsink size, since using SiC (Silicon Carbide) diode and optimizing the system contribute increasing efficiency and power density. The most efficient Boost PFC design is realized at the lowest cost by performing detailed design, loss and cost analysis for each component used. The Boost PFC with full system efficiency of 95.5% at full load is obtained by model validation done by comparing the simulation results with the experimental results obtained by hardware implementation.

Index Terms—Active filter, harmonic, efficiency, power density, power factor correction, SiC diode.

I. INTRODUCTION

ENVIRONMENTAL problems are emerging day by day with increasing energy demand and therefore the importance of more efficient use of energy is increasing. Without considering the effects on the economy and the

B. FINCAN, is with Department of Electrical Engineering, Istanbul Technical University, Istanbul, Turkey, (e-mail: fincan@itu.edu.tr). 

✉ **M. YILMAZ**, is with Department of Electrical Engineering, Istanbul Technical University, Istanbul, Turkey, (e-mail: myilmaz@itu.edu.tr). 

A. GOYNUSEN, is a senior engineer at Pavotek R&D, Istanbul, Turkey, (e-mail: alper.goynusen@pavotek.com.tr). 

K. ERENAY, is a manager at Pavotek R&D, Istanbul, Turkey, (e-mail: kerem.erenay@pavotek.com.tr). 

Manuscript received April 4, 2017; accepted July 6, 2017.
DOI: [10.17694/bajece.334355](https://doi.org/10.17694/bajece.334355)

environment, the use of all kinds of energy and systems distorts the ecological balance and causes global warming. In this context, energy resources in the country's economy should be evaluated with sustainable development approach, and efficient production and saving of energy should be taken into consideration. For this reason, it has come to the agenda to replace the inefficient drive systems with more efficient systems with the regulations and restrictions introduced.

Permanent magnet synchronous motors are the most efficient motors and have high power densities, which require voltage-fed driver. This type of conventional voltage-fed drive systems, which have disadvantages such as high cost, a large number of semiconductor switch elements, and complex control algorithms, require DC bus voltage, except for the matrix converters and they also produce harmonics and noise.

Electrical systems that transmit high frequency components (harmonics and noises) to the grid can cause electronic devices that do not have enough immunity to electromagnetic interference (EMI) to be adversely affected or distorted. For this reason, the expected noise level from a device conforming to electromagnetic compatibility (EMC) standards is that does not transmit noise to the grid, and that it is resistant to external noise, and that the elements inside the device do not interfere or distort each other. For these reasons, energy quality and efficiency are very critical in electric energy systems and precautions must be taken [1].

Passive filters consisting of elements such as inductance, capacity and resistance can be used to suppress reactive components at higher frequency values. The reactive power suppressing capacitive compensation systems in the fundamental frequency components are the most commonly used passive filter systems. These filters are not able to act on reactive components outside of the previously targeted frequencies and carry the risk of resonance with the capacitive or inductive components in the grid and the capacitive or inductive load that the system feeds. In this case, the overcurrent generated at the resonance frequency can damage the system [2]. With the BPFC used as an active filter, the phase difference between the current that grid feeds and the grid voltage, the reactive power and grid harmonics are reduced to zero and the power factor converges to one. In power electronic circuits, the power factor (PF) cannot be measured only by the phase difference between current and voltage ($\cos\phi$). Because the expression of $\cos\phi$ is only a measure of the fundamental frequency components. In fact, as can be seen in Equation (1), the power factor is the ratio between average value of the product of the input current and input voltage and the effective

value of the product of the input current and input voltage. In other words, the PF calculation is calculated by concept of Total Harmonic Distortion (THD), which is seen in Equation (2), where high frequency currents are also considered.

$$PF = \frac{\frac{1}{T_s} \int_0^{T_s} v_{in}(t) \cdot i_{in}(t) dt}{\sqrt{\frac{1}{T_s} \int_0^{T_s} (v_{in}(t) \cdot i_{in}(t))^2 dt}} = \cos \varphi \cdot \frac{1}{\sqrt{1+THD^2}} \quad (1)$$

$$THD = \frac{\sum_{n=2}^{n=\infty} I_n^2}{I_1} \quad (2)$$

BPFC can keep the output voltage constant even when the input voltage increases or decreases. In this way, even if the voltage drops, the motor input voltage does not change and the motor operation is not affected. Since the output voltage is higher than the peak value of the input voltage, there is also a minimum value for the output voltage. For a single-phase system in Turkey, this value cannot be less than 381 V because the effective value of the mains voltage in Turkey can rise to 265V. The average value of the output voltage can be selected as at least 385V since it is necessary to work somewhat away from the limit value. The BPFC elements have a maximum voltage level due to their internal resistance. If the output voltage is close the input voltage in the BPFC, the converter can work more efficiently [3]. The input current of the medium power motors (1 - 3 kW) operating with 400V input voltage is low, so copper losses are reduced and these motors can operate at wider speed and torque range depending on the input voltage. Therefore, the fact that the BPFC with 400V output voltage is

able to run with very high efficiency, which provides a great advantage in electric motor applications. For higher power systems, bridgeless PFC or interleaved PFC circuits should be used [4].

For the design of a high-efficient and power-intensive BPFC, detailed loss analysis must be performed by selecting the appropriate elements [5]. Each element is sized according to current and voltages and the selection of elements has been made with detailed designs in which losses and cost are taken into consideration. While SiC diode and system optimization result in increase in total efficiency and power density, and EMI filter and heatsink requirement are reduced and total system cost is reduced. The simulation results are compared with the hardware implementation results, and a BPFC with 1,150W output power is realized by increasing the power density and efficiency at low cost.

II. BPFC

There are three modes in the BPFC depending on the inductance current continuity: 1. Continuous conduction mode (CCM), 2. Discontinuous conduction mode, 3. Critical conduction mode. In the context of this work, CCM with less switching losses has inductance current which closer to the sinusoidal than other modes, and therefore has smaller EMI filters [6]. Figure 1 shows the BPFC and the control block diagram for this circuit. From the point of view of cost and loss analysis, it can be said that five main system components should be concentrated. These are uncontrolled bridge rectifier, inductance, output capacitor, MOSFET and diode. In the scope of the study, electronic card design and hardware system have been implemented by analyzing every system element, designing and making the necessary calculations accordingly.

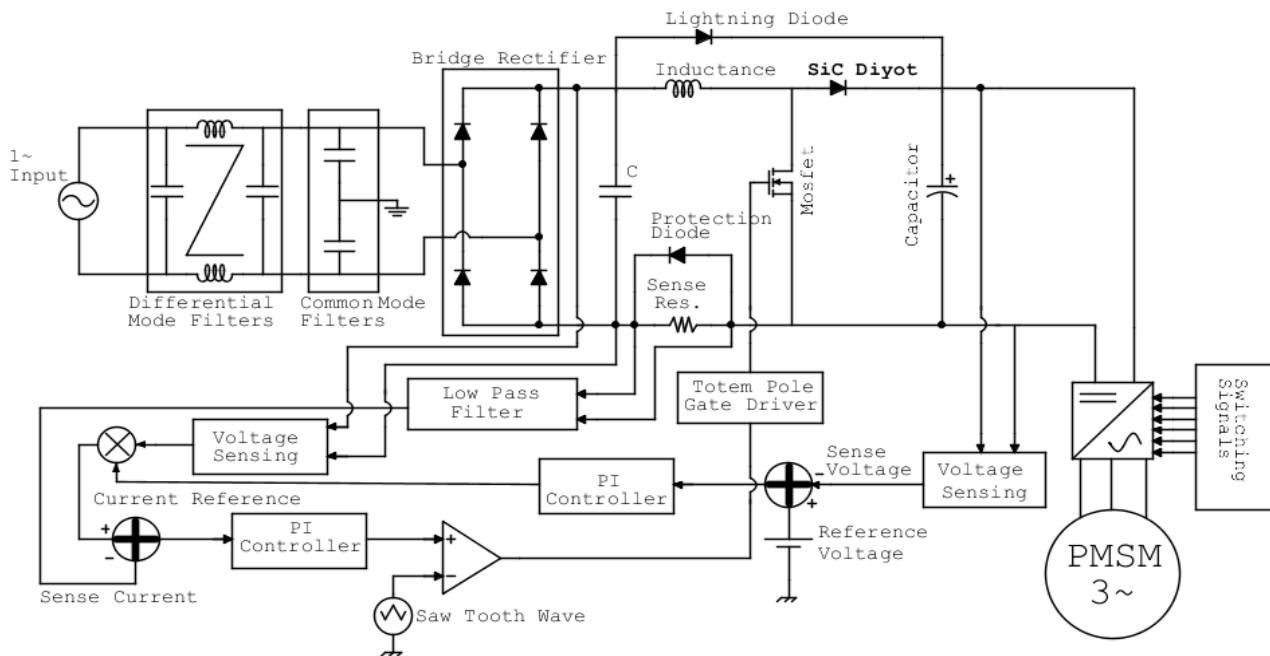


Fig.1. BPFC and its control block diagram

A. BPFC Controller Design

The output dc bar voltage will be oscillated in a certain range as the average value is 390V, V_o , and the voltage divider is used in the circuit so that it reduces the output DC bus voltage to 2.5V. The oscillations on the output voltage may lead to system instability. For this reason, as shown in Figure 2, the system stability is increased by connecting a parallel 470pF capacitor (C_{o1}) to resistance. In order to keep the output voltage constant, compensation is done by using PI controller. The difference between the reference output voltage and the measured output voltage is compensated by the PI controller, which gives the current amplitude reference value.

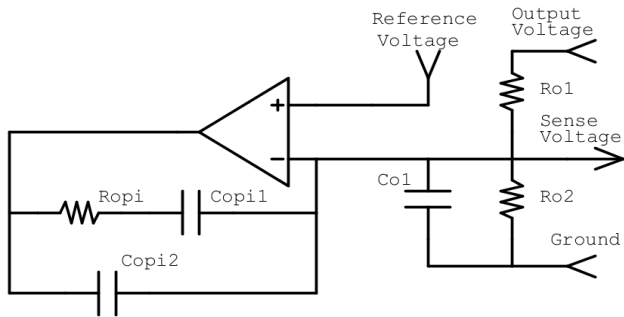


Fig.2. Output voltage sense circuit and PI controller

The FAN6982 IC is used in the study and the variables given by the IC for the PI controller account are given below. In Equation (3), K_{max} is the ratio between the maximum allowed output power and the nominal output power, which is 1.3 for this study. The output current (I_o) is 2.95A and the output capacitance (C_o) is selected as 420 μ F as will be discussed in the next sections. The cut-off frequencies of PI controller are 20Hz and 50Hz. G_{MV} is an error amplifier, which is constant and $70 \cdot 10^6$. According to, Equation (4), (5) and (6), C_{op1} , R_{op1} and C_{op2} are calculated 47nF, 170 k Ω and 18nF, respectively.

$$K_{max} = P_{o,max} / P_o \quad (3)$$

$$C_{op1} = \frac{G_{MV} \cdot I_o \cdot K_{max}}{5 \cdot C_o \cdot (2 \cdot \pi \cdot f_{VC})^2} \cdot \frac{2.5}{V_o} \quad (4)$$

$$R_{op1} = \frac{1}{2 \cdot \pi \cdot f_{VC} \cdot C_{op1}} \quad (5)$$

$$C_{op2} = \frac{1}{2 \cdot \pi \cdot f_{VP} \cdot R_{op1}} \quad (6)$$

A sense resistance whose value does not change importantly with temperature (<100 ppm, temperature coefficient) should be chosen to read the inductance current. The sense resistance is one of the most critical points in the reliability of the system and the power rating of it should be chosen appropriately. With Equation (7), the effective value of the current passing through the inductance for the lowest input voltage of 185V is calculated as 6.5A, and for the 66m Ω sense resistance, 2.77W power loss will be according to Equation (8). η is efficiency of system.

$$I_{L,rms} = \frac{P_o}{V_{in(min)} \cdot \eta} \quad (7)$$

$$P_{loss,sense} = I_{L,rms}^2 \cdot R_{sense} \quad (8)$$

As shown in Figure 3, diodes connected in reverse parallel to the sense resistance are added to protect it from overcurrent (lightning, etc.). Because the voltage drop across this diode is greater than the voltage drops across the sense resistor, the diode will not switch on - (up to 1,150W output power, P_o) during normal operation. Due to the sense current that has a noise, it is necessary to use a low-pass filter to suppress these noises. This filter is extremely critical, as the time constant of the filter increases, the system stability increases but the capacitive increases and $\cos\phi$ goes away from 1.

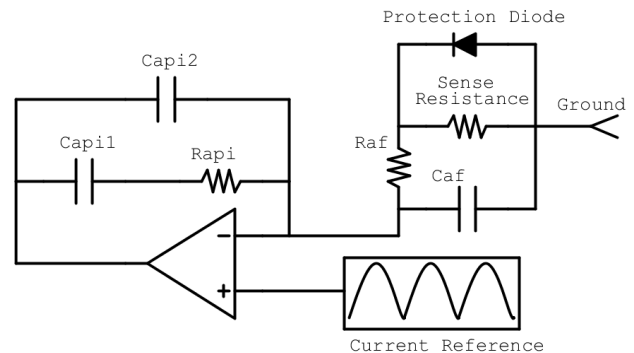


Fig.3. Current sense filter

The output voltage error is compensated by the PI controller as described in the previous section and the reference current value waveform is obtained by multiplying the input voltage shape by the current amplitude value given by PI controller. The difference between the sense current and the reference current is compensated again by the PI controller and the obtained signal is compared with the sawtooth wave to obtain the pulse width modulation signal to be applied to the MOSFET. f_{IC} is cut-off frequency of the PI controller, which should be selected times less than the switching frequency, so it is 6600Hz and, f_{IP} 60kHz in this study. G_{MI} is error amplifier, whose value is $88 \cdot 10^{-6}$. According to Equation (9), (10), (11) and (12), R_{api} , C_{api1} and C_{api2} seen in Figure 3 are selected 220 Ω , 330nF and 12nF, respectively.

$$\left| \frac{\hat{V}_{CS}}{\hat{V}_{IEA}} \right|_{@f=f_{ic}} = \frac{R_{olcme} \cdot V_o}{V_{RAMP} \cdot 2 \cdot \pi \cdot f_{ic} \cdot L} \quad (9)$$

$$R_{api} = \frac{1}{G_{MI} \cdot \left| \frac{\hat{V}_{CS}}{\hat{V}_{IEA}} \right|_{@f=f_{ic}}} \quad (10)$$

$$C_{api1} = \frac{1}{R_{api} \cdot 2 \cdot \pi \cdot \frac{f_{IC}}{3}} \quad (11)$$

$$C_{api2} = \frac{1}{R_{api} \cdot 2 \cdot \pi \cdot f_{IP}} \quad (12)$$

B. BPFC Inductance Calculation and Design

Because the dimensions such as size, loss and price are the determining factors for the inductance design, a core material selection must be made first. The use of ferrite cores is not preferred due to the fact that the fringing flux occurring in the air-gap is due to the noise propagation to other elements. In addition, the ferrite material core will lose its inductance function when it reaches the critical magnetic field density. For this reason, instead of a ferrite material, a powder core material is used. Since the saturation point of the powder core is higher than the saturation point of the ferrite core, smaller volume and mass inductances can be made by the powder core and emitted noise is lowered when the powder core is used. With a toroidal core, the inductance with high inductance value can be designed in unit volume. As the load increases, the air spaces in the powder core nest get irregularly saturated and inductances with the powder core do not have a constant magnetic permeability. As the saturation air particles increase, the magnetic reactivity and hence the inductance are reduced [7]. Because of these properties, Magnetics Company's "KoolMu" powder core is chosen and used in design. If the current on the inductance is chosen to have a fluctuation of 50%, the inductance value of Equation (13) will be set to 300 μ H. At the input voltage of 185V, the peak value of the inductance current will be 13.75A and the current ripple will be 5.5A.

The inductance design using Magnetics-KoolMu 77439 coded powder core is achieved with this inductance to obtain an inductance of 135nH in one turn wire wound, with an inductance value of 486H with 60 turns. This is valid when no current flows through the inductance value and the inductance value will decrease with loading. Using the company's "Magnetics Curve Calculation Tool", an inductance value of 296 μ H is obtained with 60 turns full load KoolMu 77439, which gives the value determined from Equation 13 [8], T is period of switching.

$$L = \frac{1}{\% Dalgallik_{L}} \cdot \frac{V_{in(min)}^2}{P_o} \cdot \left(1 - \frac{\sqrt{2} \cdot V_{in(min)}}{V_o} \right) \cdot T \quad (13)$$

$$H_{max} = \frac{I_{L,max} \cdot N}{l_e} \cdot \frac{4 \cdot \pi}{1000} \quad (14)$$

$$H_{min} = \frac{I_{L,min} \cdot N}{l_e} \cdot \frac{4 \cdot \pi}{1000} \quad (15)$$

The maximum value of the magnetic field strength, H_{max} , is calculated to be 96.53 Oersted according to Equation (14), minimum value of the magnetic field strength, H_{min} , is calculated to be 57,91 Oersted according to Equation (15). B_{max} 4,800 Gauss corresponding to H_{max} and B_{min} 3,300 Gauss corresponding to H_{min} are designated as "normal magnetization curves" in the magnetics catalog [6]. The flux and frequency-

dependent core loss given by the manufacturer Magnetics is given in Equation (16) and is calculated to be 5.433W, f is frequency of switching and V_{core} is volume of the core.

$$P_{loss,core} = \frac{(B_{max} - B_{min})^2}{4} \cdot f^{1.46} \cdot V_{core} \quad (16)$$

Depending on the current density of the windings, 1.5 mm diameter wire copper coil is used and a cross section area of 1.76 mm² is provided and the total length of copper wire used is approximately 6.23 meters. The conductor wire resistance is calculated as Equation (17) based on the specific resistance of the length and the copper at 100°C, and is determined as 71m Ω . Coil losses are calculated using the effective value of the coil current according to Equation (18), ρ is resistivity of copper. The effective value of the coil current for the input voltage of 185V will be 6.5A, resulting in a loss of 3W. In total, a power loss of 8.432 watts was determined.

$$R_{copper} = \frac{\rho \cdot l_{copper}}{A_{copper}} \quad (17)$$

$$P_{copper} = I_{L,RMS}^2 \cdot R_{copper} \quad (18)$$

C. MOSFET Selection and Losses Analysis

In the case of BPFC, the body diode parallel to the MOSFET never switches on, so it is only necessary to focus on the MOSFET. The current value of the MOSFET should be selected according to the lowest value of the input voltage, considering the highest junction temperature. The low value of C_{oss} and the transmission resistance of the MOSFET to be selected and the fast switching is very important in terms of efficiency.

The effective value of the current passing through the MOSFET can be calculated using Equation (19) and the maximum current value of the MOSFET is 13.75A. This current value must be met by the MOSFET even at a temperature of 100°C. The effective value of the MOSFET current according to Equation (19) is calculated as 4.08A. Conduction loss can be calculated by Equation (20), considering the relation of the conduction resistance with temperature. The equations (21), (22) and (23) are used for the turn-off losses in the case of equations (24) and (25). The parameters seen in Equation (20), (21), (22), (24) and (25) can be found from used MOSFET datasheet.

$$I_{MOS,RMS} = \frac{P_o}{V_{in,RMS}} \cdot \sqrt{1 - \frac{8 \cdot \sqrt{2} \cdot V_{in,RMS}}{3 \cdot \pi \cdot V_o}} \quad (19)$$

$$P_{S,cond} = I_{MOS,RMS}^2 \cdot R_{on(100^\circ)} \quad (20)$$

$$t_{on} = C_{iss} \cdot R_g \cdot \ln \left(\frac{V_g - V_{th}}{V_g - V_{pl}} \right) + C_{rss} \cdot R_g \cdot \left(\frac{V_o - V_{pl}}{V_g - V_{pl}} \right) \quad (21)$$

$$C_{rss} = \frac{Q_{gd}}{V_o} \quad (22)$$

$$P_{s,on} = 0.5 \cdot I_{L,ort} \cdot V_o \cdot t_{on} \cdot f \quad (23)$$

$$t_{off} = C_{rss} \cdot R_g \cdot \frac{V_o - V_{pl}}{V_{pl}} + C_{iss} \cdot R_g \cdot \ln \left(\frac{V_{pl}}{V_{th}} \right) \quad (24)$$

$$P_{s,off} = 0.5 \cdot I_{L,ort} \cdot V_o \cdot t_{off} \cdot f \quad (25)$$

Calculation of turn-off switching losses by conventional methods is given in Equation (25). In addition, C_{oss} behaves like a non-linear capacitive snubber, so the turn-off switching losses will be lower than the calculated value. Equations (26) where MOSFET is not in conduction, equation (27) gate losses are calculated. The sum of the losses calculated in Equation (23), (25), (26) and (27) is calculated as seen in Equation (28), and the total losses are obtained.

$$P_{S,OFF} = E_{OSS} \cdot f \quad (26)$$

$$P_{S,Gate} = V_g \cdot Q_g \cdot f \quad (27)$$

$$P_{S,Total} = P_{S,cond} + P_{S,ON} + P_{S,OFF} + P_{S,Gate} \quad (28)$$

D. Diode Selection

The diode is one of the most critical elements as the diodes in BPFCS produce high values of reverse current (I_{rrm}) as they go (depending on the slope of the current during turn-on time). Since the reverse current I_{rrm} passes through the MOSFET at the time of turn-on (t_{on}) of the MOSFET, it causes both the loss of switching and the problems of electromagnetic interference (EMI). Diode reverse recovery times (t_{on} , t_a , t_b), I_{rrm} and MOSFET current are shown in Fig. 4. As can be seen, the I_{rrm} current increases the MOSFET current. Using the totem pole structure, the MOSFET's t_{on} duration can be increased, so that the EMI generated by the reverse current I_{rrm} is reduced, but the switching losses are also increased in the same way [9].

The maximum value of the inverse recovery current is obtained by the Equation (29) and the decreasing curve of the diode current is obtained by the Equation (30). The duration of change from the zero current to $-I_{rrm}$ by the Equation (31) is calculated again. The values of Q_{rr} and t_{rr} are obtained from the manufacturer's diode information book and $I_{d,peak}$ is equal to the peak value of the inductance current, of course. As the Q_{rr} value increases, the turn-on switching loss of the MOSFET appears to increase significantly.

$$I_{rrm} = \frac{2 \cdot Q_{rr}}{t_{on}} \quad (29)$$

$$\frac{dI_f}{dt} = \frac{I_{d,peak}}{t_{on}} \quad (30)$$

$$t_a = \frac{I_{rrm}}{\frac{dI_f}{dt}} \quad (31)$$

$$t_b = t_{rr} - t_a \quad (32)$$

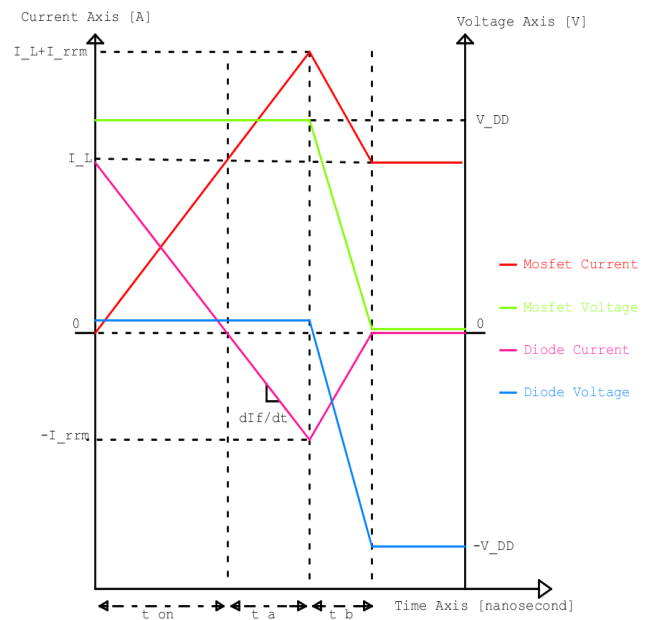


Figure 4: Diode inverse recovery current, MOSFET current and intervals durations

The average value of the diode current according to the BPFCS structure is equal to the average of the load current. The average of the diode current with Equation (33), the diode conduction losses with Equation (34), the switching losses with Equation (35) and the diode total losses with Equation (36) are obtained. V_f is voltage drop of used diode, it can be found from used diode datasheet.

It has been observed both theoretically and experimentally that the problems mentioned above are not able to be solved by the use of conventional silicon diodes in the system. For this reason, Silicon Carbide (SiC) diodes with very low reverse recovery times and currents are preferred in the BPFCS. The recovery charge of SiC diodes is small enough not to be compared with the reverse recovery charge of silicon diodes. SiC diodes have other reasons to be used. For instance, these diodes fall in reasonable prices in recent years, their reliability is high, their switching behavior is independent of temperature and they can withstand high temperature values. These superior features make it possible to increase the switching frequency and reduce the EMI level significantly while achieving a circuit with increased efficiency, reduced size and increased power density.

In Table I, loss analysis is performed for 5 different MOSFET elements and in Table II, loss analysis is performed for 6 diode elements, 2 silicon diodes and 4 SiC diodes. Assuming that R_{on} and R_{off} resistances are 15Ω and 30Ω , respectively, the turn-on time for the MOSFET and the turn-off time are calculated using Equation (21) and Equation (24). I_{rrm} with Equation (29), diode switching losses using I_{rrm} with Equation (35) and diode conduction losses with Equation (34) are calculated for each diode element in Table II. After the loss - price optimization is made; it is decided to use ST STC606 SiC diode. It is predicted that this diode will produce $0.37A$ I_{rrm} when going to turn-off. This current value is added to the MOSFET turn-on current as shown in Table I and as shown in

Figure 4, and the total loss is calculated by using Equation (28) for each MOSFET element. After the loss - price optimization, Fairchild decided to use the FCH125N60E MOSFET element. According to the analysis result, it is estimated that the MOSFET element has 21.12W loss during operation and the junction temperature is 59°C. The SiC diode is expected to operate at 7.66W loss.

It is thought that two paradigms should be emphasized. The first is that the resistance values of R_{on} and R_{off} are actually determined after the tests made after the Test Setup is established. In the determination of R_{on} and R_{off} gate resistances, the role of the equations given for MOSFET loss analysis is only in the stage of initial value assignment. The most accurate gate resistance values can only be found by empirical methods because the MOSFET element is a nonlinear element since it has the parasitic capacitances, inductances and resistances of the structure which changes with the operating frequency, the gate voltage, the noise level at the gate voltage, the junction temperature, the Drain - Source Voltage and the quality of the

printed electronic board drawn. For this reason, there is still no exact model in the literature that compares the turn-off and turn-on characteristics of the MOSFET. The second paradigm is related to the diode reverse recovery current model. Before a real reverse current I_{rrm} is recovered and settled zero, it fluctuates around the zero point with decreasing amplitude in the MHz range. This oscillation affects both EMI and increases losses. For this reason, there is no doubt that the reverse recovery current model is also an incomplete model.

It should be preferable to use the TO220 package as much as possible because the parasitic inductance of the TO220 package is less than the parasitic inductance of the TO247 package. On the other hand, the heat dissipation performance of the TO247 package is higher than that of the TO220 package. For this reason, the TO224 package is chosen because the MOSFET losses are greater than 10W and the diode losses are smaller than 10W.

TABLE I
MOSFET LOSSES ANALYSIS ($R_{on}=15\Omega$ and $R_{off}=30\Omega$)

MOSFET	t_{on} [ns]	t_{off} [ns]	$P_{s,con}$ [W]	$P_{s,on}$ [W]	$P_{s,off}$ [W]	P_g [W]	P_{total} [W]	I_{rrm} [A]	ΔT
INFINEON 1	74.931	29.31	1.53	11.40	4.32	0.07	17.32	0.37	7.79
INFINEON 2	34.155	13.06	1.76	5.19	1.93	0.03	8.91	0.37	12.09
INFINEON 3	166.310	22.83	2.07	25.29	3.37	0.10	30.83	0.37	17.57
FAIRCHILD 1	107.019	21.29	1.61	16.28	3.14	0.10	21.12	0.37	9.50
FAIRCHILD 2	115.328	32.40	1.60	17.54	4.78	0.10	24.03	0.37	10.81

TABLE II
DIODE LOSSES ANALYSIS

	Diode	Q_{rr} (nC) (130A/nS)	P_{con} [W]	t_{rr} [ns]	dI/dt [A/ns]	I_{rrm} [A]	t_a [ns]	t_{fb} [ns]	P_{switch} [W]	P_{total} [W]
Silicium Diodes	INFINEON	120.00	6.38	65.0	129	3.24	17.45	47.55	1.57	7.95
	FAIRCHILD	62.00	9.86	17.0	129	2.16	9.02	7.98	0.81	10.67
SiC Diodes	WOLFSPEED	15.00	4.93	8.00	129	0.28	2.18	5.82	0.20	5.13
	INFINEON	10.00	5.80	5.00	129	0.19	1.45	3.55	0.13	5.93
	ROHM	9.00	4.50	12.0	129	0.17	1.31	10.69	0.12	4.61
	ST	20.00	7.40	23.0	129	0.37	2.91	20.09	0.26	7.66

E. BPFC Capacitor Selection

In the BPFC, the value of the C_o capacitor is determined by the amount of oscillation of the output voltage. The average of the output voltage is 390V, and according to Equation (37), a voltage swing of about 24V with a capacity of 420μF will occur. In spite of $\Delta V_o = 6\%$, it is decided to use 420μF capacitor considering cost and volume optimization. The serial parasitic resistance value for DC link capacitor according to Equation (38) is obtained as 1.136 Ω. The ambient temperature of this capacitor is 85°C, the loss factor (DF) value is 0.15, the maximum effective value of the current to pass is 1.55 A and the tolerance is 20%. f_{grid} is frequency of grid.

$$C_o \geq \frac{P_o}{2 \cdot \pi \cdot f_{grid} \cdot \Delta V_o \cdot V_o} \tag{37}$$

$$ESR = \frac{DF}{2 \cdot \pi \cdot f_{grid} \cdot C_o} \tag{38}$$

The riskiest component of the life cycle of BPFCs is the DC bus capacitor, which determines the circuit life. For this reason, the lifetime of the capacitor must be calculated appropriately and the selection must be made accordingly. In practice, the system will be placed in the basement so that the BPFC will work in a water booster. In summer the basement can have an ambient temperature of 50°C (T_0). The information booklet of the capacitor to be used is provided with a working guarantee

of 85 hours (T_{max}) ambient temperature of 3000 hours ($LIFETIME_0$). When calculated according to Equation. (39), this capacitor has been determined to have a life of 33,000 hours (approximately 7.5 years) [10].

$$LIFETIME = LIFETIME_0 \cdot 2^{\frac{T_{max}-T_0}{10}} \quad (39)$$

The effective current of the capacitor is obtained by using Equation (40), and the effective value of the current to pass through the capacitor when the input voltage is 185V is determined as 3.8A. According to Equation (41), the amount of power loss in the capacitor is calculated.

$$I_{C_{O,RMS}} = \sqrt{\frac{8 \cdot \sqrt{2} \cdot P_o^2}{3 \cdot \pi \cdot V_{in(min)} \cdot V_o} - \frac{P_o^2}{V_o^2}} \quad (40)$$

$$P_{C_o} = I_{C_{O,RMS}}^2 \cdot ESR \quad (41)$$

It is important to choose a capacitor that will guarantee the effective value of the current to pass through the capacitor, otherwise the life of the capacitor will decrease rapidly.

According to the datasheet of the selected capacitor, 1.55 A is guaranteed for a frequency of 120Hz and an ambient temperature of 85°C. Because the application system will operate at approximately 50°C, this capacitor can withstand currents greater than 1.55A in the datasheet. When the information from the manufacturer is multiplied by the temperature coefficient of 2.42 at 1.55A, this capacity is calculated to be at most 3.75A at 50°C ambient temperature.

The capacitor current is obtained at the full load and the lowest input voltage value in the PSIM simulation program, then this capacitor current is separated to components in accordance with frequency by using Fourier Transform. These current components regard to frequency are given in Table III. The capacitor current components are multiplied by frequency coefficients received from manufacturer, these frequency coefficients are given in Table III. After the multiplications, the products are summed, and the result shown in Table III is calculated as 3.418A. Since the value of 3.418A is lower than the previously calculated value of 3.75A, it is estimated that this capacitor is within safe limits.

TABLE III
FREQUENCY AND CAPACITOR CURRENT RIPPLE RELATION

Frequency	Current [A]	Frequency Coefficients	Frequency coefficient times current [A]
100 Hz	1.944	1.041	2.023
10 kHz	1.698	0.709	1.205
50 kHz and over	0.272	0.699	0.19
TOTAL			3.418

F. Bridge Rectifier Selection

In BPFC, one-phase line voltage is rectified by full-wave (bridge) uncontrolled rectifier. Two diodes always conduct during period. For this reason, the power loss is as much as the products of the voltage drop across the two diodes and the average current. The average current of the bridge rectifier with Equation (42) and power loss with Equation (43) are calculated. Although the amount of loss in the bridge rectifier and the number of semiconductors can be decreased by using bridgeless power factor correcting circuit, but this circuit structure causes EMI to increase. In higher power applications, the bridgeless-interleaved power factor correction circuits can be used to increase the efficiency, they also reduce the magnitude of the input current harmonics and the capacitor voltage fluctuation, but this type of circuitry results in a complex build with the increase the number of components [11].

$$I_{average} = \frac{2}{\pi} \cdot \frac{\sqrt{2} \cdot P_o}{V_{in,min}} \quad (42)$$

$$P_{bridge} = 2 \cdot I_{average} \cdot V_{drop} \quad (43)$$

G. MOSFET Gate Driver Design

The maximum gate current value that the FAN6982 IC used in the operation can provide is 500mA. This is not a value that is large enough to allow the gate current of the MOSFET to turn-on and turn-off at the desired speeds. Therefore, the

maximum turn-on and turn-off currents are increased by installing the Totem Pole structure shown in Fig. 5. As the maximum current of NPN and PNP BJTs is 1,500mA, the maximum transmission and cutting current is increased to 1500mA.

In Figure 5, the R_{g1} resistance limits and protects the PWM source, the R_{g2} resistance provides high impedance between base and collector, and the R_{g5} termination resistance limits oscillations in the gate circuit of totem pole. Following the experiments, the R_{g3} (R_{on}) resistance that determines the t_{on} time is set to 15Ω, and the R_{g4} (R_{off}) resistance that sets the t_{off} time is set to 30Ω.

H. Design of Printed Circuit Board and Hardware Implementation

PCB design is done using Altium Designer drawing program. First of all, all the elements are added to the drawing program with their actual dimensions. This avoids unnecessary gaps between elements, avoiding extra PCB lead inductance and copper resistances as much as possible. Double-layer PCB drawing is done; the necessary jumpers are passed from the second surface. With the use of a mask and an inner casing, the lifetime of the circuit is increased and the soldering problem that can occur during the building is minimized.

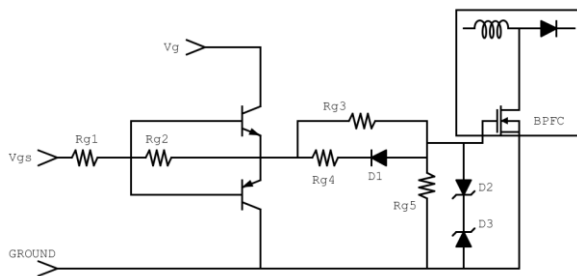


Figure 5: Totem pole gate circuit

One of the factors to be considered in the design and drawing of the PCB is the determination of cycles with high current change (di/dt) and points with high voltage change (dv/dt). The high di/dt current loop is as shown in Figure 6 (a). The parasitic inductances in this cycle are the ones that induce parasitic voltage. For this reason, a capacitor of 100 nF should be added to suppress high frequency components parallel to the output capacitance. Thus, the MOSFET, SiC diode and 100nF capacitances can be designed as close to each other as possible and the parasitic inductance value is reduced as much as possible. The high dv/dt area is shown in Figure 6 (b), where the parasitic capacitances in this region cause noise currents to be generated. PCB design should be made to prevent these areas from forming capacities with ground, earth or other elements. Another factor to note is that the FAN6982 IC's ground used and BPFIC's ground must be separated from each other and connected to each other only at one point. In this way, the IC which produces the switching signal will be affected at least from the ground's voltage collapse or voltage rise. In addition, remarkable effects have also been observed when the ground point and the heatsink are connected each other in the design [12].

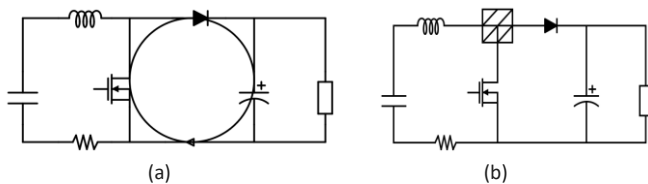


Figure 6: (a) High di/dt loop (b) High dv/dt node

III. HARDWARE IMPLEMENTATION AND EXPERIMENTAL RESULTS

The PCB electronic circuit designed with Altium Designer program has been printed. The figure of the experimental setup which is realized by hardware is shown in Figure 7. Measurements are performed using Tektronix 2024 as oscilloscope and Fluke 80i as current probe. Figure 8 shows the inductance current and input voltage waveforms when the input voltage is 185V. As can be seen, the effective value of the inductance current is 6.5A as expected. The peak value exceeds the value of 13A and the inductance fluctuation is around 45%, which agrees with the values obtained by analytical calculations. Figure 9 shows the input voltage and input current waveforms when the input voltage is 164V. As can be seen, there is no phase difference between the input current and the input voltage and the noises on the input current is suppressed.

The effective value of the input current is about 7.4A and the input power is about 1.213kW. Figure 10 shows the output voltage and output current obtained experimentally. The output voltage fluctuation is around 22V and the calculated value is very close. Similar to the output voltage, the output current has also ripple at 100Hz. The output voltage average is 400V and the output current average is 2.88A, and the output power in this case is 1.152kW.

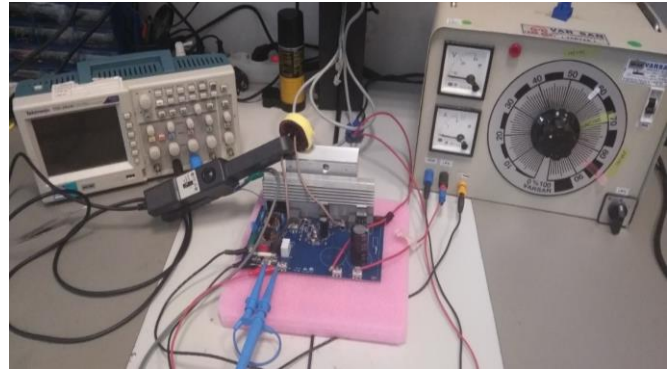


Figure 7: Experimental setup

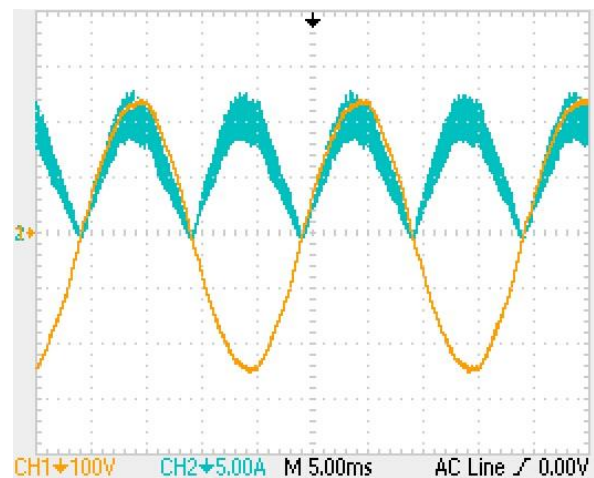


Figure 8: 185V-1,150W – Input voltage (Yellow Line) - inductance current waveforms (Green Line)

Experimental results and simulation results obtained in LTSpice are compared and similarities are observed. Using the LTSpice program, the non-ideal behavior of the switching elements is observed in obtaining the simulation results. In Figure 11, the relationship between input voltage variation and efficiency is measured and compared both in simulation environment and in experimental results. When the results are examined, it is seen that the efficiency is released at 95.5% levels. As the input voltage increases, the required input current value decreases and the efficiency increases at marginal amount.

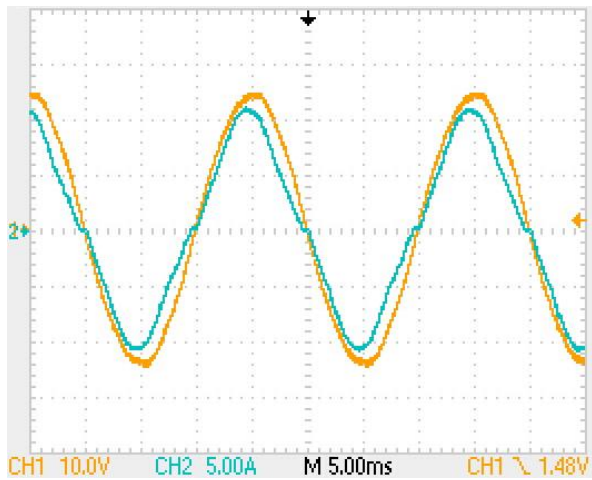


Figure 9: 164V-1,150W – Input voltage (Yellow Line) - input current waveforms (Green Line)

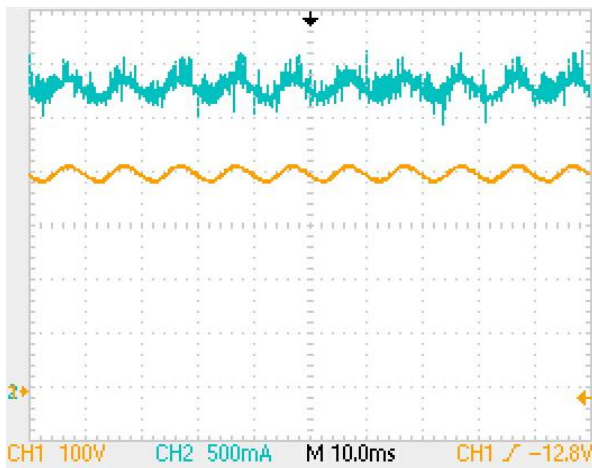


Figure 10: Output voltage (Yellow Line) - current waveforms (Green Line)

The difference of 1.7% between the simulation results and the experimental results can be explained by the lack of the switching loss models in the LTSpice and the modeling of the inductance iron losses with a constant parasitic resistance in the LTSpice program. In Figure 12, the relationship between loading rate and efficiency obtained both experimentally and in LTSpice environment. Even at low load levels, the efficiency is not lower than the 93% level. Thus, it is shown that there is no significant change in efficiency even at low power requirements.

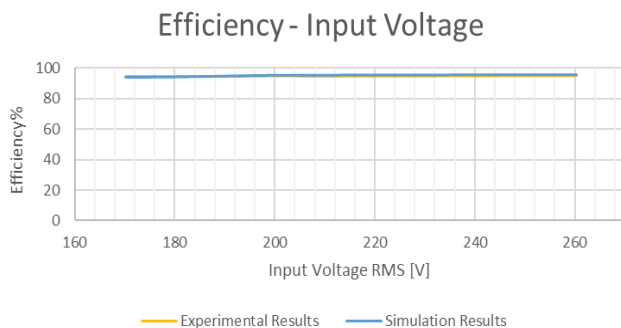


Figure 11: Simulation and experimental efficiency results according to input voltage RMS value

In Figure 13, the total loss analysis is given when the input voltage is 230V. According to this analysis, it is seen that MOSFET is the most lost element with power loss of 21.3W. Then, 9.22W bridge rectifier, 6.05W inductance, 7.6W SiC diode and 10,22W loss capacitor are listed as other important loss components. The total loss amount is around 56W.

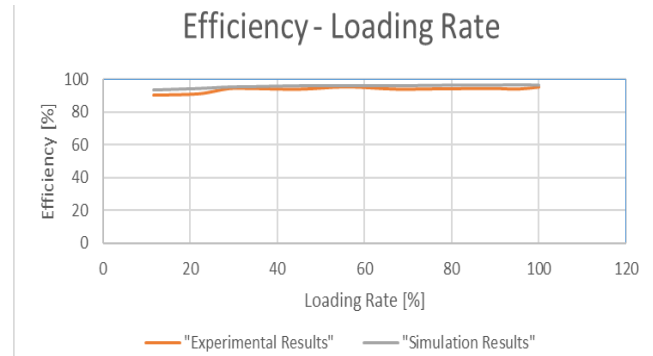


Figure 12: Simulation and experimental efficiency results according to loading rate

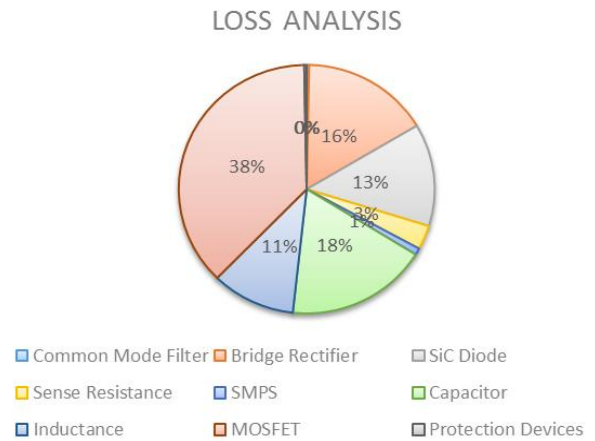


Figure 13: Components losses analysis

IV. CONCLUSION

Cost and efficiency optimization with BPFC has been carried out to design an active filter with increased power density. A detailed loss analysis is performed for each element and the SiC diode reverse recovery current is included in the loss analysis. By using the SiC diode, the reverse recovery current is limited and the efficiency increase is ensured. The analytical equations are given for the maximum current flowing through the elements and the maximum amount of voltage and verified with the model created in the PSIM simulation environment. In order to do losses analysis in the most accurate way, the LTSpice model is constructed. The Fourier analysis of the capacitor current is found in the PSIM environment. The printed circuit board is performed with the Altium Designer program and the experimental results obtained by hardware implementation are compared with the simulation results and verified by checking their compatibility with each other. According to simulation and experiments, it is observed that the system operates between 95% and 95.5% efficiency. The following

recommendations can be applied so that the system to operate at higher total efficiency can be obtained. In the later stages of the design work will be carried out and analyzed.

- BPF can be changed with the topology that are able to do soft switching during turn-on time so as to eliminate $P_{s,on}$ losses that are 16W in this study [13].
- A MOSFET that has lower conduction resistance can be selected so as to reduce $P_{s,on}$ losses that is 1.61W in this study and also this MOSFET can be paralleled even if less conduction losses are desired.
- A new capacitor that has more capacitance can be replaced with the used 420V, 420 μ F capacitor that has 10.22W losses, thus voltage ripple and ESR can be decreased. Moreover, this capacitor can be paralleled in order to have less capacitor losses, but this also reduces the power density of system.
- To get rid of the bridge rectifier losses which are 9.22W, bridgeless PFC topology can be used, but this leads to increase in the EMI level and thus volume of EMI filters.

REFERENCES

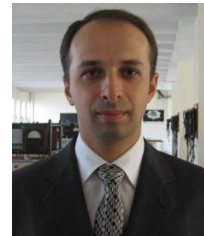
- [1] M. Umemura, *Basic Knowledge of EMC Standards*, 24 Nisan 2017. [Online]. Available: https://product.tdk.com/en/products/emc/guidebook/eemc_basic_04.pdf.
- [2] C. Kocatepe, *Elektrik Tesislerinde Harmonikler*, Birsen Yayınevi, Kasım 2003, İstanbul.
- [3] R. W. Erickson, *Fundamentals of Power Electronics*, Kluwer Academic Publishers, 1997.
- [4] L. Po-Wa et al., "Steady-state analysis of an interleaved boost converter with coupled inductors", *IEEE Trans. Ind. Electron.* vol. 47, no. 4, pp. 787-795, 2000.
- [5] Raggl T. Nussbaumer, G. Doerig, J. Biela, J. W. Kolar, "Comprehensive design and optimization of a high power density single phase boost PFC", *IEEE Trans. Ind. Electron.*, vol. 56, no. 7, pp. 2574-2587, Jul. 2009.
- [6] S. A. Rahman, F. Stückler, K. Siu, "PFC boost converter design guide", 24 Nisan 2017. [Online]. Available: http://www.infineon.com/dgdl/InfineonApplicationNote_PFCCMBBoostConverterDesignGuide-AN-v02_00EN.pdf?filed=5546d4624a56eed8014a62c75a923b05.
- [7] Magnetics Powder Core Catalog 2015, 24 Nisan 2017. [Online]. Available: <https://www.mag-inc.com/getattachment/Design/Design-Guides/2015-Magnetics-Powder-Core-Catalog.pdf?lang=en-US>.
- [8] Magnetics Inductance Design Tool, 24 Nisan 2017. [Online]. Available: <https://www.mag-inc.com/Design/Design-Tools/Inductor-Design>.
- [9] S. Bin, L. Zhengyu, "An interleaved totem-pole boost bridgeless rectifier with reduced reverse-recovery problems for power factor correction", *IEEE Trans. Power Electron.*, vol. 25, no. 6, pp. 1406-1415, Jun. 2010.
- [10] Capacitor Life Calculation Tool, 24 Nisan 2017. [Online]. Available: <http://www.illinoiscapacitor.com/tech-center/life-calculators.aspx>.
- [11] C. N. Ho, R. T. Li ; K. K. Siu, "Active virtual ground — bridgeless PFC topology", *IEEE Trans. Power Electron.*, vol. 32, no. 32, pp. 6206 - 6218, August 2017.
- [12] G. Spiazzi, *Active PFC Boost Rectifier*, 24 Nisan 2017. [Online]. Available: <http://www.dsce.fee.unicamp.br/~antenor/pdf/EMC2.pdf>.
- [13] Y. Jang, D. L. Dillman, M. M. Jovanović, "A New Soft-Switched PFC Boost Rectifier with Integrated Flyback Converter for Stand-by Power", 24 Nisan 2017. [Online]. Available: <http://www.deltartp.com/dpel/dpel-conferencepapers/pfc-with-im.pdf>.

BIOGRAPHIES



BEKİR FINCAN received the B.S. degree from the Electrical Engineering Department, Istanbul Technical University (ITU), Istanbul, Turkey, in 2012, and the M.S. degrees from the same department in 2015. He is now PhD student at the same University.

He is currently a research assistant at the Istanbul Technical University. His research interests power electronics, especially DC/DC converters.



MURAT YILMAZ received the B.S. degree from the Electrical Engineering Department, Istanbul Technical University (ITU), Istanbul, Turkey, in 1995, and the M.S. and Ph.D. degrees from the same university, in 1999 and 2005, respectively.

He is currently an Assistant Professor at the Istanbul Technical University. His research interests power electronics and electrical machines design, control, optimization, and reliability modeling in motor drives and electric drive vehicles including electric, hybrid,

and plug-in hybrid electric vehicles.



ALPER GOYNUSEN received the B.S. degree from the Electrical Engineering Department, Yildiz Technical University (YTU), Istanbul, Turkey and the M.S. degree from Electrical Machines and Power Electronics Engineering program from the same department and university in 2011 respectively.

He is currently a senior design engineer in Pavotek Electronics Design Company, and formerly worked in Arçelik and AVL as a design engineer.

His research interests are power electronics and motor drive circuits, analog electronics, soft switching and resonant circuits, analog and digital control theories.



HAYRI KEREM ERENAY received B.S. degree from Electrical Engineering and Electronics, Bosphorus University (BU), Istanbul, Turkey, 1995 and M.S. degree from Bosphorus University Electrical Engineering and Electronics in 1998.

Worked from 1995 – 2013 in Arçelik R&D, power electronics team, motor control and motor based sensing and identification.

From 2014 until now, he is business line manager in power systems group in Pavotek Electronics Design

Company, working on motor control and power supply systems.

Design of Bluetooth Low Energy Based Indoor Positioning System

D. Taşkın

Abstract— Nowadays, there is an increasing demand for indoor positioning systems as services based on location are very important in mobile applications. Since Global Positioning System (GPS) makes only outdoor positioning successful, there is a need of new approaches for indoor positioning systems. Some techniques on indoor positioning systems have been proposed in this scope, but they have not reached to the success of outdoor systems in terms of speed, consistency and power management. The aim of this study is to develop an indoor positioning system using latest Bluetooth Low Energy (BLE) technology. This system consists of BLE sensor nodes, a mobile device and a mobile application that calculates indoor position by measuring the signal levels of the sensor nodes designed. BLE sensor nodes have low power consumption and can be powered by a coin battery. Since most consumers have a mobile phone today, the system can be used easily by installing a mobile application.

Index Terms— Indoor positioning, BLE, CC254x, Bluetooth Stack, RSSI.

I. INTRODUCTION

IN RECENT YEARS, the focus of navigation systems has shifted to indoor venues where people spend almost all of their free time. These systems can identify people and track their indoor position. The scope of these systems notably oriented for use in hospitals, malls, museums to monitor people and their behavior, to enhance their satisfaction, and to provide navigation ability. These systems should provide information about location economically and just in time like classical GPS navigation. For instance, an intelligent navigation system guides patients in hospitals or mobile applications make blind people freely discover indoor activities. In other words, an indoor positioning system should provide location-awareness for mobile device users everywhere. Therefore, this study aims to develop accurate and reliable indoor positioning system with power consumption.

This paper is organized as follows: In section 2, the concept of indoor positioning system is presented. In section 3, the newest Bluetooth technology and its properties are described. The developed system is presented in section 4. The experimental results for the proposed system are given in section 5. Finally, section 6 summarizes the study and presents future works.

D. TAŞKIN, Department of Computer Engineering, Trakya University, Edirne, Turkey, (e-mail: deniztaskin@trakya.edu.tr). 

Manuscript received May 8, 2017; accepted July 14, 2017.
DOI: [10.17694/bajece.334388](https://doi.org/10.17694/bajece.334388)

II. INDOOR POSITIONING

The goal of an indoor positioning system is to make indoor locations to be identified by using sensor nodes. This system uses specific location information gathered from sensor nodes for navigation support. This system could find a possible usage in hospitals, universities, museums and shopping malls. Indoor location information can be used for navigation, giving information about a specific place, collecting customers behaves, helping people with limited vision to navigate and connecting people who are in close proximity.

For this purpose, several systems have been developed over the last decade. One of them is based on Wi-Fi technology, which requires many access points and has lack of accuracy [1]. The other developed systems are based on optical, electromagnetic and sound waves [2-6]. They have weak capabilities and drawbacks [7]. Some of these systems can be combined to improve accuracy, which will make the system more expensive [8].

Since Wi-Fi, infrared and ultra-sound based systems are costly and have complex components to be installed, they can be considered as unpractical to commercialize [9, 10].

Bluetooth Low Energy (BLE) is a new technology that can be used for many applications including positioning. BLE has basically focused on lowering the battery use and making the battery usage up to 10 times lesser than that of the classic Bluetooth devices. This specification of BLE gives it a good chance to develop a device, which run on a battery without charging for years like watches, remote control, and health devices. In addition, systems designed based on BLE are economical for commercial applications. These systems use same key components with classic Bluetooth technology except new BLE chipset. This chipset prices are as low as \$2 if they are bought in quantities of thousands. There is also an assumption that the BLE will be available in 90% of the smart phones by 2018. All these factors make the BLE to be a good choice for indoor positioning system.

III. BLUETOOTH TECHNOLOGY

Bluetooth technology gives electronic devices an ability to communicate with each other without wires. Bluetooth communication uses radio waves within the 2.4 GHz license-free ISM (Industrial, scientific and medical) band. Classic Bluetooth is used for short-range wireless communication

between devices in networks where nodes are all mobile. It uses 79 channels on the 2.4 GHz ISM band with a pseudo-random frequency hopping sequence so a master device can establish connection with 7 slave devices simultaneously. Although it is based on low-cost transceiver microchips and designed for low power consumption, its usage and popularity is decreasing against Wi-Fi enabled devices. Note that Wi-Fi enabled devices have wider range, large list of supported security protocols, user-friendly applications and a larger bandwidth.

Bluetooth Special Interest Group (SIG) who manages the Bluetooth specification, lately concerned about these problems and gives this technology a fresh direction by introducing BLE. BLE differs significantly from others classes. While all wired and wireless communications technologies increase their speeds, BLE lowers classical Bluetooth 54 Mbps transfer rate to 0.3 Mbps. Since Wi-Fi and cable based connection solutions are already proved themselves as stabilized and easy to operate for mobile devices, Bluetooth class 4 is designed to achieve another concept. As its name implies, it uses more less power than other Bluetooth standards since peak current not exceeding 15 mA according to the Bluetooth Core Specification. Small amount of data can be transmitted to the host devices without a physical master-slave connection. This means low data rates can be reached by this technology while a small battery lasts for a year [11]. This technology also aims “internet of things” concept. Its main objective is to work for a very long time with a small battery and to enable devices to work with the internet technology where traditionally they have not been able to do in so an efficient way.

IV. OVERVIEW OF BLE ARCHITECTURE

Similar to the older Bluetooth technologies, the latest Bluetooth class operates in the 2.4 GHz ISM band but divides it into 40 channels. Three of these channels are located between the commonly used data channels and used for advertising and service discovery. Except within these advertising channels, there are also 37 channels for transferring data (Figure 1).

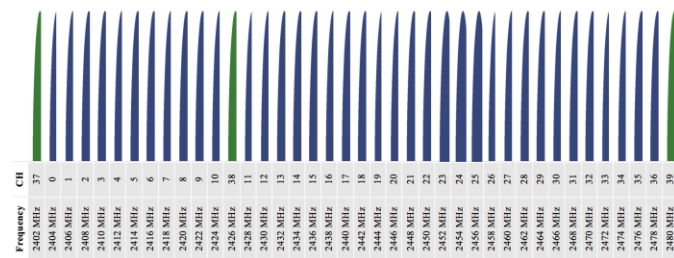


Fig.1. BLE channels, 37 for data transfer (blue), 3 for advertising (green)

According to the Bluetooth Core Specification V4.1, BLE implements an entirely new protocol stack along with new profiles and applications. As shown in Figure 2, this protocol stack consists of two sections.

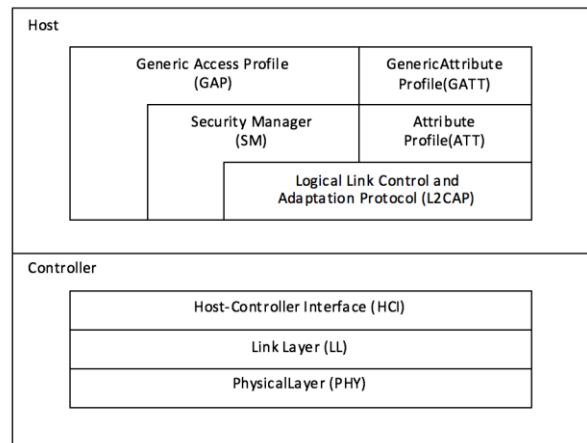


Fig.2. BLE protocol stack architecture

In BLE protocol stack architecture, the controller part is on the lowest layer of the stack and responsible of handling physical hardware signals. This part captures the physical signals in the air band, manages the timing of incoming and outgoing packets and controls the physical level data flow.

The host part of stack consists of application, attribute protocol, security manager and L2CAP properties. L2CAP provides a communication channel for data services between host and controller parts. The L2CAP encapsulates data for the upper service layers. The generic access profile (GAP) is responsible for handling device discovery and connection related services. It gives the ability of implementing different Bluetooth modes like advertising, scanning, etc. to the application layer. The security manager (SM) provides AES (Advanced Encryption Standard) 128-bit encryption engine to be used in authentication, pairing and key distribution. The attribute protocol (ATT) makes a decision about the role of the device. These roles can be master/slave or server/client. Another component is the generic attribute profile (GATT) which is a service framework and responsible for describing the sub-procedures of ATT. It interfaces the application layer to the application profiles. Each attribute profile directly communicates with the specific application and provides data formatting for this application.

In this study, we focus on Texas Instruments’ CC254x BLE stack that offers different system design options to the developer. In this evolution platform, a system application can be combined with Bluetooth stack or the application can run in the separate processor called network processor (Figure 3). In the first option single chip is used for application and BLE stack operations. In the second option, a network processor chip is used in addition to BLE stack chip. These separate units communicate with each other using their serial interfaces. The single device configuration has advantages like hardware cost and energy efficiency. This design concept uses only one chip for Bluetooth radio and application layer. While this method does not have additional communication procedures, system performance is better than previous one. It also consumes less power than the network processor configuration since the

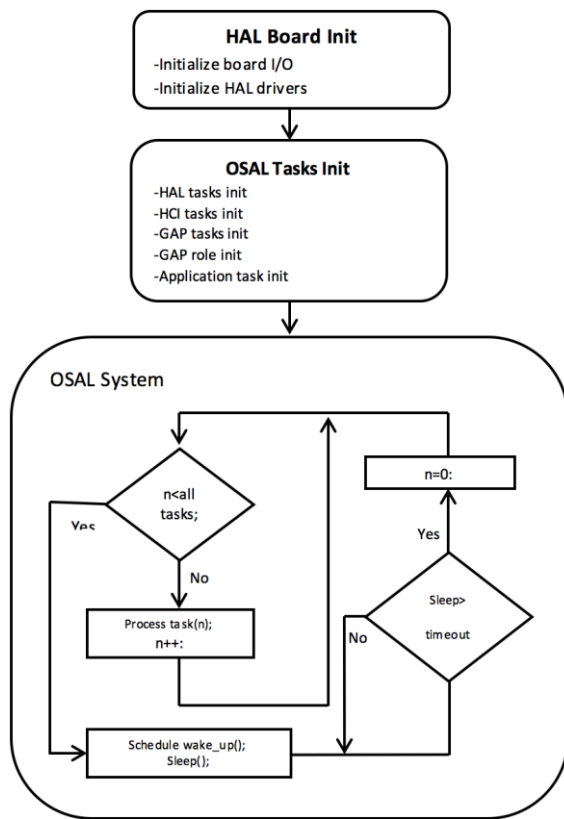


Fig.6. BLE advertiser node embedded software flow chart

HAL of the CC254x provides an interface of abstraction between the physical hardware and software. This development layer is like kernel drivers in Linux operating system and makes developed code more flexible and versatile. If a hardware change is done, only HAL code modification is enough to handle this; protocol stack or application code modification is no longer needed (Figure 6).

We also prepared a special advertisement packet format for this work. This advertisement data format consists of five pieces: data length application signature, software revision, battery level and a unique ID. Unique ID is also divided into four two-byte long pieces: Building ID, Floor ID, Region ID and Sensor ID. Data length is always “0E” since our data packet is 15 bytes long. Application signature is 4 bytes long and is selected as “22, DE, 05, 37”. And a byte is reserved for each software revision and battery level fields. Software revision is constant value and determined by the developed firmware. Battery level is a living value and updated periodically during advertisement. Unique ID field is prepared specifically for this application and consists of Building ID, Floor ID, Region ID and Sensor ID sub fields (Figure 7). Firmware has to specify all the nodes unique. This is important for identifying each node separately and calculating indoor location.

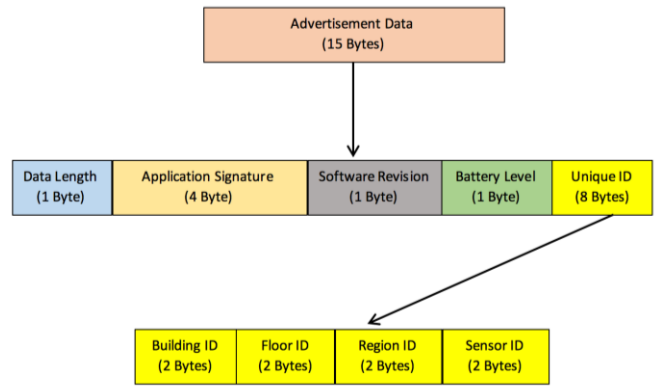


Fig.7. Format of BLE advertisement data

B. Mobile application program

Scanning mode is used in our mobile application program to capture advertisement packets, which are seeded by our BLE advertiser node. The BLE advertiser node starts in Advertise Mode and sends advertisement packet.

As shown in Figure 9, all BLE advertiser nodes have a unique AdvData value. Captured packet structure consists of Access Address, which is always 0x8E89BED6 and 4 bytes long. Advertisement PDU Type is ADV_NON_CONN_IND and Advertisement PDU Header shows that PDU-Length is 21 bytes long. Advertisement unique MAC address and Advertisement Data are 6 bytes and 15 bytes long, respectively. Advertisement data can be used for identifying sensor node. It can identify (28)8 unique nodes. CRC value, 3 bytes long, is calculated by using previous fields. Calculated RSSI level is also added to packet by BLE stack.

Application program uses a background scan engine that extends AsyncTask class. Scan engine captures advertising packets from nearby nodes and stores their UID, RSSI, MAC information in local storage with a timestamp as shown in Table.

Then, another background engine calculates mobile phone’s latest location by using Trilateration method. The basic principle of Trilateration method is that an unknown location (E1) is calculated by using known locations (A, B, C) and signal strength (R1, R2, R3) as shown in Figure 8 [12].

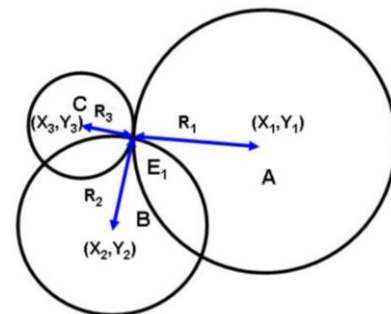


Fig.8. Trilateration method

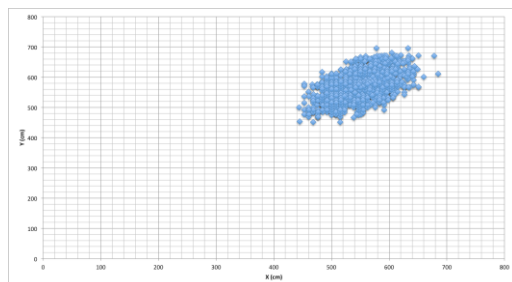
Channel	Access Address	Adv PDU Type	Adv PDU Header				AdvA	AdvData	CRC	RSSI (dBm)
0x25	0x8E89BED6	ADV_NON_CONN_IND	Type	TxAdd	RxAdd	PDU-Length	0xD03972A6B0DC	0E 22 DE 05 37 01 64 00 01 00 01 00 01 00 01	0x93921E	-51
0x25	0x8E89BED6	ADV_NON_CONN_IND	Type	TxAdd	RxAdd	PDU-Length	0xD03972A6B162	0E 22 DE 05 37 01 64 00 01 00 01 00 01 00 02	0x80ED31	-56
0x25	0x8E89BED6	ADV_NON_CONN_IND	Type	TxAdd	RxAdd	PDU-Length	0x9059AF1632AE	0E 22 DE 05 37 01 64 00 01 00 01 00 01 00 03	0x0ACC47	-46

Fig.9. Scan dump of BLE advertiser node

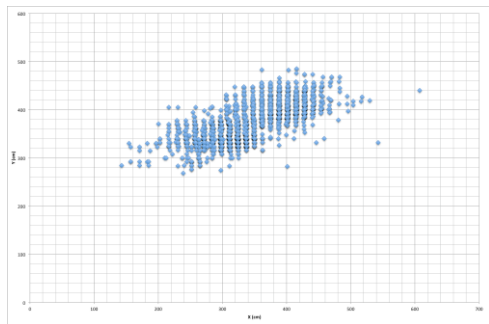
Sensor node positions (X1,Y1), (X2,Y2) and (X3,Y3) are known values and radius values of circles R1, R2, R3 are represented RSSI values. Then, approximate position of E1 point can be calculated by using these parameters [13, 14]. This location information is shown by the application interface in a preloaded indoor map. Since there are building, floor and region information in UID field, these UID fields can be associated with discrete floor plans.

C. Reliability of the measurements

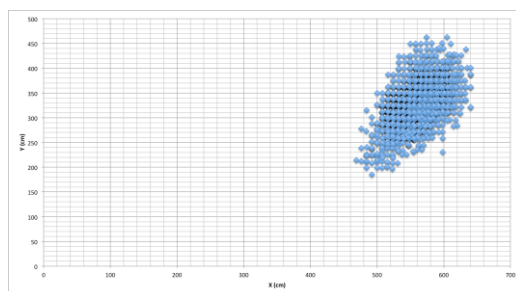
The measured signal level values, like all radio-enabled systems, vary over time depending on the crowd and device’s antenna position.



a) Test point X1=600cm Y1=600



b) Test point X2=400cm Y2=400cm



c) Test point X3=600cm Y3=400cm
Fig.10. Test results

In general, the highest RSSI value that could be measured by the scanner engine is -20dB. This value is gathered by placing a node as close to mobile phone as possible. The lowest RSSI value that could be read is -96dB. The scanner engine ignores the values that are out of these bounds.

To get better results a field study was conducted. Almost two thousand measurements were taken for each test points to calculate the indoor positions by using the RSSI values and trilateration method. The data set for three test points each on different floor of building are shown in Figure 10.

VI. CONCLUSION

In this paper, an indoor positioning system is proposed that consists of BLE advertising nodes and a mobile application program. The program has three parts as scan engine, trilateration processor and a graphical user interface. The advertising nodes are developed with Texas Instruments’ CC2540 Bluetooth Low Energy chip. These nodes are battery powered and act standalone. There is no physical connection between mobile phone and BLE nodes. RSSI signals are used to calculate estimated location of mobile phone. Since BLE nodes are designed to act as an advertiser, there is no need for master-slave connection or link. This also makes this system usable by unlimited mobile phone users simultaneously.

Distributed BLE advertiser nodes (at least three nodes), which can be identified by the application, are placed in a building for the concept of the designed system. By using the designed system, several measurements were done. The number of nodes can be increased to improve the sensitivity of the system. Also, triangulation formula can be extended for this purpose.

We have not offered a calibration scheme for this system since BLE advertisement nodes are identical. However not all mobile phones are the same. A calibration can be performed for all mobile phone brands and these calibration parameters can be used by the mobile application for specific brand.

REFERENCES

- [1] Xiang Z, Song S, Chen J, Wang H, Huang J, Gao X., “A wireless LAN-based indoor positioning technology”, *Ibm Journal of Research and Development* 2004; 48: 617-626.
- [2] Saab SS, Nakad ZS., “A Standalone RFID Indoor Positioning System Using Passive Tags”, *Ieee Transactions on Industrial Electronics* 2011; 58: 1961-1970.
- [3] Yang Y, Zhao YB, Kyas M., “RBGF: Recursively Bounded Grid-Based Filter for Indoor Position Tracking Using Wireless Networks”, *Ieee Communications Letters* 2014; 18: 1234-1237.

- [4] Cheng JJ, Cai YQ, Zhang QY, Cheng JL, Yan CD., "A New Three-Dimensional Indoor Positioning Mechanism Based on Wireless LAN", *Mathematical Problems in Engineering* 2014.
- [5] Su S, Zhao F, Jia HW., "Improved indoor Ultrasonic Positioning for Smartphones Using TDOA", *International Conference Machinery, Electronics and Control Simulation* 2014; 614: 484-489.
- [6] Kim SY, Lee MH, Choi JY., "Indoor positioning system using incident angle detection of infrared sensor", *Journal of Institute of Control, Robotics and Systems* 2010; 16: 991-996.
- [7] Gu YY, Lo A, Niemegeers I., "A Survey of Indoor Positioning Systems for Wireless Personal Networks", *Ieee Communications Surveys and Tutorials* 2009; 11: 13-32.
- [8] Cho JH, Cho MW., "Effective Position Tracking Using B-Spline Surface Equation Based on Wireless Sensor Networks and Passive UHF-RFID", *Ieee Transactions on Instrumentation and Measurement* 2013; 62: 2456-2464.
- [9] Farid Z, Nordin R, Ismail M., "Recent advances in wireless indoor localization techniques and system", *Journal of Computer Systems, Networks, and Communications* 2013.
- [10] Pirzada N, Nayan MY, Subhan F, Hassan MF, Khan MA., "Comparative Analysis of Active and Passive Indoor Localization Systems", *AASRI Procedia* 2013; 5: 92-97.
- [11] Taşkın D., Taşkın C., Çetintav I., "BLE Single Device Configuration Usage Example: An Internet of Things Application", *Journal of International Scientific Publications* 2017, 11: 465-473.
- [12] Kim T, Kim EJ., "A Novel 3D Indoor Localization Scheme Using Virtual Access Point", *International Journal of Distributed Sensor Networks* 2014.
- [13] Bruno L, Adesso P, Restaino R., "Indoor Positioning in Wireless Local Area Networks with Online Path-Loss Parameter Estimation", *Scientific World Journal* 2014.
- [14] Liu JB, Chen RZ, Pei L, Guinness R, Kuusniemi H., "A Hybrid Smartphone Indoor Positioning Solution for Mobile LBS", *Sensors* 2012; 12: 17208-17233.

BIOGRAPHIES



Deniz TAŞKIN received the B.S., M.S. and Ph.D. degrees in computer engineering from the Trakya University.

From 2002 to 2007, he was a Research Assistant and since 2007 he become an Assistant Professor at Trakya University Computer Engineering Department. He is the author of book named "Gömülü Sistem Tasarımı". His research interests include embedded systems, personal area networks, micro controllers and computer architecture.

Scene Change Detection using Different Color Palettes and Performance Comparison

F. Bulut, and S. Osmani

Abstract— In the world of massive uploaded videos, to be able to cover the content of a video at a glance becomes a necessity since there is no enough time to watch the whole video for an individual. Looking at frames of different scenes in a video gives a brief idea of the content, when each different scene images are listed to be checked by the user. In this study, an approach using various color palettes is proposed to be able to detect the different scenes of a video. In the proposed method, color histogram values of sequential frames firstly are calculated. If the difference in the histogram values of the pair frames in sequence is over a threshold value (percentage of change), scene change is detected. In the experimental studies, 3-Bit RGB (Red Green Blue), 6-Bit RGB, 8-Bit RGB, 9-Bit RGB, 1-Bit Binary, 4-Bit Gray, and 8-Bit Gray palettes are implemented over a list of video files and compared. In the comparisons of palettes, accuracy, precision, recall, and F1-Score performance metrics are used. In the performance accuracy controls, 6-Bit RGB color pallet with a threshold level value of 35% has been experimented as the best of all.


Index Terms— Scene change detection, RGB and gray palettes, histogram.

I. INTRODUCTION

IN the recent world of technology, electronic devices and social media are able to store huge sized video files where it makes searching and finding the required videos harder and time consuming. In this case, understanding the content of a video just by looking at its name is not considered as a correct and efficient way. Also, the meta information of a video might be irrelevant with the real content of the video. However, tagging method has been initially released as a sole solution. But this method brings out two more critical issues. First, if the irrelevant tag names were given mistakenly or knowingly, then the whole search process would be negatively affected. Second, it can be more time consuming.

Previously researchers have concluded static and dynamic video summarizations under the same field while stationary image summarizations provided a small collection of photos achieved from video sources.

Dynamic video summarizations have constructed from relatively queued photos and original video's audio.

✉ F. BULUT, Istanbul Rumeli University, Computer Engineering Department, Istanbul, TURKEY, (e-mail: faruk.bulut@rumeli.edu.tr). 

S. OSMANI, Data Analyst, Netlinks Technology, Kabul, AFGHANISTAN, (e-mail: shaira@netlinks.ws). 

Manuscript received May 16, 2017; accepted August 11, 2017.
DOI: [10.17694/bajece.336217](https://doi.org/10.17694/bajece.336217)

These two summarization techniques are very different from each other, stationary image summarizations dealt only with images no need for audio, where dynamic image summarizations dealt with images along with audio which made it to worked very slowly.

As it is known video files are made from consecutive static images, named as frames. One second of a video file contains a certain amount of sequential frames, called as frame per second (FPS). The primitive TV broadcasting system releases 24 FPS [1] whereas this value is 30 FPS, in so many other video formats. In the HDTV it is 50 FPS. The value of FPS with interpolation techniques in HEVC (High Efficiency Video Coding) types of industries is rising up to 300 and with the resolution 8192x4320 pixels [2].

Scene change detection using histogram and color palettes is an answer to so many questions and challenges which are faced in world's many different sectors such as education sector, filming sector and most importantly security sector.

Internet offers free learning resources but its hectic to find the desired video tutorials in seconds. For finding the desired video the user is supposed to keep on searching and playing each and every video in order to get sure of its content not only this method is time consuming but sometimes it ends up without a positive result.

While scene change detection using histograms and color palettes allows users to find the desired video in lesser than a minute, as the user entered the required information the system gives as output the most important frames of the video, so the user can check the content and decide.

Also, scene change detection with histogram and color palettes brings an ease in security sector. As an example, let's suppose a 24-hour static camera in front of a grocery shop, in case if a thief enters, the camera records it. In a similar case finding out the true period of the theft is time consuming.

In contrast the other scene change detection techniques, here the proposed system allows the users to input their recorded file, provides the required information as an output the system and gives the most important frames. Therefore, the information about the incident can be found easily.

Meanwhile, by using scene change detection with histograms and color palettes algorithm many intelligent systems can be built. For example, an intelligent camera with static position, where if the camera changes its position by any outside factor it should be able to compare the initial position's information with the current and turn back to its initial position.

This paper contains four more sections. In the second one, there is a survey including the related studies. In the third section, the details of suggested method will be explained.

Before the conclusion section, there are some experimental results and performance comparisons of the proposed methods

II. RELATED STUDIES

Since video summarization is one of the big questions in this field, some previous researches have already proposed some methods. Some valuable methods are selected and listed chronologically below.

In 1996, Wolf released a solution for video summarization technique, identifying the main frame shots from the video [3]. It is preferred to use optical flow computations in order to identify local minimum of motion in a shot-stillness. This technique allows to discover both gestures and camera motions. Results of the effectively summarized shots have showed that this algorithm is successfully select many key frames from a single complex shot.

Defaux in 1996 explained an algorithm for summarization in which the image is identified in terms of the primitives of the scene [4]. In this technique representing of the video dataset in fewer bits, compression of files plays a great role. The proposed system utilizes a specific decoder to interpolate the frames in order to provide a reliable system.

Hong Zhang and his friends in 1997 released a solution for video summarization techniques as its system provided methods for temporal segmentation of video sequences into individual camera shots, using a novel twin comparison method [5]. This method was capable of detecting both camera shots implemented by sharp break and gradual transitions implemented by special editing techniques, including dissolve, wipe, fade-in and fade-out; and content based key frame selection of individual shots by examining their temporal variation of video contents and selecting a key frame after the differences of contents between the current frame and a preceding selected key frame exceeds a set of preselected thresholds.

Huang and his friends in 1999 released another solution in this filed. They proposed a new technique that aggregates motion information and intensity in order to discover scene changes in both sudden scene changes and gradual scene changes. Two major attributes are taken as the basic dissimilarity measures, and self Additionally, they propose a new intensity statistics model in order to find gradual scene changes. Their experimental studies proved that the proposed method had outperformed the previous approaches up to 1999.

The other researchers, Lee and his friends in 2003 explained that video summaries allow condensed representations of a video content through a combination of continuous images, graphical representations, video segments, and textual descriptors [7]. Their framework distinguishes between video summaries and video summarization techniques.

In 2014, in large video collections with clusters of categories, Daniela Potapov wrote an article using machine learning techniques. He explained that category-specific video summarization can produce more accurate video summaries than unsupervised learning methods that are blind to the video categories [7]. Their approach firstly performed a temporal segmentation into semantically-consistent segments providing a video from a known category. Then, equipped with a Support

Vector Machine classifier, this approach assigned some scores to each of the segments. The resulting video assembles the segment sequences with the bigger scores. Therefore, the gained short video summary is highly informative. Experimental studies over a list of video files proves that the technique gives relevant video summaries.

Zhang and his friend in 2015 released another technique as Multi-video summarization. In this research, the proposal is a new summarization method that implements preserves well-aesthetic frames and video stability. Particularly, a multi-task attribute selection is used in order to efficiently detect the semantically important attributes. Then, the key frames are selected based on their contributions in order to rebuild the video semantics. Then, a probabilistic model is suggested to fit the key frames dynamically into the video summary [9].

Lately in 2017, Wu and his friends has newly proposed a scene change detection method especially focused on between multi-temporal image scenes. In their research, a novel scene change detection method via Kernel Slow Feature Analysis (KSFA) is proposed. With the help of post-classification fusion, KSFA is used to extract the nonlinear temporally invariant attributes for better measure between corresponding multi-temporal image scenes. The post-classification fusion methods are based on Bayesian theory. They have experimented that the proposed method increases the accuracy of scene change detection, scene transition identification, and scene classification.

In this scene change detection field, different methods with their variations are proposed in the literature in the last decades. Most of the academic publications in this area stands on the empirical studies engineering field whereas few of the studies include novel approaches.

III. PROPOSED METHOD

Experimental study is performed on a list of selected videos. Collected video files which have different types and specifications are listed in Table 1. In the list, there are four video files whose attributes are as resolution, type, color type, aspect ratio (ration in dimensions), FPS (Frame Per Second), number of total frames, number of total different scene, duration in seconds, and lastly the source which comes from. As it is seen, these collected videos which have discrete features crate a rich experimental area where different types of pallets can be compared. Each video file has different frame per second rate.

In the RGB true color system, the capacity of each of color is 8 bits. The combination of the colors represents the picture

Additionally, in Table 1, the total number of different scenes in each video can be seen at the last column. The list has been prepared by a human in order to check the performance of the implemented methods in the experiments.

All the experiments are performed in the MATLAB environment [11] on MACOS operating system. The process firstly starts step by step with the decomposition of the frames in each video files.

The original resolutions, color system, and the FPS rates of the video files in the test list are bigger than normal for a digital image video processing operation.

TABLE I
FEATURES OF VIDEO FILES

Video ID	Resolution	Category	Color Type	Aspect Ratio	FPS	Duration	# of total frames	# of total different scene
1	640×480	VGA	24-bits RGB	4:3	24	32 sec.	24×30=720	5
2	1280×720	HD Ready	24-bits RGB	16:9	25	60 sec.	25×60=1508	9
3	1920×1080	Full HD	24-bits RGB	16:9	30	125 sec.	30×120=3602	17
4	3840×2160	4K	24-bits RGB	16:9	50	58 sec.	50×50=2500	11
Total					275 sec.	8330		

Those given numerical values in the list increase both the time complexity and the computational complexity. Hence, both the size of the videos and the color bits should be decreased for a fast execution. In the empirical studies, some quantization techniques are implemented. As it is known, quantization can be called as summarization of videos.

In Table 2, there are 7 different color palettes used for quantization techniques. As it is known, color palettes are the range of colors used in a visual medium. Also, a quantization (summarization) technique is done in bit values of the RGB color values [12]. For example, 8-bit value of a color in RGB

transforms into 2-bit value by deleting the rest of first 2 bits. In 8 bit colors, the coming numbers after the initial numbers are the details and tones of the specific color. The most important color codes are accepted as the initial bits in image processing.

The resolutions of the videos and the FPS rates have remained the same throughout the process. It is certain that to reduce those values will also decrease the computational time. Since this study focuses on the color palettes, these things have not changed in the experiments. Probably in further studies, these variations can be tested.

TABLE II
COLOR PALETTES FOR QUANTIZATION TECHNIQUES

Videos ID	Palette name	R	G	B	Gray	Color Bits	Color Status	Order Status
1	3-bit RGB	1	1	1	-	$2^3 = 8$	colored	order
2	6-bit RGB	2	2	2	-	$2^6 = 64$	colored	order
3	8-bit RGB	3	3	2	-	$2^8 = 256$	colored	Not-order
4	9-bit RGB	3	3	3	-	$2^9 = 512$	colored	order
5	1-Bit Binary	-	-	-	1	$2^1 = 2$	black-white	order
6	4-Bit Gray	-	-	-	4	$2^4 = 16$	gray	order
7	8-bit Gray	-	-	-	8	$2^8 = 256$	gray	order

RGB stands for red-green-blue on a computer display. These three basic colors can be combined in various proportions in order to obtain any color in the visible spectrum for a human. In the combination, each levels of red, green and blue can vary from 0 to 100 percent of full intensity. If the total bit capacity is 24 of the RGB type, each level is represented by the range of decimal numbers from 0 to 255 since $2^8 = 256$.

A histogram is a specific statistical information that displays the frequency of color bits in successive numerical intervals of

equal size. In common forms of histogram, the dependent variable is shown along the vertical axis and the independent variable is shown along the horizontal axis.

The proposed system captures each frame when processing on a selected video file. In each frame, the color histogram values for Red, Green and Blue are calculated. As an example, red, green, blue and RGB histogram values can be seen using the Lena picture in Fig. 1, Fig. 2, Fig. 3, and Fig. 4 sequentially.

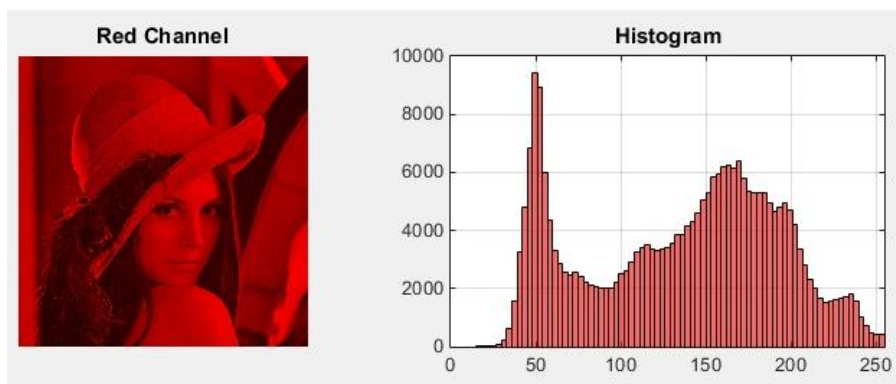


Fig. 1. Red color histogram

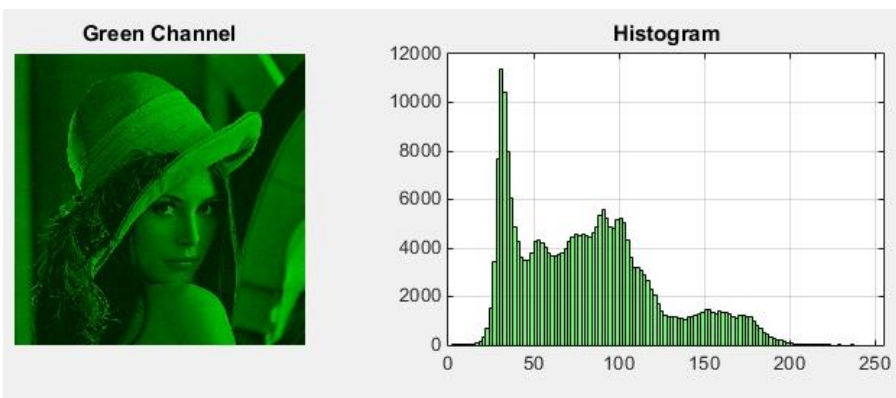


Fig. 2. Green color histogram

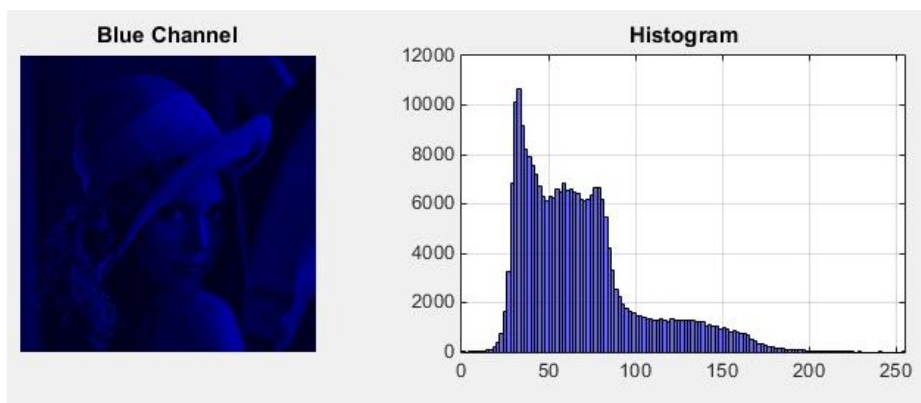


Fig. 3. Blue color histogram

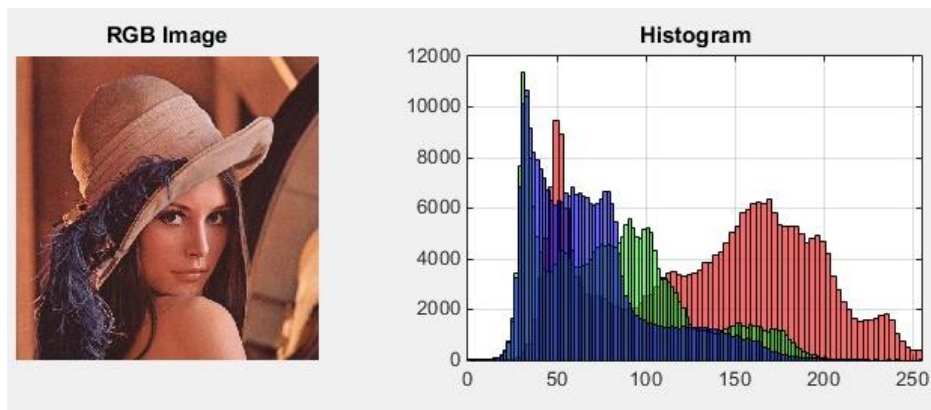


Fig. 4. Red Green and Blue color histograms

Those histogram values of the colors are different from each other. But in this example this values are taken from a static picture, Lena [13]. In video processing, these calculations are done for each frame. It should be emphasized that the histogram values continuously change in each frame during the video.

Basically the algorithm focuses on the changes of color histogram values on sequential frames. While the system generates histogram chart for each captured frame, the changes should be checked in a sequential pair of frames in order to detect the scene changes. For example, in a pair of frames, if there is a small change in the Blue histogram, it might be that a small blue colored ball has newly entered the current scene. If there is big change in the histogram rates, that means the previous scene has changed.

How can be the “small” and the “big” changes defined in the histogram values? The answer of the question affects the accuracy and the performance of the proposed system. The answer is the threshold value that compares the differences of histogram frequencies between each continuous frame. If the total histogram change is bigger than the specified threshold value, it means a new scene occurs. If not, it is the same repeating scene.

IV. EXPERIMENTAL RESULTS AND PERFORMANCE COMPARISON

In order to evaluate the accuracy, the system should use some basic performance metrics such as True Positive (TP), True Negative (TN), False Positive (FP) and False Negative (FN). These basic metrics are the basis of other well-known criterions such as accuracy, precision, recall, and confusion matrix table [14].

The proposed software mechanism sometimes detects the real scene change. This is called as TP detection. Sometimes the system detects a scene change when actually it is not. This is called as FP. If the system cannot detect the scene change, it is called as FN. And lastly if the system detects any change when there is no change, it is called as TN. TN value in this application cannot be realized. Because of this, TN will always be 0 throughout the experiments. These performance criterions of TP, TN, FP, and FN here are newly adapted to this study.

The TP, TN, FP and FN values are manually calculated by watching the whole videos in the list. The TP, TN, FP and FN rates are as shown in Table 3.

TABLE III
TP, TN, FP AND FN VALUES OF PALLESTS OVER VIDEOS

	Video 1				Video 2				Video 3				Video 4			
	TP	TN	FP	FN	TP	TN	FP	FN	TP	TN	FP	FN	TP	TN	FP	FN
3-Bit RGB	2	-	4	3	5	-	5	4	10	-	14	7	5	-	4	6
6-Bit RGB	3	-	2	2	7	-	4	2	15	-	9	2	9	-	3	2
8-Bit RGB	5	-	1	0	8	-	1	0	17	-	2	0	11	-	1	0
9-Bit RGB	5	-	1	0	8	-	2	0	17	-	1	0	11	-	0	0
1-Bit Binary	2	-	3	3	4	-	5	6	5	-	11	12	6	-	4	5
4-Bit Gray	3	-	3	2	5	-	4	6	10	-	9	7	8	-	3	3
8-Bit Gray	3	-	4	2	5	-	4	5	11	-	8	6	9	-	3	2

In the experiments, different threshold levels such as 10%, 20%, 30%, 35%, 40%, and 50% have been tested for better performance. 35% level has been experimented as the best of all.

The other performance criterions are accuracy, precision, recall, F1-Score, and recall are as follows.

Accuracy (Acc), more commonly, is a description of systematic errors, a measure of statistical bias. The accuracy formula is in the Eq. (1).

$$Accuracy = \frac{Correct\ predictions}{Total\ number\ of\ data} = \frac{TP + TN}{TP + TN + FP + FN} \quad (1)$$

Precision, also called as positive predictive value, is the fraction of retrieved instances that are relevant. Precision can be calculated using the formula in the Eq. (2).

$$Precision = \frac{True\ predicted}{Number\ of\ predictions} = \frac{TP}{TP + FP} \quad (2)$$

Recall, also known as sensitivity, is the fraction of relevant instances that are retrieved. Recall formula can be seen in the Eq. (3).

$$Recall = \frac{Predicted\ value}{Real\ value} = \frac{TP}{TP + FN} \quad (3)$$

F1 Score is the harmonic mean of precision and recall both. F1 gives more accurate results than precision or recall because it contains these metrics. F1-Score formula is in the Eq. (4).

$$F1\ Score = \frac{2}{\frac{1}{P} + \frac{1}{R}} = 2 \times \frac{P \times R}{P + R} \quad (4)$$

TABLE IV
ACCURACY, PRECISION, RECALL AND F1 VALUES OVER FOUR VIDEOS

	Video 1				Video 2				Video 3				Video 4			
	Acc	P	R	F1	Acc	P	R	F1	Acc	P	R	F1	Acc	P	R	F1
3-Bit RGB	0.22	0.33	0.40	0.36	0.36	0.50	0.56	0.53	0.32	0.42	0.59	0.49	0.33	0.56	0.45	0.50
6-Bit RGB	0.43	0.60	0.60	0.60	0.54	0.64	0.78	0.70	0.58	0.63	0.88	0.73	0.64	0.75	0.82	0.78
8-Bit RGB	0.83	0.83	1.00	0.91	0.89	0.89	1.00	0.94	0.89	0.89	1.00	0.94	0.92	0.92	1.00	0.96
9-Bit RGB	0.83	0.83	1.00	0.91	0.80	0.80	1.00	0.89	0.94	0.94	1.00	0.97	1.00	1.00	1.00	1.00
1-Bit Binary	0.25	0.40	0.40	0.40	0.27	0.44	0.40	0.42	0.18	0.31	0.29	0.30	0.40	0.60	0.55	0.57
4-Bit Gray	0.38	0.50	0.60	0.55	0.33	0.56	0.45	0.50	0.38	0.53	0.59	0.56	0.57	0.73	0.73	0.73
8-Bit Gray	0.33	0.43	0.60	0.50	0.36	0.56	0.50	0.53	0.44	0.58	0.65	0.61	0.64	0.75	0.82	0.78

In Table 4, Accuracy and F1 scores are calculated and the results are listed using the corresponding formulas over each video file.

Accuracy and F1 score rates are illustrated in bar charts in Figure 5 and Figure 6 respectively. In both Accuracy and F1 metrics, the performance of each color pallets can be examined at a glance. 8-Bit RGB and 9-Bit RGB color pallets outperform when compared with the others.

1-Bit Binary image is the worst one, of all. The main reason of the failure is the loss of image details. As it is known, the binary image contains just black and white information. There is not any other color. Hence, the details are disappeared in the quantization phase.

The similar situation to the 1-Bit Binary image exists in the gray color pallets. The unsuccessful performance of 4-Bit and 8-Bit gray level pallets can be seen in Figure 5 and Figure 6. According the experimental results increasing the bit number of a gray colored pallet will not rise the accuracy level. Thus, it can be inferred that red, green and blue color values are very important in the scene change detection.

When compared all the color pallets, the 8-Bit and 9-Bit RGB methods give the best performance in detection of scenes. Maybe 8-Bit method can be preferred to 9-Bit one because of less computational and space complexity.

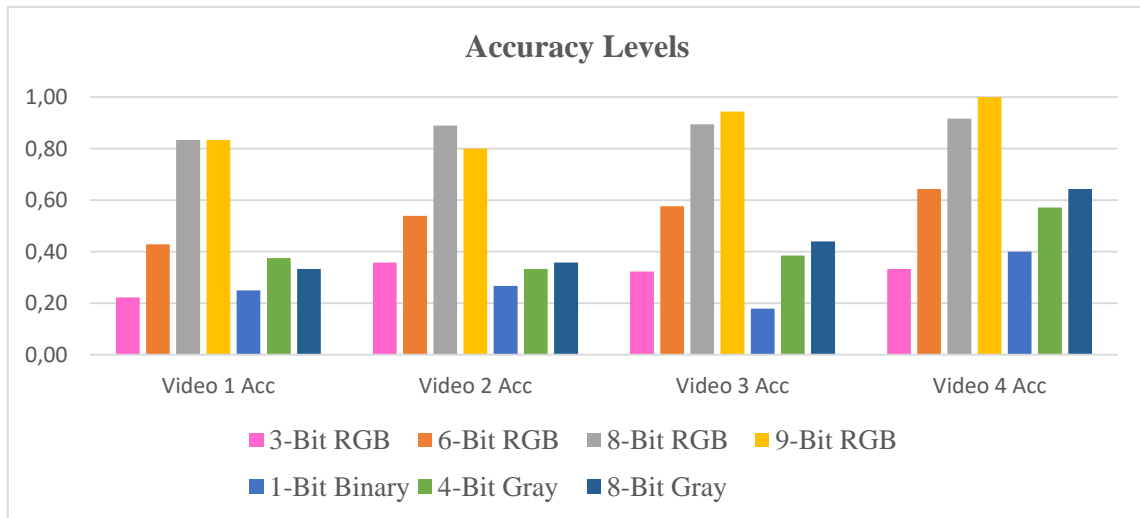


Fig. 5. Accuracy values over videos.

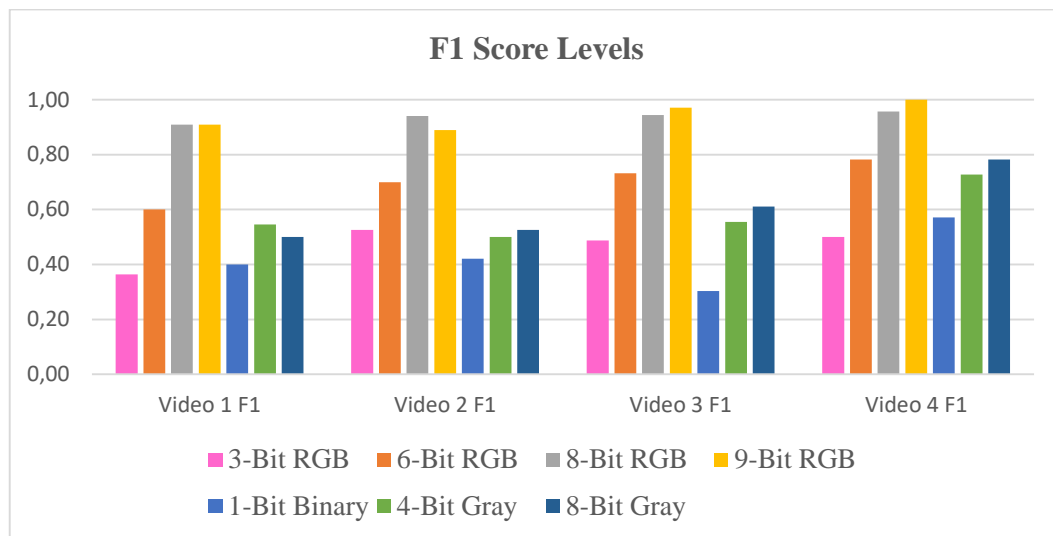


Fig. 6. F1-Score values over videos.

V. CONCLUSIONS

In this project we aim to develop a system which will summarize and give content of any lengthy video. This system will provide so many efficiencies for the user its aimed to improve the performance of searching the content of any video with less time consumptions. This proposed mechanism is composed of some techniques in order to do the summarization and give the content as the system uses color reduction, color pallets slow motion detection and the histogram charts. Proposed model of summarization can be concluded as the fact that best scene change detection can be performed using 8-RGB color pallet. The current concern is about saved static videos but in further studies this concern might be to develop a real time system which summarizes online social media videos. Summarization has been an important issue in world of image processing so the research field has been worldwide and many solutions has been implemented.

REFERENCES

- [1] Nakamura, J. (Ed.). (2016). Image sensors and signal processing for digital still cameras. CRC press.
- [2] Rao, K. R. (2016, September). High efficiency video coding. In Signal Processing: Algorithms, Architectures, Arrangements, and Applications (SPA), 2016 (pp. 11-11). IEEE.
- [3] Wolf, W., (1996), "Key Frame Selection by Motion Analysis", Proceeding of IEEE International, Conference on Acoustics, Speech and Signal Processing, Atlanta, GA, 1228-1231
- [4] Dufaux, Frédéric, and Fabrice Moscheni. "Segmentation-based motion estimation for second generation video coding techniques." Video Coding. Springer US, 1996. 219-263.
- [5] Zhang, Hong J., Jian H. Wu, and Stephen W. Smoliar. (1997), "System for automatic video segmentation and key frame extraction for video sequences having both sharp and gradual transitions." U.S. Patent No. 5,635,982. 3 Jun. 1997.
- [6] Huang, C. L., & Liao, B. Y. (2001). A robust scene-change detection method for video segmentation. IEEE Transactions on Circuits and Systems for Video Technology, 11(12), 1281-1288.
- [7] Lee, J., Lee, G. v. Kim, W., (2003), "Automatic video summarizing tool using MPEG-7 descriptors for personal video recorder", IEEE Trans. on Cons. Elect, Vol 49, 49-742
- [8] Danila Potapov, Matthijs Douze, Zaid Harchaoui, Cordelia Schmid. Category-specific video summarization. ECCV 2014 - European

Conference on Computer Vision, Sep 2014, Zurich, Switzerland, Springer, 2014

- [9] Zhang, L., Xia, Y., Mao, K., Ma, H., & Shan, Z. (2015). An effective video summarization framework toward handheld devices. Industrial Electronics, IEEE Transactions on, 62(2), 1309-1316.
- [10] Wu, C., Zhang, L., & Du, B. (2017). Kernel slow feature analysis for scene change detection. IEEE Transactions on Geoscience and Remote Sensing, 55(4), 2367-2384.
- [11] Marques, Oge. Practical image and video processing using MATLAB. John Wiley & Sons, 2011.
- [12] Umbaugh, Scott E. Digital image processing and analysis: human and computer vision applications with CVPITools. CRC press, 2016.
- [13] Lena Söderbergt, Image Processing Benchmark image, 1973. URL: [tps://en.wikipedia.org/wiki/Lenna](https://en.wikipedia.org/wiki/Lenna), taken date: 06/02/2017.
- [14] Mousavizadegan, M., & Mohabatkar, H. (2016). An Evaluation on Different Machine Learning Algorithms for Classification and Prediction of Antifungal Peptides. Medicinal Chemistry, 12(8), 795-800

BIOGRAPHIES



Faruk BULUT was born in Kayseri, Turkey in 1974. He got his bachelors' degree in the Computer Education Department at Marmara University in 1998, master degree in the Computer Engineering Department at Istanbul in 2010, and PhD degree in the Computer Engineering Department at Yildiz Technical University in 2015. He has been a lecturer in the İzmir Kâtip Çelebi University during the years of 2015-2016. Now he is an academician in Istanbul Rumeli University. His major areas of interests are: Image Processing, Machine Learning, Meta Learning and Ensemble Methods.



Shaira OSMANI was born in Kabul Afghanistan in 1994. She received her bachelor's degree from computer engineering department of İzmir Kâtip Çelebi University, in 2016. She has won the gold medal with the project related with this research article in the competition of the Young Brain New Ideas (Genç Beyinler Yeni Fikirler, GBYF). The 5th GBYF Graduation Projects has been organized in the Dokuz Eylül University Tinaztepe campus with the participation of total 11 Aegean Region Universities. Now she is a computer engineer and data analyst in Afghanistan.

An Object Detection and Identification System for a Mobile Robot Control

M. Aydın, and G. Erdemir

Abstract— The one of the features of mobile robot control is to detect and to identify objects in workspace. Especially, autonomous systems must detect obstacles and then revise actual trajectories according to new conditions. Hence, many solutions and approaches can be found in literature. Different sensors and cameras are used to solve problem by many researchers. Different type sensors usage can affect not only system performance but also operational cost. In this study, single camera based obstacle detection and identification algorithm was developed to control omni-drive mobile robot systems. Objects and obstacles, which are in robot view, are detected and identified their coordinates by using developed algorithms dynamically. Developed algorithm was tested on Festo Robotino mobile robot. Proposed approach offers not only cost efficiency but also short process time.


Index Terms—Mobile robot control, object detection, robotino.

I. INTRODUCTION

TODAY, different kinds of mobile robots are used in many application areas such as defense systems, coastal safety, environmental control systems, search and rescue systems, space studies, industry applications, ocean research, service robotics, and etc[1]. They will have a common usage area and be a part of our daily life after Industry 4.0 revolution. In recent years, the studies in service robotics have become very popular [2]. Service robots can be examined in three subsystems which are mobile robotic base, manipulator and sensor systems [1-3]. Sensing and identifying objects in dynamic environment are very important to develop control algorithms for service robots. On this topic, there are many researches in the literature [1-14]. There are many studies and researches in the literature on this topic [1-14]. Besides, manufacturers keep focusing on to develop low-cost solutions.

Different types of sensors are used for obstacle detection [1-14]. Especially, LiDAR (Light Detection and Ranging) is used extensively in both indoor and outdoor applications [7]. And, it is the most suitable sensor for indoor and outdoor applications. solutions to decrease the cost for cost-effective applications. Another common method for object detection and identification

M. AYDIN, is with Department of Computer Engineering, Fatih Sultan Mehmet Vakif University, Istanbul, Turkey, (e-mail: maydin@fsm.edu.tr). 

✉ **G. ERDEMİR**, is with Department of Electrical and Electronics Engineering, Istanbul Sabahattin Zaim University, Istanbul, Turkey, (e-mail: gokhan.erdemir@izu.edu.tr). 

Manuscript received April 06, 2017; accepted July 09, 2017.
DOI: [10.17694/bajece.336480](https://doi.org/10.17694/bajece.336480)

However, using LiDAR in mobile robots increases the cost considerably. Manufacturers must find and develop new image processing. In this kind of systems, images captured from one or more cameras are processed by a computer (or microprocessor-based controller) which is located inside or outside of the mobile robot [1]. Various operations are performed on processed images to detect objects and according to results robot trajectory is re-determined and calculated by controller [7-14]. In general, this technique which uses a single camera provides significant cost advantages. However, it is difficult to process streaming images from camera by using low capacity microprocessors [10]. In this study, an object detection and identification algorithm is developed using a low-cost camera to re-determine and planning of mobile robot trajectory. The developed algorithm is tested on the simulation software of Festo Robotino mobile robot and the results are examined. The paper is organized as follows. In section II, brief information is presented for Festo Robotino Mobile Robot (Robotino). In section 3, the structure of the developed object detection and identification system 2 is presented. The case studies and results are presented in section 4. In the last section, the obtained experimental results are discussed.

II. FESTO ROBOTINO MOBILE ROBOT

Robotino is an omni-drive mobile robot platform which is produced by Festo [15-16]. It is shown in Fig. 1. Technical properties of the Robotino are listed in Table 1. The embedded micro-controller of Robotino has ROS (Robotic Operating System) and controls wireless communication, sensors, speed mode [15-16]. By using the encoder which is inside of 1.72AP version embedded software, x-y position and z-orientation can be easily obtained. Using the IEEE 802.11g standard, x-y coordinates and angular velocity information can be easily transmitted to Robotino [15-16].



Fig. 1. Festo Robotino mobile robot platform

TABLE 1
TECHNICAL PROPERTIES OF THE ROBOTINO

Properties	Description
Dimesions	Radius: 370mm, height: 210mm, weight: 11 kg, payload capacity: 5 kg
Sensors	9 x Sharp GD2D120 infrared distance sensor, 1 x analog inductive sensor, sensor integrated bumper, 2 x optical sensors, USB web cam
Embedded Controller	PC104 MOPSIcdVE processor (300MHz, SDRAM 64MB, 128MB Compact external memory), C++ library, .Net and Matlab support, wireless LAN, ethernet, 2 x USB, 2 x RS-232
I/O	3 x output port for omni-drive, 10 x analog input (0–10V, 50 Hz), 2 x analog output, 16 x digital I/O, 3 x relay

RobotinoSim and RobotinoView software which are developed by Festo offer simulation environment for Robotino. Algorithms, which are validated in the simulation environment, can be integrated into the real system. And also, developers can develop their own simulation tool and/or control software by using Matlab, Visual Studio, Java or C/C++. Robotino support these programming platforms. In order to execute the commands on the robot, the connection between the robot and the computer must be activated firstly. For this, the following pseudo-code command lines which is shown in below must be run on Matlab and Visual Studio platforms to load and initialize the robot-computer and computer-robot data communication protocol [17]. “*robotinoAPI*” and “*robotinoIP*” parameters can be various from Robotino versions [17]. Detailed information about Robotino can be found in [15-17].

```

bool InitalizeRobotConnection()
{
    bool connection = false;
    bool l = LoadRobotLibrary();
    if (l == true)
    {
        describeRobotPath();
        loadlibrary( 'robotinoAPI');
        describeRobotParameters();
        CID = SetCommunicationID();
    }
    CID.setAddress(CID, 'robotinoIP');
    if (Connect2Robot(CID)) return true;
    else return false;
}
    
```

III. OBJECT DETECTION

Object detection algorithm which is consist of six steps was developed by using Matlab. The flow chart of developed algorithm is shown in Fig.2. In first step, images which is captured from video stream by camera are classified and labeled by colors. In the labeling process, each object is expressed as a matrix consisting of three main colors as shown in equation (1).

$$O_n = [R_n \quad G_n \quad B_n] \tag{1}$$

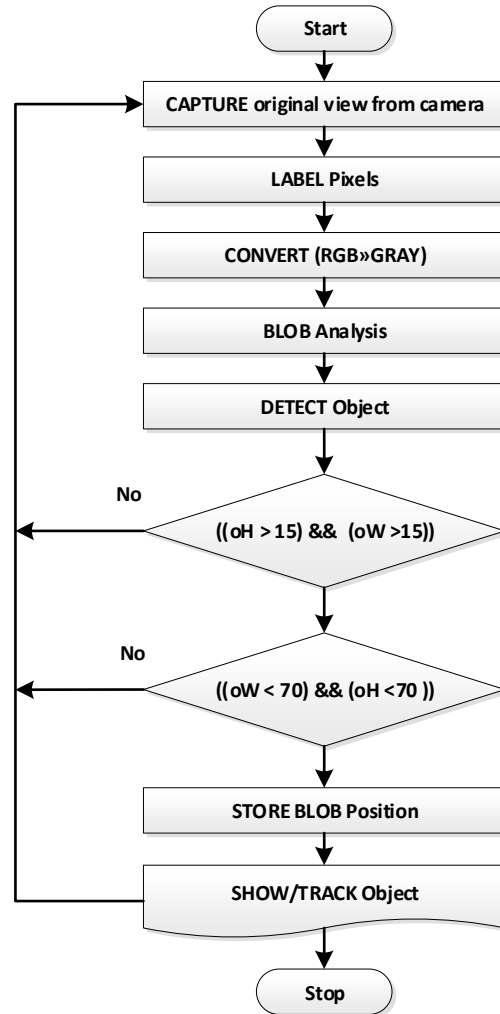


Fig. 2. Flow chart of object detection

In (1), R_n is 80x80 red color matrix, G_n is 80x80 green color matrix and B_n is 80x80 blue color matrices, respectively. In the next step, the colors of the objects with 16 essential colors in the RobotinoSim tool are defined according to the RGB codes to be used in the BLOB analysis [18]. RGB → GRAY color conversion is performed on the detected image before this operation. And then, BLOB analysis is performed on labeled sections [18]. The BLOB analysis provides the coordinates, width and height information of the objects in the live video stream which is separated by sections at first step. The detected objects on the live video stream are marked by using "Bounding Box" method. This method produces B matrix which is shown in equation (2).

$$B_n = \begin{bmatrix} x_1 & y_1 & w_1 & h_1 \\ x_2 & y_2 & w_2 & h_2 \end{bmatrix} \tag{2}$$

In (2), where B_n represents an object in bounding box, n is the number of detected objects. x_1, x_2, y_1 and y_2 represent coordinates of the objects on live video stream. h_1, h_2, w_1 and w_2 represent height and weight of the object. The matrix which is

shown in equation 3 is obtained from the BLOB analysis.

$$BO_n = [0 \quad B_n] \tag{3}$$

BO_n is a 4xn matrix where n is the number of detected objects. In this way, coordinates, height and width information of detected objects are obtained. If the dimensions of the objects are in limits which are between 15 and 70 pixels for this study, O_n matrix which is shown in (1) is obtained for each object. On matrix is necessary to classify each object by color.

In the next section, results of experimental studies which are performed in simulation are presented.

IV. CASE STUDIES

Test environment is created by using RobotinoSim simulation tool [17] for testing proposed algorithm. The codes which is written in Matlab are compiled on RobotinoSim. Views of the object detection experiments are shown in Fig.3-7. For each experiment, robot - computer connection is set and tested at the beginning.

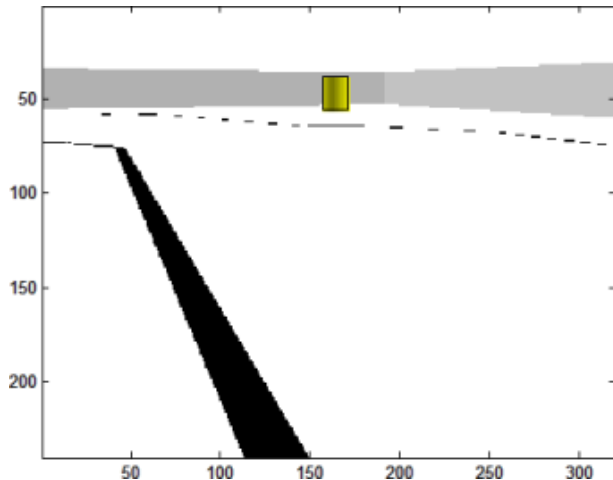


Fig. 3. Detection of yellow object from far position.

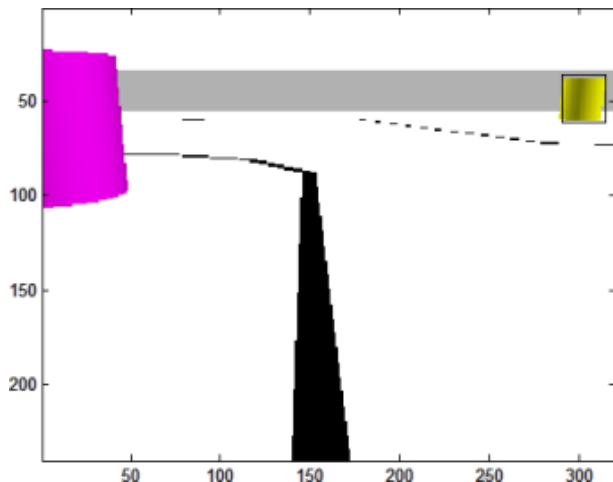


Fig. 4. Detection of yellow object from near position.

In Robotino Sim, basic 16 colors are used to create objects. Basic colors are preferred because of using any color filters for filtering color tones. Different shapes have been created as objects such as cylinder, cube, rectangular parallelepiped etc. It is assumed that the test setup is in constant light intensity. Figures 3-7 show detection of different objects. Figure 3 shows the process of detecting a yellow cylindrical object in the range of 15-70 pixels width and 15-70 pixels height in live video stream.

Fig.4 shows the process of detecting a yellow cylindrical object when robot is approaching to the object. The choice of the range of 15-70 pixels is to limit the reasons for objects to a certain size. In this view, changes over and under a certain size are automatically filtered. These dimensions can be changed if desired.

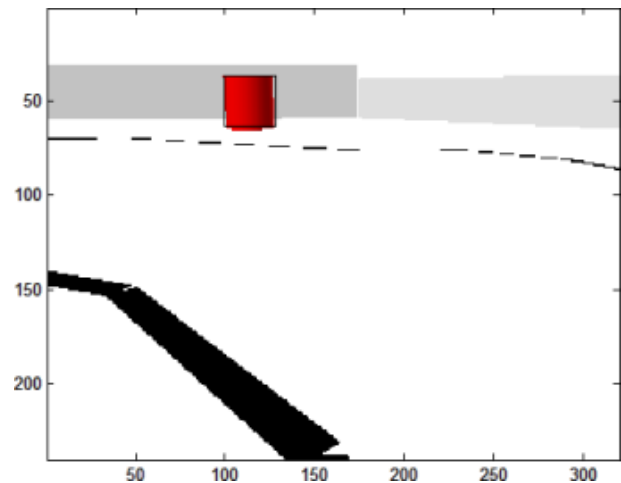


Fig. 5. Detection of red object from far position.

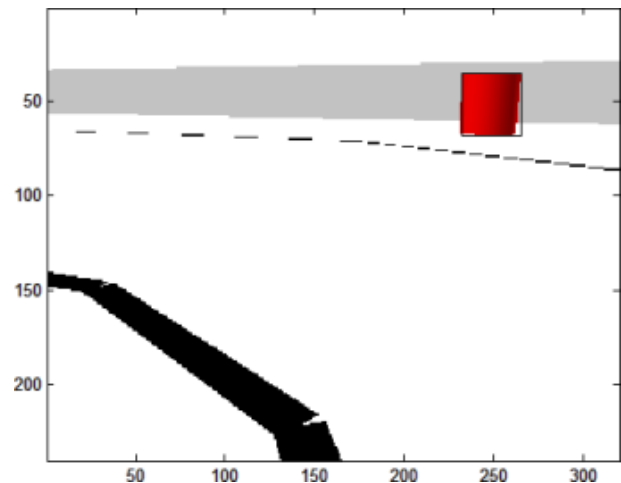


Fig. 6. Detection of red object from near position.

Fig.5 shows the process of detecting a rectangular prismatic object with a width size of 15-70 pixels and a height size of 15-70 pixels in real time. Fig.6 shows the detection of a red square prismatic object when robot is approaching to the object.

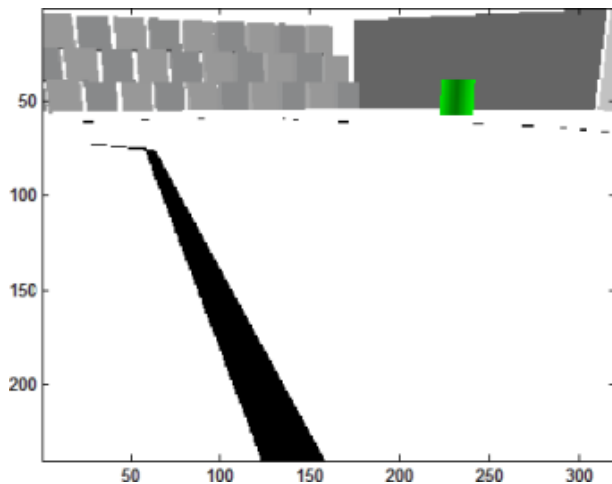


Fig. 7. Detection of green object.

Fig. 7 shows the process of detecting the green cylindrical object in the range of 15-70 pixels width and 15-70 pixels height during live video stream in the real-time.

V. CONCLUSION

In this study, detection and identification of objects in the real environment, which is one of the most important topics in mobile robot control, have been performed. By using the developed algorithm, images which are obtained from a low-cost single camera are captured and the objects which have different colors and shapes in the work space of the robot are detected and identified. The main aim of the proposed approach is to detect any kind of objects which are in work space of robot by using only low-cost single camera without an extra equipment. According to experimental results, proposed approach provides detection of all objects which are fit in determined dimension range in robot work space. And, all detected objects are labeled and marked on live video stream. By using these steps, robot can easily calculate coordinate of each object. Performance of the proposed approach is observed during experimental studies. According to our observation results, proposed approach is performed with high success rate and low calculation time. As a future work, classification of detected objects will be done by artificial neural network for developing autonomous behavior.

REFERENCES

- [1] G.N. DeSouza, A.C. Kak, "Vision for Mobile Robot Navigation: A Survey", *IEEE Transaction on Pattern Analysis and Machine Intelligence*, Vol. 24, No. 2, pp. 237-267, 2002.
- [2] A. Kroll, S.Soldan, "Survey Results on Status, Needs and Perspectives for using Mobile Service Robots in Industrial Applications", 11th International Conference on Control, Automation, Robotics and Vision, pp. 621-626, December 7-10, 2010, Singapore.
- [3] H. Takai, M. Miyake, K. Okuda, K. Tachibana, "A Simple Obstacle Arrangement Detection Algorithm for Indoor Mobile Robots", *2nd International Asia Conference on Informatics in Control, Automation and Robotics*, pp.110 – 113, Mar 6 - 7, 2010, Wuhan, China.
- [4] J. Zhu, Y. Wang, H. Yu, Haixia Xu, Y. Shi, "Obstacle Detection and Recognition in Natural Terrain for Field Mobile Robot Navigation", *the 8th World Congress on Intelligent Control and Automation*, pp. 6567 – 6572, July 6-9 2010, Jinan, China.
- [5] T. Gandhi, M.T. Yang, R. Kasturi, O. I. Camps, L. D. Coraor, J. McCandless, "Performance Characterization of the Dynamic

- Programming Obstacle Detection Algorithm", *IEEE Transactions on Image Processing*, Vol. 15, No. 5, pp.1202-1214, MAY 2006,
- [6] N. Morales, J.T. Toledo, L. Acosta, R. Arnav, "Real-Time Adaptive Obstacle Detection Based on Image Database", *Computer Vision and Image Understanding*, Vol. 115, pp. 1273-1287, 2011.
- [7] A.S. Karakaya, G. Küçüküydüz, H. Ocak, Z. Bingül, "Mobil Robot Platformu Üzerinde Engel Algılanması ve Optimal Yönün Belirlenmesi", *20th Signal Processing and Communications Applications Conference (SIU)*, pp. 1-4, April 18-20, 2012, Mugla, Turkey.
- [8] A.Talukder, R. Manduchi, A. Rankin, L. Matthies, "Fast and Reliable Obstacle Detection and Segmentation for Cross-country Navigation", *IEEE Intelligent Vehicle Symposium*, Vol.2, pp. 610-618, June 17-21, 2002, Versailles, France.
- [9] U. A. Khan, A. Fasih, K. Kyamakya, J. C. Chedjou, "Genetic Algorithm Based Template Optimization for a Vision System: Obstacle Detection", *XV International Symposium on Theoretical Engineering (ISTET)*, pp. 164-168, June 22-24, 2009, Lübeck, Germany.
- [10] L. Liu, J. Cuib, J. Li "Obstacle Detection and Classification in Dynamical Background", *AASRI Conference on Computational Intelligence and Bioinformatics*, pp. 435 – 440, July 1-2, 2012, Changsha, China.
- [11] Z. Yankun, H. Chuyang, W., Norman, "A Single Camera Based Rear Obstacle Detection System", *IEEE Intelligent Vehicles Symposium (IV)*, pp.485-490, June 5-9, 2011, Baden-Baden, Germany.
- [12] A.R. Derhgawen, D. Ghose, "Vision Based Obstacle Detection using 3D HSV Histograms", *Annual IEEE India Conference (INDICON)*, pp.1-4, December 16-18, 2011, Hyderabad, India.
- [13] Y.C. Lin, C.T. Lin, W.C. Liu, L.T. Chen, "A Vision-Based Obstacle Detection System for Parking Assistance", *8th IEEE Conference on Industrial Electronics and Applications (ICIEA)*, pp. 1627 – 1630, June 19-21, 2013, Melbourne, Australia.
- [14] S. Das, I. Banerjee, T. Samanta, "Sensor Localization and Obstacle Boundary Detection Algorithm in WSN", *Third International Conference on Advances in Computing and Communications*, pp. 412 – 415, August 29-31, 2013, Kochi, Kerala, India.
- [15] S. E. Oltean, M. Dulau and R. Puskas, "Position Control of Robotino Mobile Robot Using Fuzzy Logic", *IEEE Int. Conf. on Automation Quality and Testing Robotics (AQTR)*, Cluj-Napoca, Romania, May 28 – 30, 2010.
- [16] Festo Robotino Manual, 2010.
- [17] <http://www.openrobotino.org/> (Erişim Tarihi Ocak 2014).
- [18] T. Lindeberg, "Detecting Salient Blob-Like Image Structures and Their Scales with a Scale-Space Primal Sketch: A Method for Focus-of-Attention", *International Journal of Computer Vision* Vol.11, No. 3., pp 283–318, 1993.

BIOGRAPHIES



Musa AYDIN received his B.S. and M.S. degrees from Marmara University, Turkey. He is currently pursuing his Ph.D in the Department of Computer Engineering at Marmara University. And also he is working at the Department of Computer Engineering at Fatih Sultan Mehmet Vakif University as an instructor. His research interests include robotics, UAVs and embedded systems.



Gokhan ERDEMİR, received his B.Sc., M.Sc. and Ph.D. degrees from Marmara University, Turkey, respectively. During his Ph.D., he worked as a research scholar at Michigan State University, Department of Electrical and Computer in East Lansing MI, USA. Now, he is an assistant professor at Istanbul Sabahattin Zaim University, Department of Electrical and Electronics Engineering. His research topics include robotics, mobile robotics, control systems, and intelligent algorithms.

Generation of Bifurcation Diagrams for Ferroresonance Characterization Using Parallel Computing

J. A. Corea-Araujo, G. Guerra, J. A. Martínez-Velasco, and F. González-Molina


Abstract— Ferroresonance is a complex phenomenon that involves the association of nonlinear magnetizing inductances and capacitances. This nonlinear phenomenon can be initiated in many different ways, which makes its characterization very difficult. Some recent works have shown how bifurcation diagrams can be advantageously used for predicting the phenomenon at its different stages and finding safety zones for parameter selection. The present work expands the scope of some tools originally developed for assessing ferroresonance behavior by means of 3D bifurcation diagrams. The main goal of this work is to propose the application of parallel computing to speed up the generation of bifurcation diagrams.


Index Terms—Bifurcation Diagram, EMTP, Ferroresonance, MATLAB, Modeling, Non-linear dynamics, Parallel computing, Parametric study.


I. INTRODUCTION


FERRORESONANCE normally refers to a series resonance that typically involves the interaction of a saturable transformer and a capacitive distribution cable or transmission line [1]. Due to the involved nonlinearities and the various situations that can lead to ferroresonance, it is difficult to predict whether it will occur or not, and the severity with which it can occur [1]. Traditionally, the analysis of ferroresonance has been difficult due to its unpredictability and the lack of an overall understanding.

A roadmap for ferroresonance analysis, going from a system modeling to a ferroresonance behavior analysis and prediction using bifurcation diagrams was presented in [2].

J. A. COREA-ARAUJO, is with the Dept. d'Enginyeria Elèctrica, Universitat Politècnica de Catalunya, Diagonal 647, 08028 Barcelona, Spain. (e-mail: javier.arturo.corea@upc.edu) 

G. GUERRA, is with the Dept. d'Enginyeria Elèctrica, Universitat Politècnica de Catalunya, Diagonal 647, 08028 Barcelona, Spain. (e-mail: gerardo.guerra@upc.edu) 

J. A. MARTINEZ-VELASCO, is with the Dept. d'Enginyeria Elèctrica, Universitat Politècnica de Catalunya, Diagonal 647, 08028 Barcelona, Spain. (e-mail: martinez@ee.upc.edu) 

F. GONZALEZ-MOLINA, Francisco González-Molina is with the Dept. d'Enginyeria. Electrònica, Elèctrica i Automàtica, Universitat Rovira i Virgili, Av. Països Catalans 26, 43007 Tarragona, Spain. (e-mail: francisco.gonzalez@urv.cat) 

Manuscript received March 3, 2017; accepted June 26, 2017.
DOI: 10.17694/bajece.337936

Reference [2] proposed the application of 3D bifurcation diagrams for complementing ferroresonance characterization, mainly when more than one parameter can significantly affect the behavior of the ferroresonant nonlinear circuit.

The generation of bifurcation diagrams is however a very tedious task since a high number of simulations has to be run in order to obtain a rigorous representation of the whole phenomenon; that is, a complete parametric study of a ferroresonant scenario can require thousands of runs. In addition, a rather short time step (i.e. less than 10 microseconds) has usually to be considered due to the nonlinearities involved in this phenomenon. This means that for a rather small system model several days of computer time can be necessary for completing the parametric study.

A simple solution to this problem is the application of parallel computing. Indeed, several parametric studies can be simultaneously run using a multicore installation to cover the whole range of parameter values that are of concern.

The approach followed in this work is basically that presented in [2]; it is based on a MATLAB procedure that uses the ATP version of the EMTP to carry out the transient simulations: the MATLAB procedure drives ATP within a multicore installation and collect the generated information to obtain the bifurcation diagram that will characterize the behavior of the test system.

This document has been organized as follows. A short summary on ferroresonance characterization is first presented in Section 2. The tools developed for parametric studies using a multicore installation and the postprocessing tasks that will generate bifurcation diagrams are detailed in Section 3. The remaining sections are dedicated to present some test cases that will illustrate the way in which bifurcation diagrams are generated and their usefulness for ferroresonance analysis.

II. CHARACTERIZATION AND SIMULATION OF FERRORESONANCE

In many scenarios, more than one ferroresonant state is possible, and the operation may jump in and out of ferroresonance modes depending on switching angle or nonlinear circuit parameters. Recorded waveforms corresponding to actual events and results from numerical simulations have led to the classification of ferroresonance states into four different modes [10]:

- **Fundamental mode:** Voltages and currents are periodic

with a period T equal to the power frequency period.

- **Subharmonic mode:** The signals are periodic with a period nT that is a multiple of the source period.
- **Quasi-periodic mode:** This mode is not periodic and exhibits a discontinuous spectrum.
- **Chaotic mode:** The signals show an irregular and unpredictable behavior.

Given the difficulties for distinguishing the normal transient state from the ferroresonant transient state in a ferroresonant circuit, this classification corresponds to the steady state

condition, once the initial transient state is over.

Ferroresonance can be characterized by using either a spectral study method based on Fourier's analysis or a stroboscopic analysis obtained by measuring current i and voltage v at a given point of the system and plotting in plane $v-i$ the instantaneous values at instants separated by a system period. The stroboscopic method, also known as *Poincaré Map* [11], can be used to differentiate between ferroresonance states (i.e., a quasi-periodic state from a chaotic state). A *bifurcation diagram* records the locations of all the abrupt changes in a system signal (e.g., voltage) when a system parameter is quasi-statically varied.

The bifurcation diagram is an alternative to traditional parametric and sensitivity methods for understanding system behavior in ferroresonance analysis. Techniques applied to the calculation of a bifurcation diagram may be based on the principle of continuation [3], [7], experimentation, or time-domain simulation [4], [6]. Reference [2] used time-domain simulation and an ATP-MATLAB link to obtain both 2D and 3D bifurcation diagrams.

If time-domain simulation is used to analyze and predict ferroresonance, it is important to keep in mind that simulation results have a great sensitivity to models and errors in the parameters of nonlinear components. The transformer model is probably the most critical part of any ferroresonance study. Different models and different means of determining the parameters are required for each type of core. Several topology transformer models based on the principle of duality have been presented in the literature [12] - [16]. By default, the transformer model must have an accurate representation of all nonlinear inductances of the core, including hysteresis effects [17] - [19]. Internal capacitances of the transformer might be also considered since they could be crucial in the final development of a ferroresonant process.

Since no standard model is available in any simulation package, tests suggested in the literature cannot be always performed and no standard test has been developed for determining the parameters specified in some models [13], [15], so their use is presently rather limited. Although much effort has been made on refining models for transformers and performing simulations using transient circuit analysis programs such as EMTP and like [20], determining nonlinear parameters is still a challenge.

Other components to be considered, besides the transformer, are the study zone that must be represented in the model, the

source impedance, the transmission or distribution line(s)/cable(s), and any other capacitance not already included from the previous components.

Source representation is not generally critical; if the source does not contain nonlinearities, it is sufficient to use the steady-state Thevenin impedance and the open-circuit voltage. Lines and cables may be represented as *RLC* coupled pi equivalents, cascaded for longer lines/cables. Shunt or series capacitors may be represented as a standard capacitance, paralleled with the appropriate resistance. Transformer stray capacitances may also be incorporated either at the corners of an open-circuited delta transformer winding or midway along each winding.

Since ferroresonance is a nonlinear phenomenon, the conditions with which the phenomenon is initiated will have a significant impact; therefore, residual fluxes, initial capacitance voltages, angles of sources and switches cannot be neglected, see [21], [22]. The latter aspect was analyzed in [2] by varying the switch angle and the phase shift of the source. Both values play a very important role and can decide the final state of the ferroresonance and the length of the transient between the normal operation and the ferroresonant final state [23].

III. PARAMETRIC STUDIES USING A MULTICORE INSTALLATION

A 2D bifurcation diagram records on a plane the locations of all abrupt changes experienced by the final operating state of the test system while one or more system parameters are quasi-statically varied [24]. The 3D bifurcation diagram is based on the variation of two system parameters, stacking as many 2D planes as values given to the second parameter range. The implementation of 3D bifurcation diagrams applies the brute-force method, which consists of repeating time-domain simulations followed by frequency-domain sampling of the same output to determine its periodicity. The procedures for obtaining 2D and 3D bifurcation diagrams were presented in [2].

Parametric studies required to obtain a bifurcation diagram may involve thousands of simulations and take a significant amount of computer time. This time can be significantly reduced by distributing the tasks among several cores. Fig. 1 presents a schematic diagram of the procedure implemented in MATLAB to run ATP in a multicore environment.

A template of the input file corresponding to the test case is firstly elaborated. This template includes the ATP feature Pocket Calculator Varies Parameters (PCVP), normally used to perform parametric studies. By means of the MATLAB procedure, the PCVP section is varied as many times as required to cover the whole range of the first parameter; PCVP is also used to vary the second parameter while the first one remains constant. The user has to specify the range of values and the number of runs for each parameter.

The diagram presented in Fig. 1 shows a procedure with three main parts: (1) data input preparation (aimed at editing input files); (2) data handling and generation of plots; (3) conversion of simulation results produced by ATP (i.e. the so-called PL4 files) to MATLAB format (i.e. MAT files). Note the directions

in which the information is flowing: the MATLAB code generates the final input files, distributes them between cores, controls the ATP runs and the data conversion, reads and manipulates simulation results once they have been translated into in MATLAB code, and finally takes care of the generation of bifurcation diagrams. Data conversion and further post-

processing steps of this procedure take advantage of the previous developments, used for the work presented in reference [2]. For this expanded version, additional MATLAB code was needed to edit ATP input files and distribute them among cores.

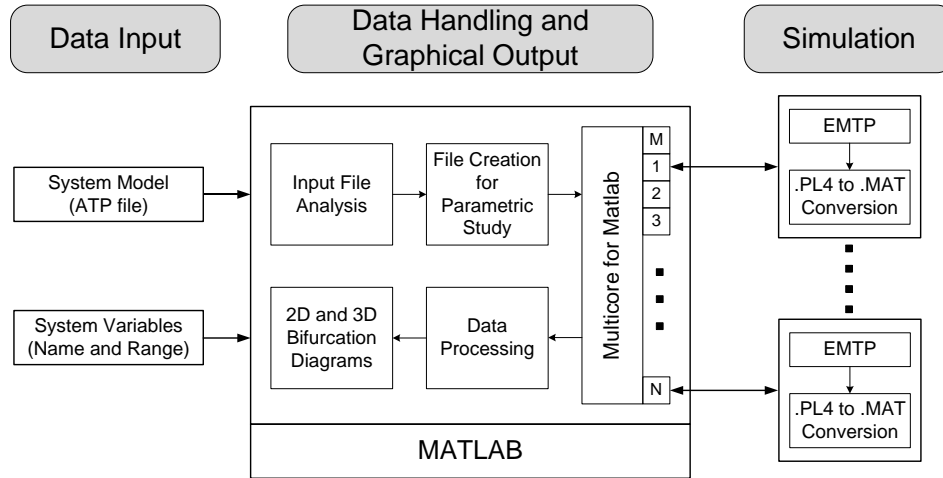


Fig. 1. Flow chart for a 3D plot implementation.

Another important aspect was the size of the files generated by ATP when using PCVP. Since a PL4 file for each combination of the two parameters that are varied to obtain the 3D diagram is needed, the size of the information that has to be manipulated is huge (e.g. if every parameter is varied 200 times, up to 40000 PL4 files will have to be manipulated). To avoid the storage and manipulation of such a quantity of files, the simulations are progressively made; for instance, if 200 runs are to be controlled from PCVP, the same file is run 4 times and the parameter is varied only 50 times within each run. Remember that the ultimate goal is to obtain both 2D and 3D bifurcation diagrams for ferroresonance characterization.

IV. 4. CASE STUDIES

A. Case 1: An Illustrative Example

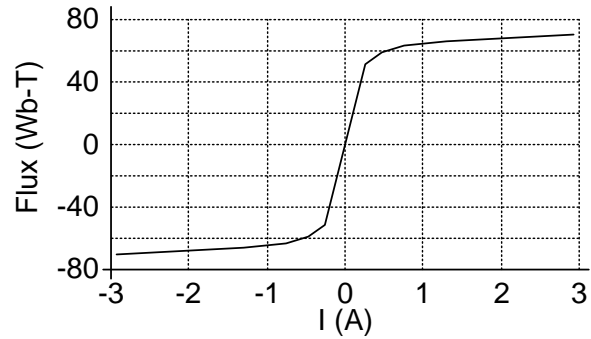
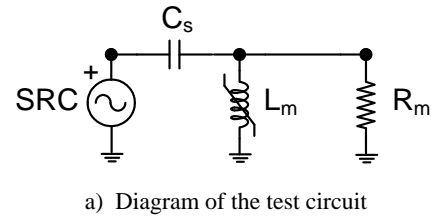
The basic circuit of this example is shown in Fig. 2a. The circuit is composed of a 25 kV, 50 Hz ideal voltage source, a capacitance of 0.1 μ F and a saturable inductance (see Fig. 2b) paralleled with a resistance of 40 Ω [25]. The shifting angle of the voltage source is -90° , being zero both the initial capacitance voltage and the residual flux in the saturable inductance. The simulation is carried out without introducing any switching event.

Using the above parameters, the resulting voltage in the inductor is that shown in Fig. 3a; it can be easily identified as a periodic ferroresonant signal.

Consider now that the value of the resistance is infinite; that is, assume a lossless circuit. Fig. 3b shows the new time-domain response. Notice, however, that the ferroresonant signal in Fig. 3b cannot be easily characterized, since it is not possible to distinguish between a chaotic and a quasi-periodic mode.

The 3D diagram elaborated according to the procedure proposed in [2] and created by slowly varying C_s (parameter

K1), from 0 to 1 μ F, and R_m (parameter K2), from 0 to 40 k Ω , is shown in Fig. 4.



b) Non-linear inductance characteristic

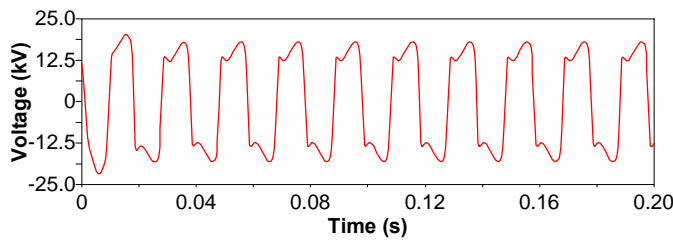
Fig. 2. Case 1: Test circuit.

This plot is basically the same that was previously presented in [2].

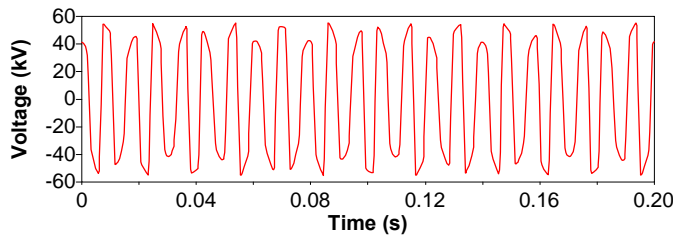
Note that even though ferroresonance is present in almost any match C_s - R_m , there are two intervals (i.e., $C_s = 0 \div 0.2 \mu$ F and $R_m \leq 10$ k Ω) in which the signal is completely damped. Notice also that the surrounded light blue area remains below the nominal voltage.

The 3D bifurcation diagram summarizes a parametric study and can be used to select design parameters for newer systems

and predict beforehand whether in a ferroresonant event the values will remain or not in a non-destructive zone. Besides, the diagram can be easily applied for analyzing the impact on given equipment by indicating in a chosen color (e.g., red color) the range of values for which equipment failure could occur.



a) Ferroresonant signal – Lossy circuit, $R_m=40\text{ k}\Omega$ and $C_s=0.1\text{ }\mu\text{F}$



b) Ferroresonant signal – Lossless circuit, $R_m=\infty$ and $C_s=0.1\text{ }\mu\text{F}$

Fig. 3. Ferroresonance (lossless) test circuit. Simulation results.

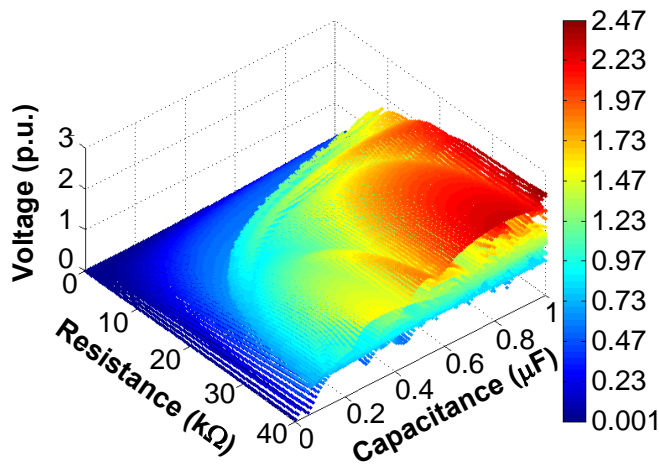


Fig. 4. Case 1: 3D bifurcation diagram.

B. Case 2: Ferroresonant Behavior of a Voltage Transformer

This study is based on a work presented in [8], and deals with a ferroresonance case that involves inductive voltage transformers (VTs) in a substation equipped with circuit breaker grading capacitors.

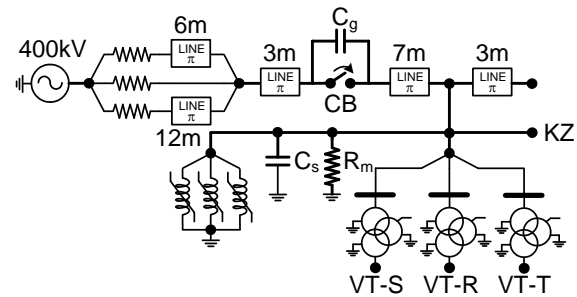
Fig. 5a shows the diagram of the model implemented in ATPDraw, based on the BCTRAN model; Fig. 5b shows some relevant information for ferroresonant studies.

The system consists on a 400 kV busline and a branch feeding a transformer bank with no residual flux. The cable lengths and the grading capacitance of the circuit breaker CB are shown in the figure. More information about the test system is provided in the Appendix.

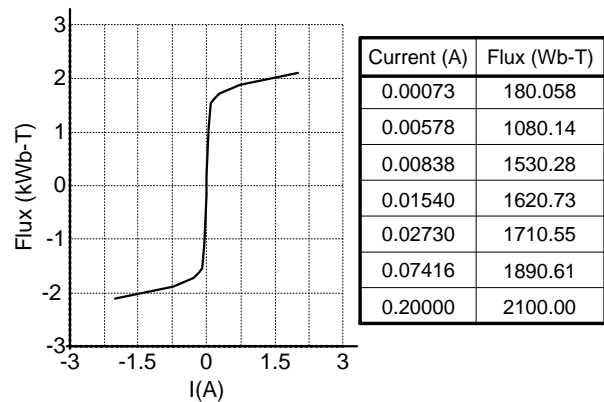
All capacitances are initially discharged, the phase angle of

the source is 0° and the closing of the switch is performed at $t = 0.3\text{ s}$.

A catastrophic incident was reported when the three phase breaker (CB) was opened [8].



a) Diagram of the test circuit



b) Saturation curve of the voltage transformer (VT-S, VT-R, VT-T)

Fig. 5. Case 2: Test system.

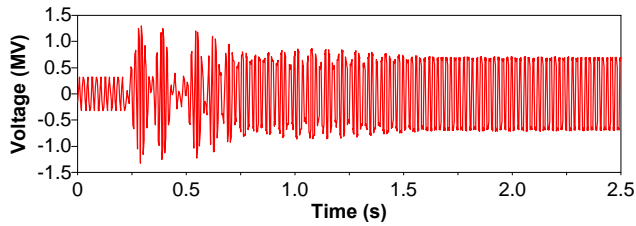
The operation left the grading capacitance connected in series to the nonlinear inductance of a transformer bank connected to the same line. The ferroresonant signal is presented in Fig. 6a. After a study aimed at analyzing the influence of the value C_s , it was discovered that for a range of values the result could be much different, see Fig. 6b. The stray capacitance C_s and the grading capacitance C_g are recognized as major influence parameters in the ferroresonant system. In this example, the values of C_s and C_g are respectively 490 pF and 600 pF [8].

The 3D diagram depicted in Fig. 7 was again constructed following the procedure presented in [2] using C_s and C_g as parameters. The z axis gives the per-unit value of the voltage at node KZ (phase B), and referred to the source voltage. One can easily note that with most combinations of C_s and C_g , the resulting mode of ferroresonance will not exceed the 1 p.u. value, except for those values of C_s lower than 200 pF, an interval that can unfold chaotic mode with voltage values of up to 4 p.u. This plot is again the same that was presented in [2].

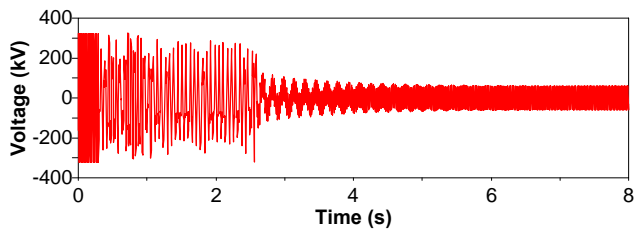
C. Case 3: Ferroresonance in a Five-Legged Transformer

This case is based on a series of studies conducted in the early 1990's and aimed at synthesizing experimental work and modeling of five-legged core transformers driven to a ferroresonance condition. Originally, the National Rural Electric Cooperative Association (NRECA) funded a study in

1986 and 1987 to assess the problem on rural electric cooperative systems.



a) $C_s=490$ pF and $C_g=600$ pF



b) $C_s=2590$ pF and $C_g=600$ pF

Fig. 6. Case 2: Simulation results.

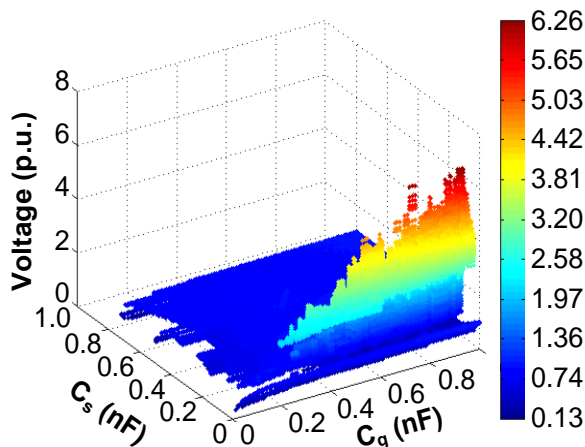


Fig. 7. Case 2: 3D bifurcation diagram.

Several reports were released describing overvoltage condition problems related to five-legged core transformers operating with the grounded-wye connection [26]. This situation induced the need to develop a transformer model that would efficiently analyze the causes of the phenomenon [27]. After some validation work, the problem under study could be categorized as a ferroresonance phenomenon [28]. An ATP model of a five-legged core transformer was later proposed in [29]. That study was aimed at analyzing the ferroresonant response of the transformer to changes in the capacitance of the cable between the transformer and the source.

Fig. 8 shows the model implemented in ATPDraw and the characteristics of the saturable inductances. More information about the test system is provided in the Appendix.

This case analyzes the effects in the ferroresonance final stage provoked by the cable capacitance and the source voltage regulation ($\pm 10\%$). Some simulation results showing the ferroresonance state in phase A are presented in Fig. 9.

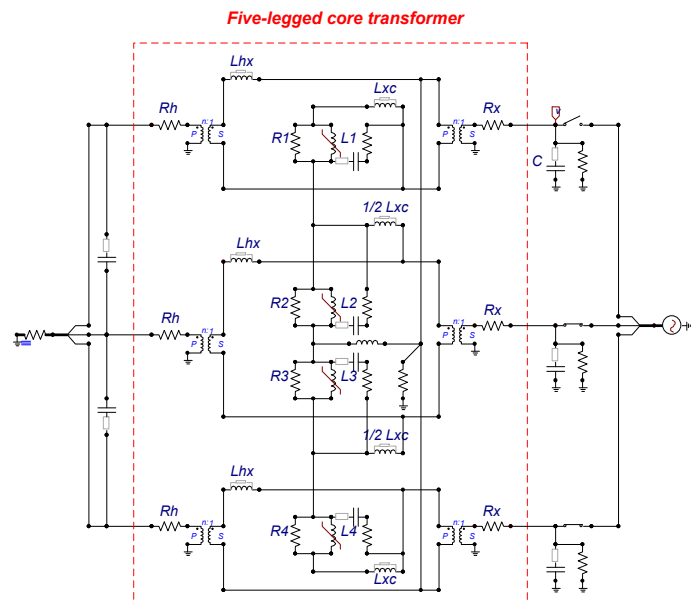
Since the ferroresonant situation starts along with the simulation, the switch between the source and the phase A is left open (see Fig. 8), and the initial capacitance voltage and the residual flux are set to zero. After running a series of simulations it was possible to understand how the capacitance value, the switching angle and the source voltage were directly affecting the final state of the ferroresonance. Thus, the capacitance has been varied from 0 to 30 μF , while the source voltage has been varied from 432 to 528 V. All tests were carried out assuming a no load condition (represented by means of a very high resistance).

An extensive parametric study has been again resumed using the 3D bifurcation diagram; the diagram has been obtained from 90000 runs. Fig. 10 show the resulting 3D diagram for the source voltage variation. From this plot it is possible to easily locate those potentially destructive zones as well as zones where the oscillation peaks are harmless for equipment and protections (i.e. they are not higher than 0.5 p.u.).

V. AN EXTENSION OF BIFURCATION DIAGRAMS

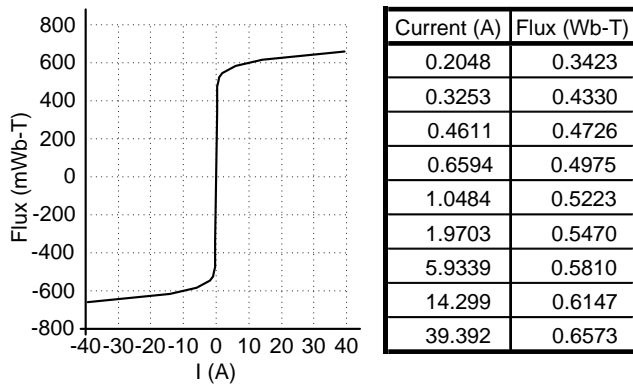
An extension of the bifurcation diagram can be made by introducing the idea of a 4D diagram, which may consist of varying three individual parameters and collecting the voltage peaks resulting of the induced ferroresonance. The peaks selected are then colored according to its severity; this may enhance the map by avoiding the use of an axis representing the peaks. The example selected to illustrate the advantage of a 4D diagram is based on the first case study presented in Section IV.A. The parameters to be evaluated are: resistance R_m , capacitance C_s , and the power source variation ($\pm 10\%$).

The “fourth axis” is the colored range given to the output voltage. Fig. 11 shows the resulting map. Dark red areas represent zones with ferroresonance peaks above twice the rated value.

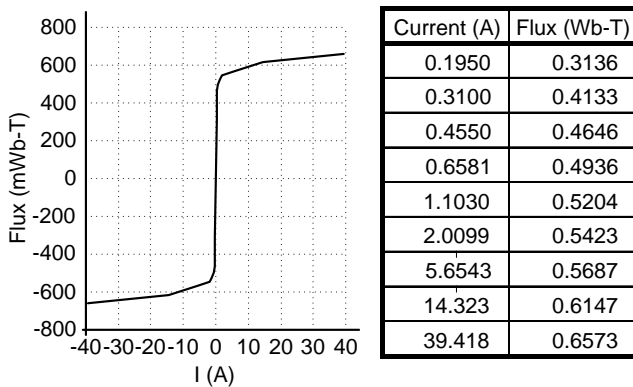


a) Diagram of the test system.

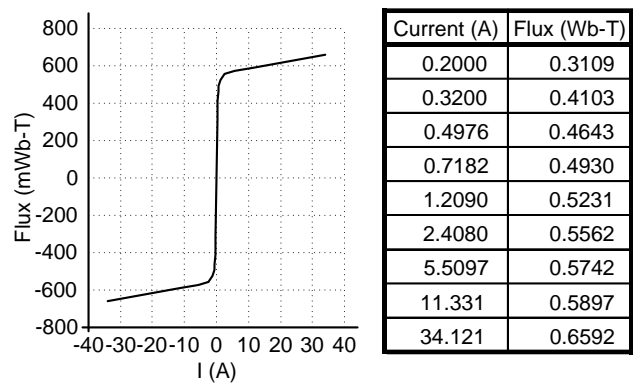
Fig. 8. Case 3: System model in ATPDraw.



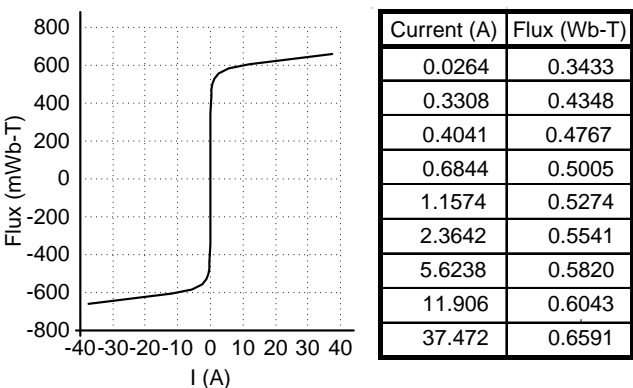
b) Saturation curve of the inductance L_1



c) Saturation curve of the inductance L_2

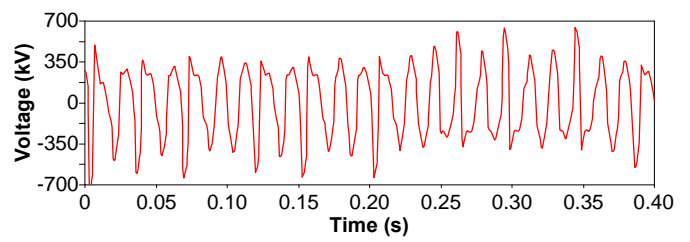


d) Saturation curve of the inductance L_3

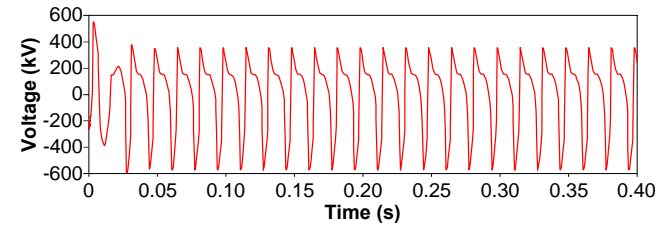


e) Saturation curve of the inductance L_4

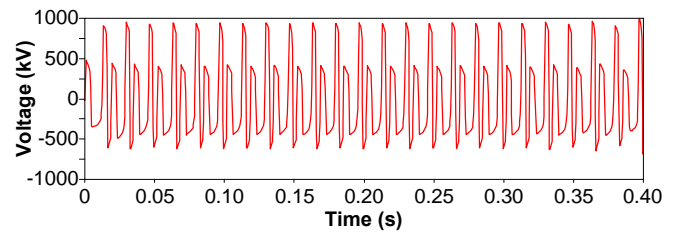
Fig. 8. Case 3: System model in ATPDraw (cont.).



a) Shift angle = -90° , Capacitance = 15 μF , Source voltage = 480 V



b) Shift angle = -90° , Capacitance = 10 μF , Source voltage = 440 V



c) Shift angle = 0° , Capacitance = 25 μF , Source voltage = 500 V

Fig. 9. Case 3: Phase A – Some ferroresonant signals.

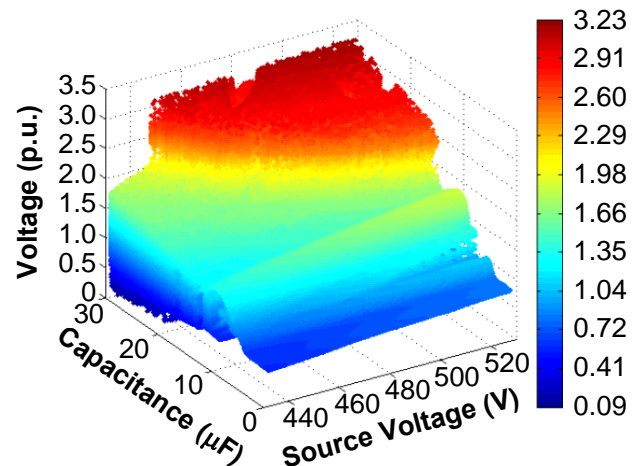


Fig. 10. Case 3: 3D bifurcation diagram.

To facilitate the interpretation, the map can be separated in sub-plots containing the range of values of interest. Fig. 12 introduces the section of the map for those peaks colored in red and corresponding to the highest ferroresonance voltages.

VI. CONCLUSION

Parametric studies can be very useful to detect parameter ranges of concern in some transient phenomena. The CPU time required to carry out some of these analyses can be too long, mainly if a short or very short time step must be considered and a high number of runs is necessary to cover the full range of parameter values.

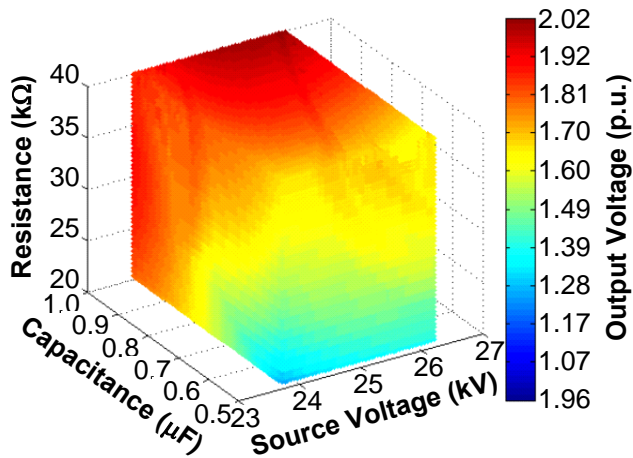


Fig. 11. Case 1: 4D bifurcation diagram.

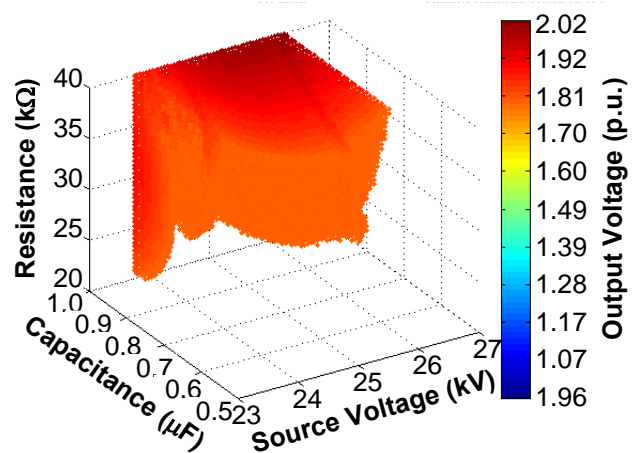


Fig. 12. Case 1: Selected segments of the 4D bifurcation diagram.

An efficient option is the usage of a multicore installation where the runs are shared among the cores. The work presented here is based on a previous work that proposed 3D bifurcation diagrams as a technique for a good comprehension of the behavior of a power system while driven into a ferro-resonant state. This technique can also be used to establish the roadmap of a hypothetical ferroresonant situation, pointing the safe zones in which the parameter under study should be selected.

This paper has presented the application of a parallel MATLAB procedure for creating bifurcation diagrams that can characterize ferroresonant situations. Since the reduction of the simulation time is obviously proportional to the number of cores, some studies can easily become affordable by using a few dozens of cores. Some useful information about the cases studied in this paper is provided in Table I. In order to understand the advantage of this approach it can be mentioned that all the cases studied here required several days of single-CPU time to obtain all the information needed for creating the corresponding 3D plot. The 4D map has been obtained after 125000 simulations and contains up to 6125000 points. The total simulation time was around 6 hours.

It is important to point out the factors influencing the duration of the total simulation time, which are: The amount of

simulations, individual simulation time and the integration time step.

Finally, it is important to emphasize the influence of the transformer model on the results and therefore the bifurcation diagrams obtained with the present methodology. Reference [30] shows that for single-phase transformers an accurate ferroresonance study can only be carried out when the saturable cores are represented by means of a hysteretic core. All case studies presented in this paper were carried out by using a non-hysteretic representation of transformer cores; therefore, results presented here should be used with care.

TABLE I.
SIMULATION TIMES-50 CORES

Test Case	Parameters	Tmax	Time step	Runs	CPU time
1	$R_m: 0 \div 40 \text{ k}\Omega;$ $C_s: 0 \div 1 \text{ }\mu\text{F}$	1 s	1 μs	200×200	6031 s
2	$C_s: 0 \div 1 \text{ nF};$ $C_g: 0 \div 1 \text{ nF}$	8s	10 μs	200×200	8621 s
3	$V: 432 \div 528 \text{ V};$ $C: 0 \div 30 \text{ }\mu\text{F}$	1s	1 μs	300×300	35558 s

APPENDIX

A. Case 2 – Main Parameters

Power source (ideal): L-L Voltage = 400 kV; Frequency = 50 Hz.

Cables: They are represented by constant-parameters PI models. Their lengths vary between 3 and 12 m.

Circuit breaker: It is represented by a grading capacitance, C_g , with variable value.

Voltage transformers (VTs): Main characteristics

- Single-phase three-winding transformer
- Ratings: 400/0.1/0.033 kV, 0.1/0.1/0.05 kVA.
- Short-circuit test values: $Z_{sh,1w-2w} = 13.46 \%$, $Z_{sh,1w-3w} = 20 \%$, $Z_{sh,2w-3w} = 20 \%$.
- No load test losses: $R_m = 182 \text{ M}\Omega$.
- Saturation curve shown in Fig. 7.

Stray capacitance (C_s): Variable value.

B. Case 3 – Main Parameters

Power source: L-L Voltage = 230 kV; Frequency = 60 Hz; Per phase short-circuit impedance = $0.2116 \Omega + j4.3801 \Omega$.

Bus-line B1-B2: Per phase values are as follows

Line Filter 1: $R = 2.17 \Omega$; $X = 16.72 \Omega$; $C = 0.938 \text{ }\mu\text{F}$.

Line Filter 2: $R = 1.84 \Omega$; $X = 16.74 \Omega$; $C = 1.31 \text{ }\mu\text{F}$.

Bus-lines interconnections: They are represented by a PI arrangement of capacitances with the following values

Series capacitance $C_Y = 0.001108 \text{ }\mu\text{F}$.

Parallel capacitance $C = 0.005316 \text{ }\mu\text{F}$.

Circuit breaker: It is represented by a grading capacitance, C_g , with variable value.

Bus-line A1-A2: It is represented by a stray capacitance, C_s , with variable value.

Voltage transformers (V13F, V33F):

- YNyn0 three-phase two-winding transformers
- Rated voltages: 230/0.115 kV.

- Short-circuit test: $R_{sh,1w} = 7490 \Omega$, $X_{sh,1w} = 0.001 \Omega$; $R_{sh,2w} = 0.0463 \Omega$, $X_{sh,2w} = 0.1642 \Omega$.
- No load test (steady state): Current = 0.00478 A; Flux = 0.38 W-T; Core loss resistance $R_m = 9.52 \text{ M}\Omega$.
- Saturation curve shown in Fig. 12.

Substation transformer (SST2):

- YNy0 Three-phase two-winding transformer, grounded through a 2.4Ω impedance.
- Rated voltages = 230/4.16 kV
- Short-circuit test: $R_{sh,1w} = 12 \Omega$, $X_{sh,1w} = 322.69 \Omega$; $R_{sh,2w} = 0.0012 \Omega$, $X_{sh,2w} = 0.1056 \Omega$.
- No load test (steady state): Current = 0.02485 A; Flux = 0.04 W-T; Core loss resistance: $R_m = 3.11 \text{ M}\Omega$.
- Saturation curve shown in Fig. 12.

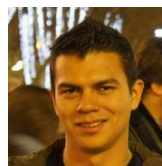
Load (connected to V13F and V33F): Per phase values

$R = 163.2 \Omega$; $X = 0.268 \Omega$.

REFERENCES

- [1] M.R. Iravani, A.K.S. Chaudhary, W.J. Giewbrecht, I.E. Hassan, A.J.F. Keri, K.C. Lee, J.A. Martinez, A.S. Morched, B.A. Mork, M. Parniani, A. Sarshar, D. Shirmohammadi, R.A. Walling, and D.A. Woodford, "Modeling and analysis guidelines for slow transients: Part III: The study of ferroresonance," *IEEE Trans. on Power Delivery*, vol. 15, no. 1, pp. 255-265, January 2000.
- [2] J. A. Corea-Araujo, F. González-Molina, J. A. Martínez, J. A. Barrado-Rodrigo, and L. Guasch-Pesquer, "Tools for characterization and assessment of ferroresonance using 3-D bifurcation diagrams," *IEEE Trans. on Power Delivery*, vol. 29, no. 6, pp. 2543-2551, December 2014.
- [3] C. Kieny, "Application of the bifurcation theory in studying and understanding the global behavior of a ferroresonant electric power circuit," *IEEE Trans. on Power Delivery*, vol. 6, no. 2, pp. 866-872, April 1991.
- [4] P.S. Bodger, G.D. Irwin, D.A. Woodford, and A.M. Gole, "Bifurcation route to chaos for a ferroresonant circuit using an electromagnetic transients program," *IEEE Proc. Gener. Transm. Distrib.*, vol. 143, no. 3, pp. 238-242, May 1996.
- [5] A. Ben-Tal, D. Shein, and S. Zissu, "Studying ferroresonance in actual power systems by bifurcation diagram," *Electric Power Systems Research*, vol. 49, no. 3, pp. 175-183, April 1999.
- [6] D.A.N. Jacobson, P.W. Lehn, and R.W. Menzies, "Stability domain calculations of period-1 ferroresonance in a nonlinear resonant circuit," *IEEE Trans. on Power Delivery*, vol. 17, no.3, pp. 865-871, 2002.
- [7] F. Wörnle, D.K. Harrison, and C. Zhou, "Analysis of a ferroresonant circuit using bifurcation theory and continuation techniques," *IEEE Trans. on Power Delivery*, vol. 20, no. 1, pp. 191-196, January 2005.
- [8] M. Val Escudero, I. Dudurych, and M.A. Redfern, "Characterization of ferroresonant modes in HV substation with CB grading capacitor," *Electric Power Systems Research*, vol. 77, no. 1, pp. 1506-1513, 2010.
- [9] F. Ben Amar and R. Dhifaoui, "Study of the periodic ferroresonance in the electrical power networks by bifurcation diagrams," *Electrical Power and Energy Systems*, vol. 33, pp. 61-85, 2011.
- [10] P. Ferracci, Ferroresonance, *Cahier Technique no. 190*, Groupe Schneider, 1998.
- [11] R. Hilborn, *Chaos and Nonlinear Dynamics: An Introduction for Scientists and Engineers*. New York: Oxford University Press, 2001.
- [12] S. Jazebi, A. Farazmand, B. Perinkolam Murali, and F. de León, "Comparative study on π and T equivalent models for the analysis of transformer ferroresonance," *IEEE Trans. on Power Delivery*, vol. 28, no. 1, pp. 526-528, January 2013.
- [13] J.A. Martinez, R. Walling, B. Mork, J. Martin-Arnedo, and D. Durbak, "Parameter determination for modeling systems transients. Part III: Transformers," *IEEE Trans. on Power Delivery*, vol. 20, no. 3, pp. 2051-2062, July 2005.
- [14] B.A. Mork, F. Gonzalez, D. Ishchenko, D.L. Stuehm, and J. Mitra, "Hybrid transformer model for transient simulation-Part I: Development and parameters," *IEEE Trans. on Power Delivery*, vol. 22, no. 1, pp. 248-255, January 2007.
- [15] F. de León, P. Gómez, J.A. Martinez-Velasco, and M. Rioual, "Transformers," Chapter 4 of *Power System Transients. Parameter Determination*, J.A. Martinez-Velasco (ed.), CRC Press, 2009.
- [16] S.E. Zırka, Y.I. Moroz, C.M. Arturi, N. Chiesa, and H.K. Hoidalen, "Topology-correct reversible transformer model," *IEEE Trans. on Power Delivery*, vol. 27, no. 4, pp. 2037-2045, October 2012.
- [17] A. Rezaei-Zare, R. Iravani, and M. Sanaye-Pasand, "Impacts of transformer core hysteresis formation on stability domain of ferroresonance modes," *IEEE Trans. on Power Delivery*, vol. 24, no. 1, pp. 177-186, January 2009.
- [18] A. Rezaei-Zare, R. Iravani, M. Sanaye-Pasand, H. Mohseni, and S. Farhangi, "An accurate hysteresis model for ferroresonance analysis of a transformer," *IEEE Trans. on Power Delivery*, vol. 23, no. 3, pp. 1448-1456, July 2008.
- [19] P. Moses, M.A.S. Masoum, and H.A. Toliyat, "Impact of hysteresis and magnetic couplings on the stability domain of ferroresonance in asymmetric three-phase three-leg transformers," *IEEE Trans. on Power Delivery*, vol. 26, no. 2, pp. 581-592, 2011.
- [20] H.W. Dommel, *EMTP Theory Book*, Bonneville Power Admin., Portland, August 1986.
- [21] K. Miličević and Z. Emin, "Impact of initial conditions on the initiation of ferroresonance," *Int. J. of Electrical Power and Energy Systems*, vol. 31, pp. 146-152, 2009.
- [22] K. Miličević, D. Vinko, and Z. Emin, "Identifying ferroresonance initiation for a range of initial conditions and parameters," *Nonlinear Dynamics*, vol. 66, pp.755-762, 2011.
- [23] J.A. Corea-Araujo, F. Gonzalez-Molina, J.A. Martinez-Velasco, J.A. Barrado-Rodrigo, and L. Guasch-Pesquer, "An EMTP-based analysis of the switching shift angle effect during energization/de-energization in the final ferroresonance state," *IPST*, Vancouver, July 2013.
- [24] T.S. Parker and L.O. Chua, *Practical Numerical Algorithms for Chaotic Systems*, Springer, 1989.
- [25] J.A. Martinez-Velasco and J.R. Martí, *Electromagnetic Transients Analysis, Chapter 12 in Electric Energy Systems: Analysis and Operation*, A. Gomez-Exposito, A. Conejo, and C. Cañizares (Eds.), CRC Press, Boca Raton, 2008.
- [26] D.D. Mairs, D.L. Stuehm, and B.A. Mork, "Overvoltages on five-legged core transformers on rural electric systems," *IEEE Trans. on Industry Applications*, vol. 25, no. 2, pp. 366-370, March/April 1989.
- [27] D.L. Stuehm, B.A. Mork, and D.D. Mairs, "Five-legged core transformer equivalent circuit," *IEEE Trans. on Power Delivery*, vol. 4, no. 3, pp. 1786-1793, July 1989.
- [28] D.L. Stuehm, B.A. Mork, and D.D. Mairs, "Ferroresonance with three-phase five-legged core transformers," *Minnesota Power Systems Conference*, Minneapolis, MN, October 3, 1988.
- [29] B.A. Mork, "Ferroresonance and Chaos - Observation and Simulation of Ferroresonance in a Five Legged Core Distribution Transformer," Ph.D. Thesis, North Dakota State University, 1992.
- [30] J.A. Corea-Araujo, J.A. Martinez-Velasco, F. González-Molina, J.A. Barrado-Rodrigo, L. Guasch-Pesquer, and F. Castro-Aranda, "Validation of single-phase transformer model for ferroresonance analysis," Accepted for publication in *Electrical Engineering*.

BIOGRAPHIES



JAVIER A. COREA-ARAUJO was born in San Salvador (El Salvador). He received his Electrical engineering degree from Universidad de Sonsonate (El Salvador). He received his M.S. and Ph.D. degree from Universitat Rovira i Virgili (Spain) in 2010 and 2015, respectively. Nowadays, he is a researcher at Universitat Politècnica de Catalunya (Spain). His research interests include transient analysis of power systems and EMTP modeling.



GERARDO GUERRA was born in San Salvador (El Salvador). He received his B.S. in Electrical Engineering from Universidad Centroamericana (El Salvador). He received his M.S. and Ph.D. from Universitat Politècnica de Catalunya (Spain) in 2012 and 2016, respectively. His research interests include

integration of renewable generation, power distribution reliability, and application of high performance computing to power systems.



JUAN A. MARTINEZ-VELASCO was born in Barcelona (Spain). He is Profesor Titular at the Departament d'Enginyeria Elèctrica of the Universitat Politècnica de Catalunya. His teaching and research interests include transmission and distribution, power system analysis, and EMTP applications.



FRANCISCO GONZALES-MOLINA was born in Barcelona (Spain). He received the M.S. and Ph.D. degrees from Universitat Politècnica de Catalunya, in 1996 and 2001, respectively. Nowadays, Dr. Gonzalez works as Assistant Professor at the Universitat Rovira i Virgili (Spain). His research interests include transient analysis of power systems, lightning performance of transmission and distribution lines, power quality, and

renewable energy.

A Note on Commensurate-Order Characteristic Root Equivalency Class of Linear Time Invariant Systems

B. B. Alagoz


Abstract—This study investigates characteristic root equivalency relations between commensurate order and integer order Linear Time Invariant (LTI) systems. Author introduces some useful properties of a special class of commensurate order systems, which is called characteristic root equivalency class of LTI systems. These properties present potential to facilitate design and analysis efforts of this class of commensurate order systems. In this sense, straightforward stability checking procedures and design approaches for commensurate order root equivalent systems of the first and second order LTI systems are demonstrated. Findings of the study are validated by illustrative examples.

Index Terms— Fractional order systems, characteristic root equivalency, stability, design, analysis.

I. INTRODUCTION

THERE has been a growing interest for utilization of Fractional Calculus (FC) in engineering and science problems because of its promises of better describing real world objects and phenomenon [1-5]. It was suggested that real world objects can be more accurately modeled and analyzed by using FC because real world objects do not have to precisely comply with integer order system models: Majority of them may exhibit fractionality even at a low degree [1,2,5-10]. The fractional order derivative and integration were shown to act upon solutions of many problems in physics [6,7,8], thermodynamics [9], electrical circuits theory and fractances [10,11,12], mechatronics systems [13], chaos theory [14], control systems [15,16,17] etc.

Linear Time Invariant (LTI) systems have been used as a fundamental and substantial modeling tool for theoretical analyses of real systems [18]. Extensive researches on LTI systems offered well established mathematical background, simplified solutions, experimentally proven methods for the characterization and analysis of real systems. In these analyses, LTI system models can be expressed in many forms such as differential equations, state space models and transfer function forms [18]. LTI system modeling techniques, system stability, observability and controllability issues have been studied extensively and applied in engineering problems.

B. B. ALAGOZ, is with Department of Computer Engineering, Inonu University, Malatya, Turkey, (e-mail: baykant.alagoz@inonu.edu.tr). 

Manuscript received May 16, 2017; accepted August 11, 2017.
DOI: [10.17694/bajece.337929](https://doi.org/10.17694/bajece.337929)

In recent years, fractional order LTI systems have become the most underpinning topic of researchers and there are extensive researches ongoing for problems of fractional order system stability [19-33], identification, implementation and computation methods [20]. Nonetheless, rather deepened investigations on fractional order LTI system properties are still required for better understanding fractional dynamics of real world systems.

Commensurate order LTI systems are indeed a class of fractional order systems, which provides simplification for analysis and design efforts because it has a proper expression of fractional orders in the form of $k\alpha$, $k = 0,1,2,3...$. Thus, the order fractionality of commensurate order LTI systems can be expressed by a single order parameter $\alpha \in R$. For the integer values of order $\alpha = 1,2,3...$, the system turns into conventional integer order LTI systems. As known, system behavior and model structure strongly depends on root locus of LTI system. Investigating effects of fractional order α on root placement of characteristic equations on complex plane can be helpful to explain connections between fractional order LTI system model and integer order LTI system model.

This study investigates properties of a special class of commensurate order systems. This class of system models has the same characteristic root set for different commensurate order ($\alpha \in R$). These systems were referred to as characteristic root equivalent systems and the characteristic root equivalency was used to establish arithmetical relation between fractional order systems and integer order systems [24]. In the current study, author addresses some fundamental aspects of characteristic root equivalency families of the first and second order LTI systems. It is observed that the root equivalency formed by α order shifts the roots of the characteristic equation in complex plane and thus draws a root trajectory with respect to the commensurate order α . This trajectory represents root locus of root equivalency class of commensurate order systems in complex domain and properties of these trajectories can provide useful information for system analysis and design. On the other hand, characteristic root equivalent systems have complex coefficients and this causes implementation complications for real-valued systems. In order to transform the complex coefficient root equivalent systems into real coefficient commensurate order systems, we use complex conjugate root addition method.

II. METHODOLOGY

A. Basic definitions

Characteristic root equivalence family of fractional order systems were introduced in [24]. Here, we consider root equivalency class of commensurate order LTI systems.

Fractional order characteristic root equivalency: Let's assume characteristic polynomial of a first order LTI system be expressed as $s - \nu = 0$ in s-domain. For a given fractional order $\alpha \in R$, fractional order root equivalent of this root can be defined by $s^\alpha - \nu^\alpha = 0$.

Proof: The root of characteristic equation $s - \nu = 0$ can be solved as $s = \nu$. By applying α power to the both sides of the equation $s = \nu$, one can obtain $s^\alpha = \nu^\alpha$. In this case, α -order root equivalent characteristic equation can be written in the form of $s^\alpha - \nu^\alpha = 0$. The transformation of $s = \nu$ into $s^\alpha = \nu^\alpha$ is called as α -order root equivalency.

Characteristic root equivalent commensurate order systems: Let's consider commensurate systems in its simple state space form $X^{(\alpha)} = AX$. For a given fractional order $\alpha > 0$ and integer order characteristic polynomial $\Delta(s) = \prod_{i=1}^n (s - \nu_i)$,

where $\nu_1, \nu_2, \nu_3, \dots, \nu_n, n \in Z^+$ are complex roots of system, after applying $s^\alpha = \nu_i^\alpha$ transformation to all roots of $\Delta(s)$, α -order root equivalent commensurate order polynomial family of the integer order characteristic polynomial is defined as

$$\Delta_c = \left\{ \det(s^\alpha I - A) = \prod_{i=1}^n (s^\alpha - \nu_i^\alpha) : \alpha \in (0,1) \cup (1,2) \vee n \in Z^+ \right\}.$$

B. Effects of fractional order root equivalency

In this section, we study root equivalency of the first order LTI systems. In further sections, we extent our analyses on root equivalency to second order systems. The first order LTI systems establish the most basic form of root equivalent fractional order systems.

Let consider a commensurate order LTI system, defined in form of $x^{(\alpha)} = \nu x(t) + Ku(t)$, where $u(t)$ and $x(t)$ are input and state of the system, respectively. The system output was assumed as $y(t) = x(t)$ and a zero initial state ($x(0) = 0$) is used for the sake of computational simplicity. The transfer function of the first order LTI system for $\alpha = 1$ is expressed in general form as,

$$T(s) = \frac{K}{s - \nu}. \tag{1}$$

Characteristic polynomial of the system $T(s)$ can be obtained as $\Delta(s) = (s - \nu)$. By applying α order root equivalency mapping to the root by $s^\alpha = \nu^\alpha$, the α -order root equivalence system family of $T(s)$ can be written as,

$$T_\alpha(s) = \frac{K}{s^\alpha - \nu^\alpha} = \frac{K}{s^\alpha - M^\alpha e^{j\alpha\theta}}. \tag{2}$$

In equation (1), the root of $\Delta(s)$ is written in the complex form as $\nu = Me^{j\theta}$, where M is magnitude and θ is angle of complex root, respectively. For the real coefficient first order LTI systems, root angle θ takes two values: $\theta = \pi$ radian for stable systems and $\theta = 0$ radian for unstable systems. One can write the α -order root equivalent of ν in the complex form as $\nu^\alpha = M^\alpha e^{j\alpha\theta}$. This reveals the following fundamental property of the α -order root equivalency in complex plane:

- (i) *Nonlinear scaling of root magnitude:* Due to $s^\alpha = \nu^\alpha$ transformation, root amplitude is scaled by the power of $\alpha \in R$. In other word, the root magnitude goes from M to M^α . ($M \rightarrow M^\alpha$). (i) If $\alpha < 1$ then $M^\alpha < M$, and (ii) if $\alpha > 1$ then $M^\alpha > M$ as illustrated in Fig. 1.
- (ii) *Linear scaling of root angle:* Due to $s^\alpha = \nu^\alpha$ transformation, root angle is scaled proportional to the order α . In other words, the root angle goes from θ to $\alpha\theta$. ($\theta \rightarrow \alpha\theta$). (i) If $\alpha < 1$ then $\alpha\theta < \theta$ and (ii) if $\alpha > 1$ then $\alpha\theta > \theta$ as illustrated in Fig. 1.

TABLE I.
EFFECT OF α -ORDER ROOT EQUIVALENCY ON THE COMPLEX ROOTS

	Integer order	α -order	Effect
Magnitude	M	M^α	Nonlinear scaling of root magnitude
Angle	θ	$\alpha\theta$	Linear scaling of root angle

Table 1 summarizes effects of α -order root equivalency on the complex roots. These effects in the root locus is referred as to root equivalency shifting with the α -order. Fig. 1 illustrates this root shifting effect for a stable first order LTI system, which occurs in clockwise direction for $\alpha < 1$ and counterclockwise direction for $\alpha > 1$. The root angle takes discrete angle values, $\theta = \{0, \pi\}$ for a first order LTI system. The root of first order LTI ($\alpha = 1$) is reel for real coefficient first order transfer functions. However, for root equivalent fractional order systems, root angle takes continuous angle values, defined as $\theta = \{0, \alpha\pi\}$ for an $\alpha \in R$ and the trace of shifting root, which is $\alpha\pi$, draws a root equivalency trajectory, which depicts root locus of root equivalency family in the complex plane.

Effects of fractional order on system stability and the first Riemann sheet were discussed in detail in Ref [1,21-24]. By applying $s = u^m$ transformation to characteristic polynomial of fractional order systems, the stability analysis of a fractional order system based on the root locus was confined in the first Riemann sheet that is defined as the portion of complex plane with angle range of $-\pi/m \leq \phi \leq \pi/m$.

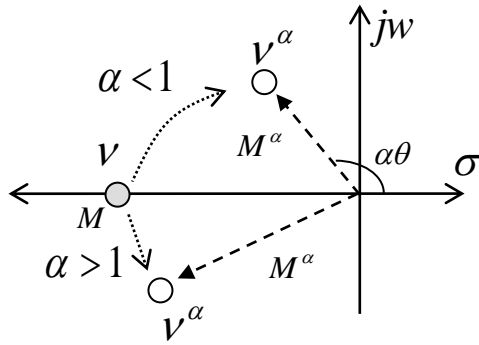


Fig. 1. A representation of root locus shifting effect for a stable first order LTI system

Fig. 2 shows the possible trajectories of shifting roots for $\alpha \in [0, 3.1]$ and different root magnitudes (M). These trajectories are calculated by $v^\alpha = M^\alpha e^{j\alpha\theta}$ to indicate family of root equivalent systems, graphically. As seen in the figure, the magnitude M yields three trajectory types: For $M > 1$ (expanding trajectory), it follows an expanding circular route and the root magnitude increases depending on α . For $M = 1$ (circulating trajectory), it follows a steady circular route and the order α do not change the root magnitude. In the case of $M < 1$ (narrowing trajectory), it follows a narrowing circular route and the root magnitude decrease depending on the α . It is already known that root magnitude takes effect on the response time of a stable system. As magnitude decreases, system response is getting slower.

By considering $e^{j\alpha\theta} = \cos(\alpha\theta) - j\sin(\alpha\theta)$ in equation (2), one can express the root equivalent family of first order LTI systems in the form of

$$T_\alpha(s) = \frac{K}{s^\alpha - M^\alpha \cos(\alpha\theta) - jM^\alpha \sin(\alpha\theta)} \quad (3)$$

The α order root equivalency mostly generates complex coefficient system models from real coefficient first order LTI system models due to the fact that first order system has a single real root without any conjugate pair with respect to real axis and this root moves in a round trajectory without conjugate trajectory as illustrated in Fig. 1.

Example: Lets figure out $\alpha = 1.2$ and $\alpha = 0.8$ root equivalence of the first order stable LTI system $T(s) = \frac{1}{s+2}$.

By considering $M = -2$ and $\theta = \pi$ radian due to the root $v = -2 = 2e^{j\pi}$, the $\alpha = 1.2$ order root equivalent system of $T(s)$ is obtained according to equation (3) as,

$$T_{1.2}(s) = \frac{1}{s^{1.2} - (-2)^{1.2}} = \frac{1}{s^{1.2} + 1.8586 + j1.3504} \quad (4)$$

Here, the complex root emerges as $v^{1.2} = (-2)^{1.2} = (2e^{j\pi})^{1.2} = 2^{1.2} e^{j1.2\pi} = -1.8586 - j1.3504$. The magnitude of root is changed from 2 to 2.2974, ($2 \rightarrow 2^{1.2}$), and the angle of root changes from π to 1.2π radian.

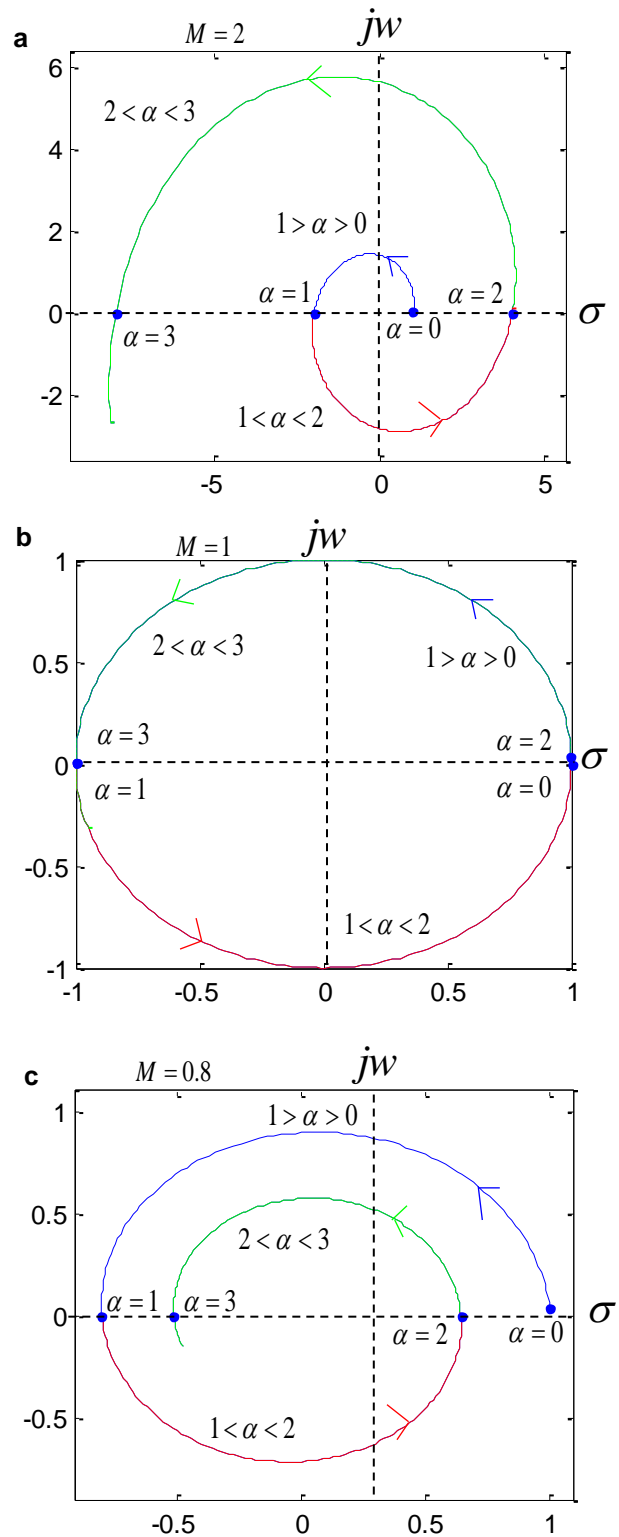


Fig. 2. The root locus shifting in the range of $0 < \alpha < 3.1$ for root magnitudes; $M = 2$ in (a), $M = 1$ in (b) and $M = 0.8$ in (c)

Both magnitude and angle of root increase because of $\alpha > 1$ and $M > 1$. Fig. 3 confirms this effect, graphically.

For $\alpha = 0.8$, the root equivalency of $T(s)$ is obtained as follows,

$$T_{0.8}(s) = \frac{1}{s^{0.8} - (-2)^{0.8}} = \frac{1}{s^{0.8} + 1.4086 - j1.0234} \quad (5)$$

Here, $v^{0.8} = (-2)^{0.8} = (2e^{j\pi})^{0.8} = 2^{0.8} e^{j0.8\pi} = -1.4086 + j1.0234$. The magnitude of root is changed from 2 to 1.7411 ($2 \rightarrow 2^{0.8}$) and the angle of root changes from π to 0.8π radian. For $\alpha < 1$, magnitude and angle of the root decrease. Fig. 3 shows this effect, graphically.

Fig. 3 illustrates possible root equivalency trajectories of the first order systems $T(s) = 1/(s + 2)$ and $T(s) = 1/(s + 0.5)$ in the range of $0 < \alpha < 2$. The root trajectories in the figure demonstrate that the system model has single complex root without a complex conjugate. Practically, it is difficult to implement transfer functions containing complex roots without its conjugate pairs. One see that, for $\alpha = 0$, all trajectories converge to one. For $\alpha > 0$, type of root equivalency trajectory of the system (narrowing, circling or expanding trajectories) depends on the magnitude of the root (M).

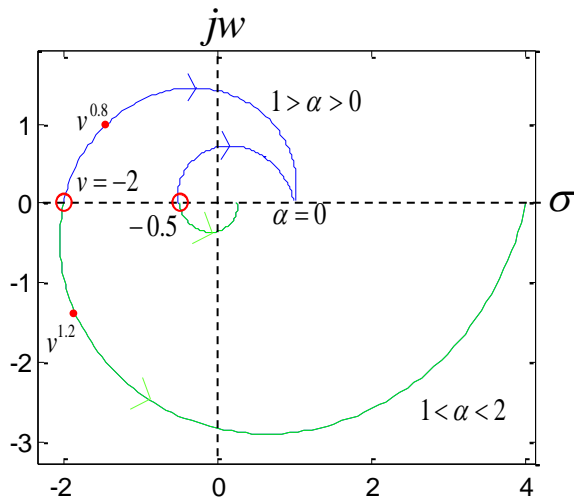


Fig. 3. The root locus shifting of stable first order LTI systems in the range of $0 < \alpha < 2$. The outer trajectory is for $T(s) = 1/(s + 2)$ and the inner trajectory is for $T(s) = 1/(s + 0.5)$

C. Root addition for complex root conjugating of commensurate order equivalence of first order LTI Systems

System designers may question whether it is possible to derive a real coefficient commensurate order system from the first order LTI systems by using α -order root equivalency so that realization of complex coefficient systems is a complicated problem for practice. Previously, to carry out implementation of complex-order systems, several studies have addressed the implementation problems of complex coefficient transfer functions. To obtain real valued outputs from complex-order systems, conjugated-order system concept were introduced [34,35].

In this section, we benefit from a similar perspective, which involves complex conjugate root addition to system model in order to transform a complex coefficient root equivalent system into a real coefficient commensurate order systems. This method increases root counts of characteristic equation from one to two because of $\Delta_\alpha(s) = (s^\alpha - v^\alpha)(s^\alpha - v^{\alpha*})$, where $v^{\alpha*} = M^\alpha e^{-j\alpha\theta}$ represents the complex conjugate pair of $v^\alpha = M^\alpha e^{j\alpha\theta}$. Thus, this additional conjugate root allows real valued outputs from the system model. With the complex root conjugating, equation (3) expand to the model of real coefficient α commensurate order system as follows.

$$T_\alpha(s) = \frac{K}{(s^\alpha - M^\alpha \cos(\alpha\theta) - jM^\alpha \sin(\alpha\theta))(s^\alpha - M^\alpha \cos(\alpha\theta) + jM^\alpha \sin(\alpha\theta))} \quad (6)$$

When this equation is arranged, one obtains the real coefficient commensurate order root equivalent system with complex conjugate as follows,

$$T_\alpha(s) = \frac{K}{s^{2\alpha} - 2M^\alpha \cos(\alpha\theta)s^\alpha + M^{2\alpha}} \quad (7)$$

Here, the root angle θ can take values of $\{0, \pi\}$ so that a real coefficient first order LTI system $T(s)$ has a characteristic root only on the real axis. If $T(s)$ is a stable system, the root resides on the left half plane and $\theta = \pi$. The real coefficient $T_\alpha(s)$ function expresses a special class for the second order commensurate order system that is based on root equivalency of first order LTI systems. Previously, some analyses addressing the stability of second order conjugate systems were addressed in detail by Radwan et al [23].

Let's investigate effects of α order on the system behavior. A discussion on system behavior depending on system pole location was previously given by Monje et al. [32]. We performed simulations and observed the following remarks for root equivalencies of the first order stable LTI systems given by equation (7):

- (i) For $\alpha = 0.5$, it yields the original first order LTI system that is expressed by equation (1).
- (ii) In the case of $\alpha < 0.5$, simulation results indicate that the commensurate order root equivalent system with complex conjugate can exhibit low rise time step response.
- (iii) In the case of $0.5 < \alpha < 4/3$, simulation results showed that the commensurate order root equivalent system with complex conjugate yields a slower step response than the original first order LTI system.
- (iv) In the case of $\alpha = 4/3 \cong 1.33\dots$, the root equivalent system exhibits oscillating behavior.
- (v) In the case of $\alpha > 4/3$, the root equivalent system is unstable.

The value of $\alpha = 4/3$ defines an upper boundary for asymptotical stability of commensurate order root equivalent systems that are expressed in the form of equation (7). In order

to obtain an asymptotically stable commensurate order system, a sufficient condition of $0 < \alpha < 4/3$ should be satisfied in system design. (See Property 1 in Appendix for the extraction of $\alpha = 4/3$ boundary condition). This property allows a straightforward solution for testing of the stability of a special class of commensurate order systems expressed in the form of equation (7). A stability check procedure for a given commensurate order system complying with the equation (7) can be summarized as follows:

Step 1: By considering characteristic polynomial in the form of $\Delta_\alpha(s) = s^{2\alpha} + a_1 s^\alpha + a_0$, find commensurate order α by considering orders as $k\alpha$ for $k = 0, 1, 2$.

Step 2: By considering the term a_0 , calculate M by $M = a_0^{1/(2\alpha)}$.

Step 3: If $2M^\alpha \cos(\alpha\theta) = -a_1$ for $\theta = \pi$, the system is a root equivalency of a first order stable LTI system. In this case, commensurate order root equivalent system is said to be stable for $\alpha < 4/3$ in accordance with the remark (iii).

Since the root angle is zero ($\theta = 0$ rad), the α -order root equivalent systems of the first order unstable LTI systems can be expressed $T_\alpha(s) = \frac{K}{s^\alpha - M^\alpha e^{j\theta\alpha}} = \frac{K}{s^\alpha - M^\alpha}$. This states that α -order root equivalency of the unstable first order LTI systems is always real coefficient and unstable for $\forall \alpha \in \mathbb{R}$. (See Proper 2 in Appendix)

D. An extension of root equivalency analysis for the second order LTI systems

In this section, we extent our investigation for root equivalence of the second order LTI systems. The transfer function of the second order LTI system can be written in general form as,

$$T(s) = \frac{K}{(s - v_1)(s - v_2)} \quad (8)$$

The root equivalent characteristic polynomial of the equation (8) is written as $\Delta_\alpha(s) = (s^\alpha - v_1^\alpha)(s^\alpha - v_2^\alpha)$. The transfer function of α -order root equivalent commensurate system with two roots can be written in the form of,

$$T(s) = \frac{K}{(s^\alpha - v_1^\alpha)(s^\alpha - v_2^\alpha)} \quad (9)$$

By applying root equivalent transformation to the each root as $s^\alpha = v_1^\alpha = M_1^\alpha e^{j\alpha\theta_1}$ and $s^\alpha = v_2^\alpha = M_2^\alpha e^{j\alpha\theta_2}$, one can rearrange the α -order root equivalent commensurate system as,

$$T_\alpha(s) = \frac{K}{(s^\alpha - M_1^\alpha e^{j\alpha\theta_1})(s^\alpha - M_2^\alpha e^{j\alpha\theta_2})} \quad (10)$$

When the roots of second order system are $v_2^\alpha = v_1^{\alpha*}$, it yields the real coefficient characteristic polynomial. So, it can be possible to find out a α value that makes v_1^α and v_2^α complex

conjugate pairs. One can obtain the real coefficient characteristic polynomial, when conditions of $\alpha\theta_1 = -\alpha\theta_2$ and $M_1 \sin(\alpha\theta_1) = M_2 \sin(\alpha\theta_2)$ are satisfied. A solution to satisfy these two conditions can be written as $\alpha\theta_1 = -\alpha\theta_2 = \eta\pi$, $\eta \in \mathbb{Z}^+$. Here, the first α value making equation (10) a real coefficient system model can be found as $\alpha = \pi/\theta_1$ for $\eta = 1$. Accordingly, real coefficient commensurate order root equivalent system can be expressed for $\alpha = \pi/\theta_1$ and $\theta_1 = -\theta_2$ in the form of,

$$T_\alpha(s) = \frac{K}{s^{2\alpha} - (M_1^\alpha \cos(\alpha\theta_1) + M_2^\alpha \cos(\alpha\theta_2))s^\alpha + M_1^\alpha M_2^\alpha} \quad (11)$$

Example: Let's find α values that makes $T_1(s) = \frac{1}{s^2 + 4s + 3}$ and $T_2(s) = \frac{1}{s^2 + 0.5s + 1}$ a real coefficient commensurate order root equivalent systems.

For $T_1(s)$, roots are -1 and -3, which is not complex conjugate roots and $\theta_1 = \theta_2 = \pi$ radian. So, $\alpha = \pi/\theta_1 = \pi/\pi = 1$. There is not any real coefficient commensurate order root equivalent system. One should add new conjugate roots in a similar way applied for the first order LTI systems.

For $T_2(s)$, roots are complex conjugate pairs as $-0.2500 \pm 0.9682j$. In this case, $\theta_1 = 1.8235$ radian and $\alpha = \pi/1.8235 = 1.7229$. When it is used in equation (11), the real coefficient commensurate order root equivalent systems is found as,

$$T_{1.7229}(s) = \frac{1}{s^{3.4457} + 2s^{1.7229} + 1} \quad (12)$$

An important remark to notice when the second order LTI system is stable, the real coefficient commensurate order system with $\alpha = \pi/\theta_1$ is also stable. (See Property 3 in Appendix) This allows checking the stability of the commensurate order systems in the form of equation (11) by using root equivalence of second order systems as follows,

Step 1: By considering characteristic polynomial in the form of $\Delta_\alpha(s) = s^{2\alpha} + a_1 s^\alpha + a_0$, find α by considering the commensurate order in the form of $k\alpha$ for $k = 0, 1, 2$.

Step 2: Assume $v_2^\alpha = v_1^{\alpha*}$ for real coefficient characteristic polynomial. Therefore, suppose $M_1^\alpha = M_2^\alpha = M^\alpha$, $\theta_1 = \pi/\alpha$ and $\theta_2 = -\theta_1$.

Step 3: By considering the term a_0 , calculate M by $M = a_0^{1/(2\alpha)}$.

Step 4: If $2M^\alpha \cos(\alpha\theta_1) = -a_1$, the system is a root equivalent of second order LTI system, and if $\frac{\pi}{2} < \theta_1 < \frac{3\pi}{2}$, the second

order LTI system is stable and therefore the commensurate order system are also stable.

III. ILLUSTRATIVE EXAMPLES

Example 1: Let's find real coefficient commensurate order root equivalent of the first order stable LTI system $T(s) = \frac{1}{s+2}$ by applying complex root conjugation addition approach for $\alpha = 1.2$ and $\alpha = 0.8$.

If the characteristic root of system is considered in the complex form as $s = -2 = 2e^{j\pi} = Me^{j\theta}$, one obtains $M = 2$ and $\theta = \pi$. For $\alpha = 1.2$, by using equation (7), one obtains the real coefficient commensurate order root equivalent systems of $T(s)$ as,

$$T_{1.2}(s) = \frac{1}{s^{2.4} + 3.7173s^{1.2} + 5.278} \tag{13}$$

and, similarly, for $\alpha = 0.8$, one obtains the real coefficient commensurate order root equivalent systems of $T(s)$ as,

$$T_{0.8}(s) = \frac{1}{s^{1.6} + 2.8172s^{0.8} + 3.0314} \tag{14}$$

order root equivalent systems derived from the first order stable LTI system $T(s) = \frac{1}{s+3}$ for various α .

When the root of characteristic polynomial of $T(s)$ is considered in complex form, $s = -3 = 3e^{j\pi} = Me^{j\theta}$, one obtains $M = 3$ and $\theta = \pi$. By applying equation (7), we can obtain complex conjugated commensurate order root equivalent systems of $T(s) = \frac{1}{s+3}$ as listed in Table 2. Step responses of these systems are shown in Fig. 4. The step responses in the figure confirm system behavior corresponding to values of α , which are explained in the section 2.C.

TABLE II. COMPLEX CONJUGATED COMMENSURATE ORDER ROOT EQUIVALENT SYSTEMS FOR VARIOUS α

α	Commensurate Order Root Equivalent Systems	Remarkd Item
0.3	$T_{0.3}(s) = \frac{1}{s^{0.6} - 1.6354s^{0.3} + 1.9332}$	(ii) $\alpha < 0.5$
0.5	$T_{0.5}(s) = T(s) = \frac{1}{s+3}$	(i) $\alpha = 0.5$
0.9	$T_{0.9}(s) = \frac{1}{s^{1.8} + 5.1126s^{0.9} + 7.2247}$	(iii) $0.5 < \alpha < 4/3$
1.333	$T_{1.3509}(s) = \frac{1}{s^{2.7018} + 4.3267s^{1.3509} + 18.7208}$	(iv) $\alpha = 4/3$
1.4	$T_{0.9}(s) = \frac{1}{s^{2.8} + 2.8773s^{1.4} + 21.674}$	(v) $\alpha > 4/3$

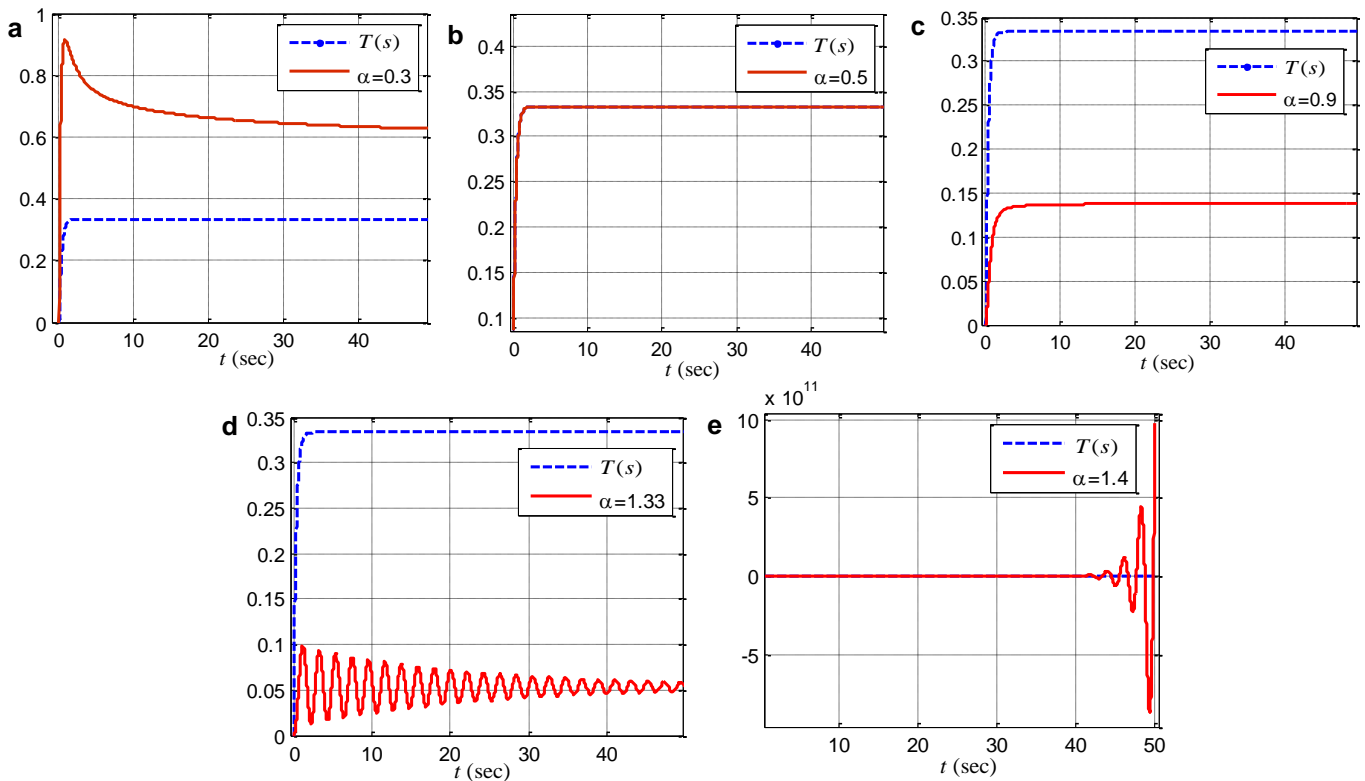


Fig. 4. Step responses obtained for commensurate order root equivalent systems, which are listed in Table 2

Example 2: Lets investigate behavior of complex conjugated commensurate

We observed from step response simulation results that for $\alpha < 0.5$, the step response of commensurate order root

equivalent systems is faster than the first order integer order LTI system. For $\alpha > 0.5$, the step response of commensurate order root equivalent system is slower than the first order integer order LTI system. Another noteworthy point should be emphasized that, $\alpha \cong 1.33..$ yields oscillations due to root placement on the stability boundary. More comprehensive discussions on sinusoidal oscillation condition of fractional and integer order systems was given in [22,23].

Example 3: Let us check whether the commensurate order LTI system $G(s) = \frac{1}{s^{2.2} + 11.171s^{1.1} + 34.4932}$ is stable?

Lets apply the steps of stability check procedure given in previous section.

Step 1: Due to terms of $s^{2.2}$, $s^{1.1}$ and s^0 , one finds $\alpha = 1.1$.

Step 2: Considering $M = a_0^{1/(2\alpha)}$, then, one calculate $M = (34.4932)^{1/2.2} \cong 5$.

Step 3: Considering $2M^\alpha \cos(\alpha\theta) = a_1$ for $\theta = \pi$ radian, one calculates $2 \cdot 5^{1.1} \cos(1.1\pi) = -11.171 = -a_1$. This confirms that $G(s)$ is the root equivalency of the stable LTI $1/(s+5)$.

Step 4: In this case, since $\alpha = 1.1 < 4/3$, the system $G(s)$ is stable.

In order to validate this result, we demonstrate the step response of $G(s)$ in Fig. 5(a) and root locus in the in the first Riemann sheet in Fig. 5(b) to apply Radwan stability test procedure [23]. Radwan stability test procedure is essentially based on Matignon’s theorem [21]. This procedure applies $s = u^m$ transformation to characteristic polynomial and investigates root angle of expanded degree integer order polynomial on the first Riemann sheet. After applying $s = u^{10}$ to characteristic equation $\Delta_{1.1}(s) = s^{2.2} + 11.171 s^{1.1} + 34.49$, one obtains $\Delta_{1.1}(u^{10}) = u^{22} + 11.17u^{11} + 34.49$. If any root angle (ϕ) of satisfies $-\pi/20 \leq \phi \leq \pi/20$ in the first Riemann sheet, Radwan procedure suggests us that the system is unstable. Fig. 5(b) shows root locus of $\Delta_{1.1}(u^{10})$ and it confirms stability of the system so that roots are out of instability region defined by $-\pi/m \leq \phi \leq \pi/m$. The roots are indicated by blue stars in Fig 5(b). In some cases, this test procedure introduces high computational complexity. For instance, if $\alpha = 1.111$, one need to apply $s = u^{1000}$ and calculate root angles of the polynomial $\Delta_{1.111}(u^{1000})$. Accordingly, amount of digits in fractional part increases computational complexity, significantly. One of the advantages of root equivalency analyses may appear in such cases. If commensurate order LTI system is a member of root equivalency class, it can significantly reduce computational complexity in stability analyses.

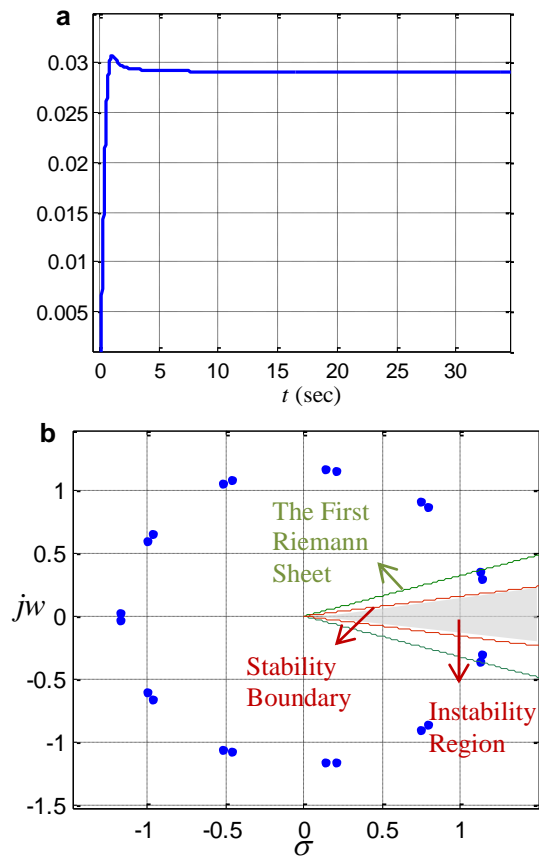


Fig. 5. (a) Step response of $G(s)$ and (b) the root locus showing that $G(s)$ system is stable according to Radwan stability test procedure

Example 4: Lets design an oscillating response from the root equivalency family of the commensurate order system that was analyzed in the previous example.

In order to provide oscillation of $G(s) = \frac{1}{s^{2.2} + 11.171 s^{1.1} + 34.4932}$, which is a member of the root equivalency class of the function $1/(s+5)$ for $M = 5$ and $\theta = \pi$ radian as shown in previous example. Here, one configures $\alpha = 4/3 = 1.33...$ for oscillating behavior. By using equation (7), one obtains transfer function of oscillating commensurate order root equivalent system as,

$$G(s) = \frac{1}{s^{2.6812} + 8.3063s^{1.3406} + 74.8295} \quad (15)$$

We used step function proposed in [33] to numerically calculate step responses in this study. Fig. 6 shows oscillating behavior of the system. As $\alpha = 4/3 = 1.33...$ is an infinite decimal number, it cannot be exactly implemented and calculated in digital systems. Therefore, the finite decimal implementation of $\alpha = 1.33...$ can result in an unbalanced oscillation as shown in Fig. 6.

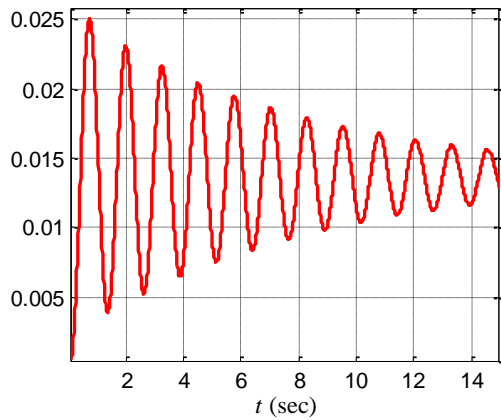


Fig. 6. Step response showing oscillating system behavior

Example 5: Let's find the x coefficient that makes $G(s) = \frac{1}{s^{1.82} + xs^{0.91} + 9.777}$ function a root equivalence class of a first order LTI system.

It is apparent from $s^{1.82}$ and $s^{0.91}$ that the α order of the system is 0.91 and we calculate the magnitude as $M = (9.777)^{1/1.82} \cong 3.5$ by considering $M^{2\alpha} = 9.777$ according to Equation (7). In this case, the function $G(s)$ can be the root equivalence of the first order LTI system $1/(s + 3.5)$. We can calculate $x = -2M^\alpha \cos(\alpha\theta) = -2(3.5)^{0.91} \cos(0.91\pi) \cong 6.0053$ for $\alpha = 0.91$ and $\theta = \pi$.

Example 6: Let's check stability of $G_1(s) = \frac{1}{s^{4.5508} + 18.3022s^{2.2754} + 83.7423}$ and $G_2(s) = \frac{1}{s^{3.0884} + 6.9296s^{1.5442} + 12.0047}$ by using root equivalent class of second order LTI systems.

By applying stability check procedure for $G_1(s)$,
Step 1: Due to terms $s^{4.5508}$, $s^{2.2754}$ and s^0 , one finds $\alpha = 2.2754$.

Step 2: The root angle is $\theta_1 = \pi/\alpha = \pi/2.2754 = 1.3807$
Step 3: Considering $M = a_0^{1/(2\alpha)}$, then, one calculate $M = (83.7423)^{1/2.2754} \cong 2.6458$.

Step 4: Considering $2M^\alpha \cos(\alpha\theta_1) = -a_1$, one calculates $2 \cdot 2.6458^{2.2754} \cos(2.2754 \cdot 1.3807) = -18.3022 = -a_1$. This confirms that the system is root equivalency of the second order stable LTI system. However, the root angle $\theta_1 = 1.3807$ does not satisfy the condition $\frac{\pi}{2} < \theta_1 < \frac{3\pi}{2}$, $G_1(s)$ system is unstable system.

By applying stability check procedure for $G_2(s)$,
Step 1: Due to terms $s^{3.0884}$, $s^{1.5442}$ and s^0 , one finds $\alpha = 1.5442$.

Step 2: The root angle is $\theta_1 = \pi/2.2754 = 2.0344$
Step 3: Considering $M = a_0^{1/(2\alpha)}$, then, one calculate $M = (12.0047)^{1/(1.5442)} \cong 2.2361$.
Step 4: Considering $2M^\alpha \cos(\alpha\theta_1) = -a_1$, one calculates $2 \cdot 2.2361^{1.5442} \cos(1.5442 \cdot 2.0344) = -6.9296 = -a_1$. This confirms that the system is a root equivalency of the second order stable LTI system. Since, the root angle $\theta_1 = 2.0344$ does satisfy the condition $\frac{\pi}{2} < \theta_1 < \frac{3\pi}{2}$, $G_2(s)$ system is stable.

Fig. 7 demonstrates step responses of $G_1(s)$ and $G_2(s)$ functions, which confirm results of the stability analyses. Fig. 7(a) indicates step response of an unstable system and Fig. 7(b) indicates the step response of a stable system.

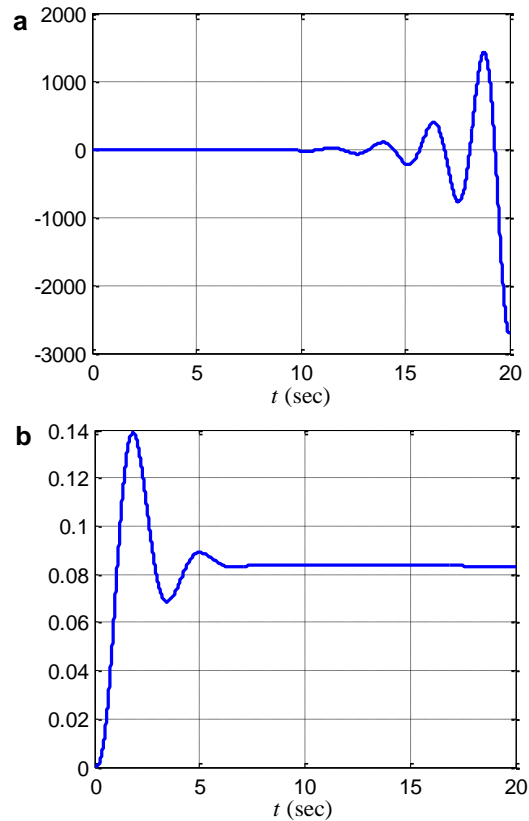


Fig. 7. Step responses of $G_1(s)$ in (a) and $G_2(s)$ in (b)

IV. CONCLUSIONS

This study shows that one can establish analytical relations between fractional order LTI systems and integer order LTI systems via characteristic root equivalency. These relations can facilitate design and analysis efforts of commensurate order systems on bases of root equivalency of integer order LTI systems and help comprehension of effects of fractional orders on the system behavior.

In summary, α -order commensurate root equivalence classes of the first and second order stable LTI systems are investigated in the paper. The first order LTI system produces complex coefficient commensurate order root equivalent

systems with single root. To transform them to a real coefficient commensurate order root equivalent systems, root conjugation by a complex root addition was used. Then, we extent our investigation to root equivalency of second order LTI systems. We derived a sufficient condition that transforms a second order LTI system to a real coefficient root equivalent commensurate order LTI system without any conjugate root addition. Numerical examples were presented to demonstrate straightforward analytical solutions for stability analysis and design problems for commensurate order systems. Some important remarks can be summarized as follows:

(i) The characteristic root equivalency transformation $s^\alpha = v^\alpha$ for $\alpha \in \mathcal{R}$ results in shifting of roots on the trajectory in complex plane according to nonlinear magnitude scaling (M^α) and linear angle scaling ($\alpha\theta$). These properties of this trajectories can be used to establish analytical relations between fractional order systems and integer order LTI systems. This can provide simplifications in design and analyses of this class of fractional order systems.

(ii) First order LTI system yields real coefficient root equivalent commensurate order systems by addition of a complex conjugate root. This class of root equivalent commensurate order systems of first order stable LTI systems establishes a constant stability boundary at $\alpha = 4/3$, which yields oscillating systems. For $0 < \alpha < 4/3$, the system is stable [23]. In the stable region, we observed that effect of order α on time responses of this class exhibit consistently.

(iii) Second order LTI system can yield real coefficient root equivalent commensurate order systems at $\alpha = \pi/\theta_1$ without addition of any complex conjugate root. If the second order LTI system is stable, the real coefficient root equivalent commensurate order system is also stable.

Computational complexity of stability analyses for this type commensurate order systems can be reduced, significantly. In future studies, fractional order root equivalency relations can be extended higher order LTI systems.

V. APPENDIX

Properties for the first order LTI systems:

Property 1 (Stability Boundary at $\alpha = 4/3$) : The real coefficient commensurate order root equivalent systems of the stable first order LTI systems, which is expressed in the form of equation (7), is (i) stable for $0 < \alpha < 4/3$, (ii) oscillating for $\alpha = 4/3$ and (iii) unstable for $\alpha > 4/3$.

Proof:

Let consider a stable first order system. This infers the condition of $\theta = \pi$. Now, we can treat separately two cases of $\alpha > 0$, which are $0 < \alpha \leq 1$ and $\alpha > 1$. According to value of α , the stability region of commensurate order systems change according to the root angle ranges $-\pi < \alpha\theta < -\alpha\frac{\pi}{2}$ and

$$\alpha\frac{\pi}{2} < \alpha\theta \leq \pi$$

as seen in Fig. 8 [1].

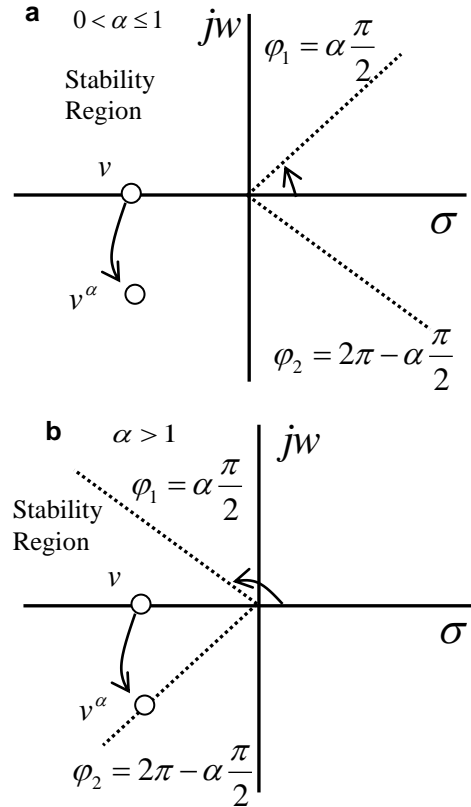


Fig. 8. Root shifting analysis for the first order stable LTI systems in the stability region for $0 < \alpha \leq 1$ in (a) and $\alpha > 1$ in (b) [1]

(i) In the case of $0 < \alpha \leq 1$, lower stability boundary $\phi_1 = \alpha\frac{\pi}{2}$ moves toward zero angle and this expand stability region as shown Fig. 8(a). Due to $\alpha\theta = \alpha\pi$ for commensurate order root equivalency of a first order LTI system, the condition $\alpha\theta > \alpha\frac{\pi}{2}$ is always satisfied for every $0 < \alpha \leq 1$ and therefore the roots of equivalent systems always stay in the stability region.

(ii) In the case of $\alpha > 1$, due to narrowing stability region as in Fig. 8(b), the root of the first order equivalent system comes closer to the boundary $\phi_2 = 2\pi - \alpha\frac{\pi}{2}$. The α -order, which shifts the root of the first order LTI system on the boundary line ϕ_2 , results in sinusoidal oscillation of commensurate order systems. So, to figure out α -order to shift the root $v^\alpha = M^\alpha e^{j\alpha\pi}$ to the stability boundary $\phi_2 = 2\pi - \alpha\frac{\pi}{2}$, one can solve the equation $\alpha\theta = \alpha\pi = 2\pi - \alpha\frac{\pi}{2}$ and calculate the stability boundary of $\alpha = 4/3$. Here, $\alpha = 4/3$ results in sinusoidal oscillation of commensurate order root equivalent system of the first order LTI systems. For unstable

commensurate order root equivalent systems, the root should move beyond the stability boundary. So, $\alpha\theta = \alpha\pi > 2\pi - \alpha\frac{\pi}{2}$

For $0 < \alpha < 4/3$, the system response stable because of placement of root inside the stability region. For $\alpha = 4/3$, the system oscillates because of placement of root on the stability boundary, and for $\alpha > 4/3$, the system becomes unstable because of placement of root outside the stability region.

Property 2: The real coefficient commensurate order root equivalent systems of the unstable first order LTI systems is unstable for $\forall \alpha \in R$.

Proof:

For the first order unstable systems, one can take the root angle $\theta = 0$. Fig. 9 clearly shows that the root angle of α -order equivalent root is $\alpha\theta = \alpha \cdot 0 = 0$ for $\alpha \in R$ and therefore it always stays out of the stability region that expressed the angle range $-\pi < \alpha\theta < -\alpha\frac{\pi}{2}$ and $\alpha\frac{\pi}{2} < \alpha\theta \leq \pi$.

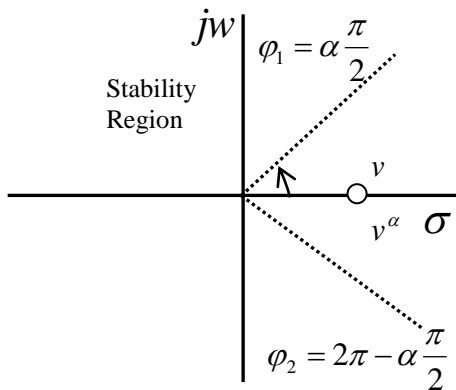


Fig. 9. Root shifting analysis for the first order unstable LTI systems [1]

Properties for the second order LTI systems:

Property 3 (Stability Boundary $\theta_1 = \pi/2$) if integer order LTI system is stable, the real coefficient root equivalent commensurate order system in the form of equation (11) for $\alpha = \pi/\theta_1$ is stable.

Proof:

Let assume a stable second order system is given. This infers the condition of $\frac{\pi}{2} < \theta_1 < \frac{3\pi}{2}$. Now, let's treat two cases of α , which are $0 < \alpha \leq 1$ and $\alpha > 1$.

(i) In the case of $0 < \alpha \leq 1$, roots shifts towards the stability boundary $\varphi_1 = \alpha\frac{\pi}{2}$. If the second order system is stable, the real coefficient commensurate order root equivalent systems obtained for $\alpha = \pi/\theta_1$ are always stable because the closest

root is always stays in stability region because $\alpha\theta_1 = \alpha\frac{\pi}{\alpha} = \pi$ and therefore $\alpha\frac{\pi}{2} < \alpha\theta_1$ is always satisfied.

(ii) In the case of $\alpha > 1$, the complex root can move toward the upper stability boundary $\varphi_2 = 2\pi - \alpha\frac{\pi}{2}$. When it place on this boundary, the α order commensurate order system oscillates.

If $\alpha\theta_1 = 2\pi - \alpha\frac{\pi}{2}$ equation is solved for real coefficient root equivalent with $\alpha = \pi/\theta_1$, one obtains $\theta_1 = \pi/2$. If root angle θ_1 is equal or greater than $\frac{\pi}{2}$, the commensurate order system are stable. As a consequence, if integer order LTI system is stable, the root equivalent commensurate order system with $\alpha = \pi/\theta_1$ is also stable.

REFERENCES

- [1] I. Petras, "Stability of Fractional-Order Systems with Rational Orders: A Survey", *Fractional Calculus And Applied Analysis*, Vol.12, No.3, 2009, pp.269-298.
- [2] B. West, M. Bologna, P. Grigolini, "Physics of Fractal Operators", Springer, New York, 2003.
- [3] A. Oustaloup, "La Derivation Non Entiere: Theorie, Synthese et Applications", Hermes, Paris, 1995.
- [4] I. Podlubny, "Fractional Differential Equations", Academic Press, San Diego, 1999.
- [5] Y.Q. Chen, K.L. Moore, "Analytical stability bound for a class of delayed fractional-order dynamic systems", *Nonlinear Dynamics*, Vol.29, 2002, pp.191-200.
- [6] F.J.V. Parada, J.A.O. Tapia, J.A. Ramirez, "Erective medium equations for fractional Ficks law in porous media", *Physica*, Vol.373, 2007, pp. 339-353.
- [7] J.A.O. Tapia, F.J.V. Parada, J.A. Ramirez, "A fractional-order Darcys law", *Physica* Vol.374, 2007, pp.1-14.
- [8] P.J. Torvik, R.L. Bagley, "On the appearance of the Fractional Derivative in the Behavior of real materials", *Transactions of the ASME*, Vol.51, 1984, pp.294-298.
- [9] I.S. Jesus, J.A.T. Machado, "Fractional control of heat diffusion systems", *Nonlinear Dynamics*, Vol.54, No.3, 2008, pp.263-282.
- [10] P. Arena, R. Caponetto, L. Fortuna, D. Porto, "Nonlinear Noninteger Order Circuits and Systems - An Introduction", World Scientific, Singapore, 2000.
- [11] A. Charef, "Modeling and analog realization of the fundamental linear fractional order differential equation", *Nonlinear Dynamics*, Vol.46, 2006, pp.195-210.
- [12] M. Nakagava, K. Sorimachi, "Basic characteristics of a fractance device", *IEICE Trans. Fundamentals*, E75 - A, 1992, pp.1814-1818.
- [13] M.F. Silva, J.A.T. Machado, A.M. Lopes, "Fractional order control of a hexapod robot", *Nonlinear Dynamics*, Vol.38, 2004, pp.417-433.
- [14] M.S. Tavazoei, M. Haeri, "Chaotic attractors in incommensurate fractional order systems", *Physica D*, Vol. 237, 2008, pp.2628-2637.
- [15] I. Podlubny, "Fractional-order systems and PID μ -controllers", *IEEE Trans. on Automatic Control*, Vol.44, 1999, pp.208-213.
- [16] H.F. Raynaud, A. Zerganoh, "State-space representation for fractional order controllers", *Automatica*, Vol.36, No.7, 2000, pp.1017-1021.
- [17] B.M. Vinagre, I. Petras, P. Merchan, L. Dorcak, "Two digital realizations of fractional controllers: Application to temperature control of a solid", In: Proc. of the ECC'01, Porto, Portugal, 2001, pp. 1764-1767.
- [18] G. Madan, "Modern Control System Theory", New Age International, 1993, pp.322-324.
- [19] H.S. Ahn, Y.Q. Chen, I. Podlubny, "Robust stability test of a class of linear time-invariant interval fractional-order system using Lyapunov inequality", *Appl. Math. Comput.*, Vol.187, 2007, pp.27-34.

- [20] R. Caponetto, G. Dongola, L. Fortuna, I. Petras, "Fractional Order Systems Modeling and Control Applications", World Scientific Series on Nonlinear Science A series Vol. 72, World Scientific Publishing Co. Pte. Ltd, 2010.
- [21] D. Matignon, "Stability result on fractional differential equations with applications to control processing", in Proc. IMACS-SMC Proceedings, Lille, France, 1996, pp 963-968.
- [22] A.G. Radwan, A.S. Elwakil, A.M. Soliman, "Fractional-Order Sinusoidal Oscillators: Design Procedure and Practical Examples", IEEE Transaction On Circuits and System, Vol.5, 2008, pp.2051-2063.
- [23] A.G. Radwan, A.M. Soliman, A.S. Elwakil, A. Sedeek, "On the stability of linear systems with fractional-order elements", Chaos Solitons & Fractals, Vol.40, No.5, 2009, pp.2317-2328.
- [24] B.B. Alagoz, "Hurwitz stability analysis of fractional order LTI systems according to principal characteristic equations", ISA Transactions, 2017, <https://doi.org/10.1016/j.isatra.2017.06.005>.
- [25] M. Buslowicz, "Stability Analysis of Linear Continuous-time Fractional Systems Of Commensurate Order", Journal of Automation, Mobile Robotics & Intelligent Systems, Vol.3, 2009, pp.12-17.
- [26] M., Buslowicz Frequency domain method for stability analysis of linear continuous-time fractional systems. In: K. Malinowski, L. Rutkowski (Eds.): Academic Publishing House EXIT: Warsaw 2008, pp.83-92.
- [27] W.C. Wright, T.W. Kerlin, "An efficient computer oriented method for stability analysis of large multivariable systems", Journal of Fluids Engineering, Vol.92, 1970, pp.279-286.
- [28] M.S. Tavazoei, M. Haeri, "A note on the stability of fractional order systems", Mathematics and Computers in Simulation, Vol.79, No.5, 2009, pp.1566-1576.
- [29] Y.D. Ma, J.G. Lu, W.D. Chen, Y.Q. Chen, "Robust stability bounds of uncertain fractional-order systems", Fractional Calculus and Applied, Vol.17, No.1, 2014, pp.136-153.
- [30] J.G. Lu, Y.Q. Chen, "Robust stability and stabilization of fractional order interval systems with the fractional order α : The $0 < \alpha < 1$ case", IEEE Trans. Autom. Control, Vol.55, No.1, 2010, pp.152-158.
- [31] C. Li, J.C. Wang, "Robust stability and stabilization of fractional order interval systems with coupling relationships: The $0 < \alpha < 1$ case", J. of the Franklin Institute, Vol.349, No.7, 2012, pp.2406-2419.
- [32] C.A. Monje, Y.Q. Chen, B.M. Vinagre, D. Xue, V. Feliu-Battle, "Fractional-order Systems and Controls Fundamentals and Applications", Springer, 2010.
- [33] D. Xue, Y.Q. Chen, D.P. Atherton, "Linear Feedback Control Analysis and Design with MATLAB", Society for Industrial and Applied Mathematics, Philadelphia, 2007.
- [34] R.S. Barbosa, J.A.T. Machado, M.F. Silva, "Discretization of complex-order algorithms for control applications", Journal of Vibration and Control, Vol.14, 2008, pp.1349-1361.
- [35] T.T. Hartley, C.F. Lorenzo, J.L. Adams, "Conjugated-order differintegrals", in Proceedings of the ASME International Design Engineering Technical Conferences and Computers and Information in Engineering Conference, Long Beach, CA, 2005, DETC2005-84951.

BIOGRAPHIES



BARIS BAYKANT ALAGOZ received bachelor degree in Istanbul Technical University, Department of Electronics and Communication Engineering in 1998, M.Sc. and Ph.D. degrees in Inonu University, Department of Electrical-Electronics Engineering in 2011 and 2015. His research interests include modeling and simulation of physical systems, control systems, smart grid. He is working at Computer Engineering Department in Inonu University.

Emg Signal Classification Using Fuzzy Logic

O. Ülkir, G. Gökmen and E. Kaplanoğlu

Abstract— Electromyography (EMG) signals are an important technique in the control applications of prosthetic hand. These signals, which are measured from the skin surface, are used to perform movements such as wrist flexion / extension, forearm supination / pronation and hand opening / closing of prosthetic devices. In this study, root mean square, waveform length and kurtosis methods were applied to extracted EMG signals from flexor carpi radialis and extensor carpi radialis muscles by using two channel surface electrodes. A fuzzy logic based classification method has been applied to classify the extracted signal features. With this method, classification for different gripping movements has been successfully accomplished.


Index Terms—Surface EMG, fuzzy logic, feature extraction, EMG classification.


I. INTRODUCTION


ELECTROMYOGRAM (EMG) is defined as muscle contraction resulting because of bioelectric signals. The source of those bioelectric signals is various electrochemical processes occurring in the body. Data logging of electrical signals in the muscles, provides important information in the diagnosis of abnormalities in both motor system and muscles [1].

EMG signals can be obtained by placing surface electrodes on the muscles or needle electrodes into the muscle tissue. Although differences between the needle and surface electrodes are not of a significant degree, the surface electrodes are preferred over the needle electrode. The most important reason for this is to be a safe and non-invasive measurement method [2].

EMG signals are used in medicine for the diagnosis of muscle and nerve disorders, besides that they are also used in engineering as an input for modelling of mechanical systems such as artificial limbs and also in prosthesis control engineering are used [3].

O. ÜLKİR, Department of Mechatronics Engineering, Technology Faculty, University of Marmara, Istanbul, Turkey, (e-mail: osman.ulkir@marmara.edu.tr). 

G. GÖKMEN, Department of Mechatronics Engineering, Technology Faculty, University of Marmara, Istanbul, Turkey, (e-mail: gokhang@marmara.edu.tr). 

E. KAPLANOĞLU, Department of Mechatronics Engineering, Technology Faculty, University of Marmara, Istanbul, Turkey, (e-mail: ekaplanoglu@marmara.edu.tr). 

Manuscript received May 16, 2017; accepted August 11, 2017.
DOI: [10.17694/bajece.337941](https://doi.org/10.17694/bajece.337941)

Because the first EMG controlled prosthetics had only one grasping ability, they were only able to do open-close functions or simple proportional control techniques [4]. The multi-grasp prosthetics used today require more complex control methods, and therefore, the need for classification of EMG signals used for control arises.

An EMG signal from a muscle which performs different functions has only one pattern for a specific function. This pattern contains information about the direction of motion and the action's speed. To successfully control the prosthetic, this patterns must be classified correctly. A pattern recognition system is made up of a few steps: data acquisition, feature extraction selection, determination of the classification algorithm, and designing the classifier [5].

For classification it is necessary to determine what type of EMG signal from the muscles is recorded as the result of the movement. For this, the EMG signal must be classified after filtering and the appropriate signal must be matched to the appropriate movement. There are many methods for classifier design such as heuristic approach, explicit approach, statistical approach, artificial neural networks, support vector machines and fuzzy approach. [6-9]. Fuzzy logic method is a more preferred technique for classifier because biological markers don't repeat and sometimes show features beyond expectations [6]. In the literature, fuzzy logic classification method is frequently used in prosthetic hand applications [9-11]. In such studies, it is aimed to improve the results by applying different self-extracting methods. In this study, three different qualitative inference methods were applied at the same time in order to successfully perform the classification process.

The aim of this study is to distinguish different gripping movements for prosthetic hand applications. To distinguish these movements, it is necessary to classify signals received with surface EMG electrodes. In this study, fuzzy logic classification method is used. In order for the fuzzy logic classification method to be successful, the attributes used as input signals must be well chosen.

II. METHODOLOGY

The analysis of EMG signal consist of several steps, such as data acquisition, pre-processing, feature extraction and classification algorithm [12]. Figure 1 shows the block diagram of classification method. The EMG signals, received from the data collection card from the two different muscle groups, were passed through the preprocessing process for their feature extraction. In this study, three feature extraction methods were used. Then the fuzzy logic based classification method was applied.

Be aware of the different meanings of the homophones “affect” (usually a verb) and “effect” (usually a noun), “complement” and “compliment,” “discreet” and “discrete,” “principal” (e.g., “principal investigator”) and “principle” (e.g., “principle of measurement”). Do not confuse “imply” and “infer.”

Prefixes such as “non,” “sub,” “micro,” “multi,” and “ultra” are not independent words; they should be joined to the words they modify, usually without a hyphen [2-4]. There is no period after the “et” in the Latin abbreviation “*et al.*” (it is also italicized). The abbreviation “i.e.,” means “that is,” and the abbreviation “e.g.,” means “for example” (these abbreviations are not italicized).

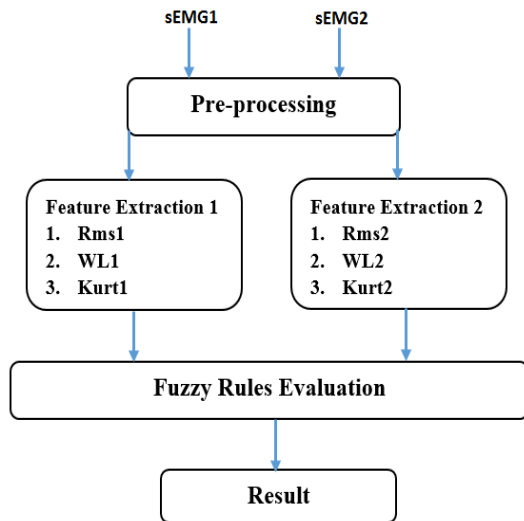


Fig.1. The block diagram of fuzzy logic classification method

A. sEMG Data Acquisition

EMG signals were obtained using surface electrodes by Bitalino EMG sensor. Four Ag-AgCl surface electrodes and one reference electrode is used, including two for each muscle. In this study, we focus on the wrist muscles which are the flexor carpi radialis (FCR) and extensor carpi radialis (ECR). These signals were given in Figure 3. Figure 2 shows the surface electrodes placed on the muscle surface.

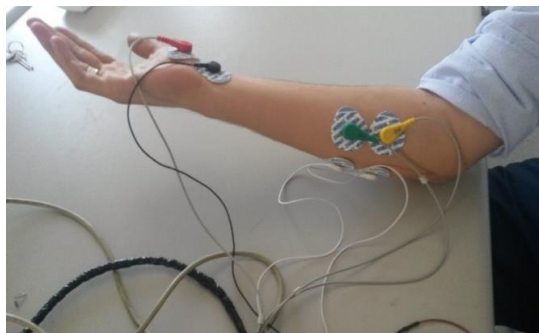


Fig.2. The position of the surface electrodes

The sampling frequency was set at 2 kHz using Arduino Uno programming card. EMG signals were recorded for 10 seconds, 5 seconds of flexion and 5 seconds of extension.

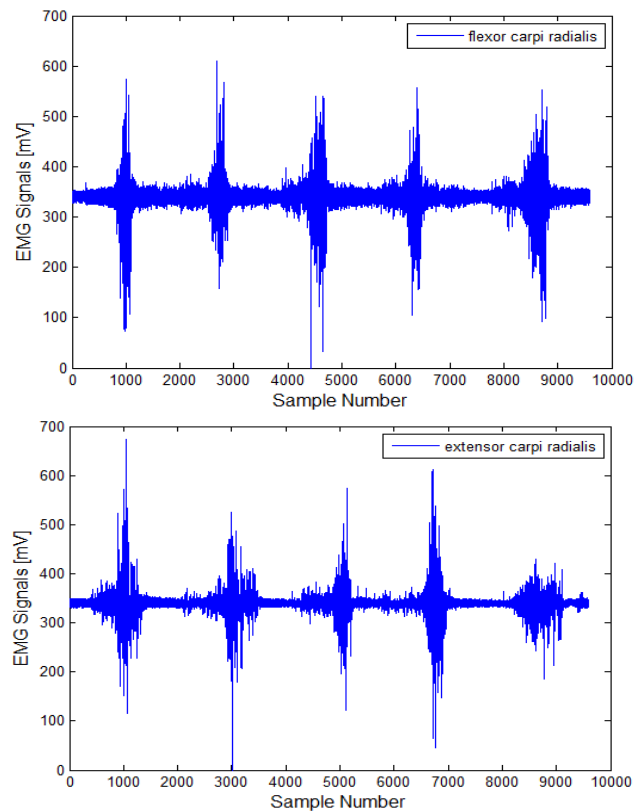


Fig.3. EMG signals

B. Features Extraction

EMG signals, which are a time series with a random number of elements, are not practical for classification. For this reason, the signal sequences must be matched to the vectors called the feature. In order to successfully classify EMG signals, the feature vectors must be well chosen. There are many feature extraction methods, such as mean absolute value, root mean square, variance etc. The advantages and disadvantages of each method are available.

To classify the EMG signal, it is necessary to extract the features from the signal. Since the recorded signal is measured by different time-dependent movements, it is necessary to analyze it at different intervals of time. For this, the EMG signal is divided into 256 data windows, and different feature extraction of each window is performed by three different methods. In this study, root mean square (RMS), waveform length (WL) and kurtosis (Kurt) methods were used for feature extraction. The analysis using these methods have shown repeatable and discrete model at different states of muscle contraction.

1) Root Mean Square (RMS)

It is a statistical method used to measure the magnitude of variable quantities. It is particularly useful in waves where the change is positive and negative. A continuously changing function can be calculated for the continuous value series. The root mean square method is calculated as in Equation 1.

$$RMS = \sqrt{\frac{1}{N} \sum_{n=1}^N x_n^2} \tag{1}$$

2) *Wavelet Length (WL)*

Waveform length represents wave cumulative length during time. WL is associated with pulse width, frequency and time. Waveform length method is calculated as shown in Equation 2.

$$WL = \sum_{n=1}^{N-1} |x_{n+1} - x_n| \quad (2)$$

3) *Kurtosis (Kurt)*

Kurtosis is a measure of data that provides information about the status of the peak. A near-zero kurtosis forms a near normal distribution. A positive value for the kurtosis is a sign of a more normal distribution. Kurtosis method is calculated as shown in Equation 3.

$$kurtosis = \frac{\sum_{i=1}^N (x_i - \bar{x})^4}{(N-1)\delta^4} \quad (3)$$

III. FUZZY LOGIC CLASSIFIER DESIGN

The fuzzy logic classifier is designed according to the connection between the start and end times of wrist flexion and extension movements. There are a total of 6 entry membership functions, 3 for each muscle in the system. These membership functions are obtained as a result of the feature extractions from the sEMG signals. The signals were analyzed using root mean square as the main method. Other features were applied waveform length and kurtosis. For the classifier design, the state of the contraction information is namely Start (S), Middle (M) and End (E) in determining the final output.

The fuzzy logic classifier has 6 inputs generated from feature extraction of the EMG signals and 1 input which is the states. The block diagram of the fuzzy logic classifier is shown in Figure 4 and Mamdani type fuzzy logic system was used. Triangular shapes are used for the membership function of the inputs and output. The centroid method is used for the defuzzification. The fuzzy logic classifier is developed using Matlab&Fuzzy Logic Toolbox. The system is tested using Simulink.

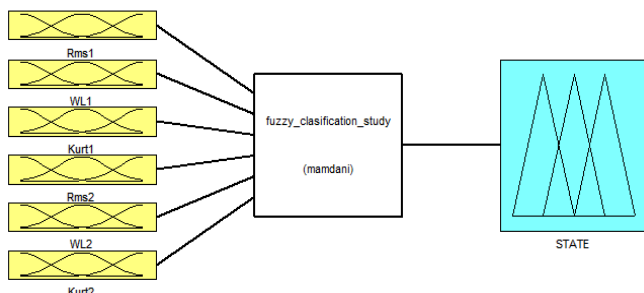


Fig.4. The block diagram of fuzzy logic classification system

The feature extraction of the sEMG signals gives 6 features. The features that are obtained in case of flexion of the wrist can be describes as Rms1, WL1, Kurt1. The features that are obtained in case of extension of the wrist can be describes as Rms2, WL2, Kurt2. For the input MF, the states of a contraction is used as the fuzzy set which are Start (S), Middle (M), End (E) and Relax (R). The output membership functions are expressed as State1 (S1), State2 (S2) and State3 (S3). Figure 5 shows input and output membership functions.

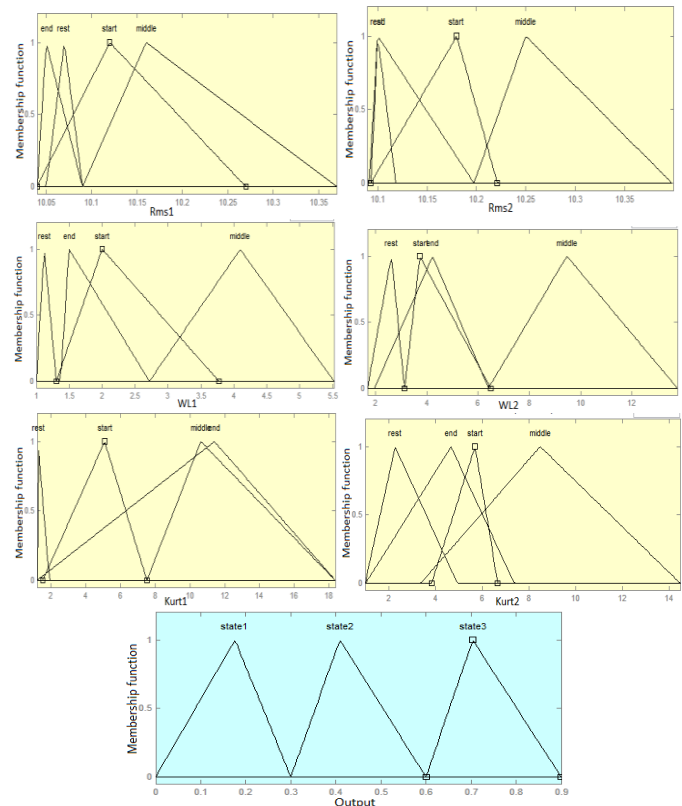


Fig.5. The membership functions of fuzzy logic classifier

Fuzzy logic classifier output states can be described as follows:

- 1) Wrist flexion of the Start – S3
- 2) Wrist flexion of the Middle – S2
- 3) Wrist flexion of the End – S1
- 4) Wrist extension of the Start – S1
- 5) Wrist extension of the Middle – S2
- 6) Wrist extension of the End – S3

The rules are given in Table 1. The first and second rule is only applied to wrist flexion, rule 5 and 6 apply to wrist extension and rule 3 and 4 apply to wrist flexion/extension. Expert guidance was used while plotting the rule table. The features was expressed Rms1 (A1), WL1 (B1), Kurt1 (C1), Rms2 (A2), WL2 (B2) and Kurt2 (C2) in Table 1.

TABLE I
FUZZY LOGIC CLASSIFIER RULE TABLE

Rule	A1	B1	C1	A2	B2	C2	THEN	State
1	S	S	S	R	R	R	THEN	S3
2	S	S	S	E	E	E	THEN	S3
3	M	M	M	R	R	R	THEN	S2
4	R	R	R	M	M	M	THEN	S2
5	E	E	E	S	S	S	THEN	S1
6	R	R	R	S	S	S	THEN	S1

IV. RESULTS AND ANALYSIS

Feature extraction signals which used as input membership functions in fuzzy logic classification and classification results are shown in Figure 6. EMG signals obtained from flexor carpi radialis muscle were obtained as follows: Rms1, WL1 and Kurt1. EMG signals obtained from extensor carpi radialis muscle were obtained as follows: Rms2, WL2 and Kurt2.

According to the output graph obtained, the fuzzy logic classifier classifies the EMG signals for three different states (S1, S2, S3).

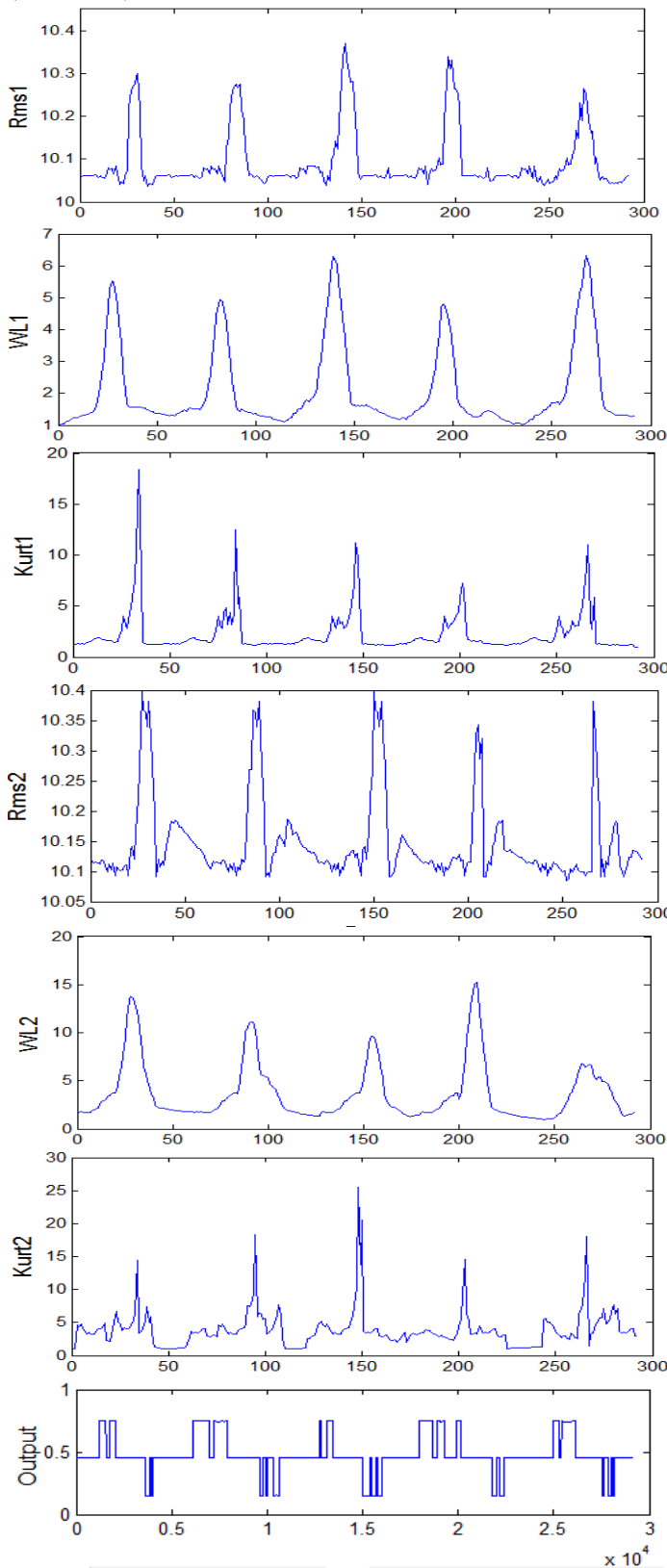


Fig.6. The result of fuzzy logic classifier

The classifier outputs are presented in detail in Figure 7 for initial contraction. The wrist was selected as S3 (0.6-0.9) for the beginning of contraction, S2 (0.3-0.6) for contraction center and

S1 (0-0.3) for the ending of contraction.

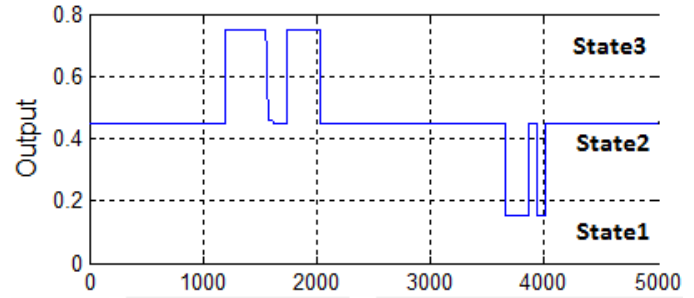


Fig.7. The result of classification

The accuracy (in%) of the data obtained as a result of the data obtained as a result of the classification are shown in Table 2.

TABLE II
THE ACCURACY (IN %) OF FUZZY LOGIC CLASSIFIER

Wrist Flexion/Extension	% Classification success
Start	88.84
Middle	99.85
End	90.67
Average success	93.12

V. CONCLUSION

In order to understand contraction state movement by using gripping movements, state-based fuzzy logic classification method is used. Conditions are expressed as the beginning, middle and end of the contraction. In this study, the feature extraction and classification of EMG signals received with two channel surface electrodes has been successfully accomplished. As a result of the classification, the wrist flexion / extension times of the user have been determined.

The most important reason of preferring the fuzzy logic classification method is that it does not require any training and its application is simple. A prosthesis developed with the fuzzy logic classification method can easily be transferred from one person to another.

REFERENCES

- [1] M. Diakides, J.D. Bronzino, D.R. Peterson, "Medical Infrared *Imaging: Principles and Practices*", CRC press, 2012.
- [2] E. Criswell, "Cram's introduction to surface electromyography", Jones & Bartlett Publishers, 2010.
- [3] J. He, D. Zhang, N. Jiang, X. Sheng, D. Farina, X. Zhu, "User adaptation in long-term, open-loop myoelectric training: implications for EMG pattern recognition in prosthesis control", *Journal of Neural Engineering*, vol. 12, no. 4, 2015.
- [4] K. Englehart, B. Hudgins, P.A. Parker, M. Stevenson, "Classification of the myoelectric signal using time-frequency based representations", *Medical Engineering & Physics*, vol. 21, no. 6, pp. 431-438, 1999.
- [5] X. Chen, D. Zhang, X. Zhu, "Application of a self-enhancing classification method to electromyography pattern recognition for multifunctional prosthesis control", *Journal of Neuroengineering and Rehabilitation*, vol. 10, no. 1, 2013.
- [6] H.J. Fariman, S.A. Ahmad, M.H. Marhaba, M.A.J. Ghasab, P.H. Chappell, "Simple and computationally efficient movement classification approach for EMG-controlled prosthetic hand: ANFIS vs.

- Artificial Neural Network”, *Intelligent Automation & Soft Computing*, vol. 21, no. 4, pp. 559-573, 2015.
- [7] M. Ariyanto, W. Caesarendra, K.A. Mustaqim, M. Irfan, J.A. Pakpahan, J.D. Setiawan, A.R. Winoto, “Finger movement pattern recognition method using artificial neural network based on electromyography (EMG) sensor”, in *Automation, Cognitive Science, Optics, Micro Electro-Mechanical System, and Information Technology (ICACOMIT)*, 2015, International Conference, pp. 12-17.
- [8] Q. Wu, J.F. Mao, C.F. Wei, S. Fu, R. Law, L. Ding, C.H. Yang, “Hybrid BF-PSO and fuzzy support vector machine for diagnosis of fatigue status using EMG signal features”, *Neurocomputing*, vol. 173, no. 3, pp. 483-500, 2016.
- [9] F. Rajablou, M. Ghanbari, “Identifying the condition of arm through classification of EMG signals by the use of hybrid trained adaptive neural fuzzy inference systems (ANFIS)”, *Bulletin of the Georgian National Academy of Sciences*, vol. 9, no. 2, pp. 404-410, 2015.
- [10] A. Subasi, “Classification of EMG signals using combined features and soft computing techniques”, *Applied soft Computing*, vol. 12, no. 8, pp. 2188-2198, 2012.
- [11] H.B. Xie, H. Huang, J. Wu, L. Liu, “A comparative study of surface EMG classification by fuzzy relevance vector machine and fuzzy support vector machine”, *Physiological Measurement*, vol. 36, no. 2, pp. 191-206, 2015.
- [12] P. Konrad, “The abc of EMG: A practical introduction to kinesiological electromyography”, Noraxon Inc., 2005.

BIOGRAPHIES



Osman ÜLKİR was born in Hatay, Turkey. He graduated from Kocaeli University, Engineering Faculty, Kocaeli, in 2012, and received M. Sc. degree from Marmara University, Institute of Pure and Applied Sciences, in İstanbul, Turkey, in 2015. He has been started Ph. D. studying in department of Mechatronics Engineering, Marmara University, Institute of Pure and Applied Sciences in 2015. He is currently working as a research assistant in mechatronics engineering department in technology faculty at Marmara University. His special field of interest Biomechatronics systems, signal processing, lower limb orthosis, and data-driven predictive control.



Gökhan GÖKMEN was born in Mersin, Turkey 1974. He received B.S, M.S and PhD degrees from Marmara University, İstanbul, Turkey. He has been working as an associate professor at Marmara University. His current interests are measurement method, signal processing techniques, vocational education.



Erkan KAPLANOĞLU received the bachelor's degree from Marmara University Electric Department, in 1996. He completed his M. Sc. and Ph. D. thesis at Computer Control Department of Marmara University, Institute for Graduate Studies in Pure and Applied Sciences, in 2000 and 2006, respectively. In March 2014, Dr. Kaplanoğlu became Associate Professor at Marmara University, Mechatronics Department. He has been awarded YGGDRASIL Award (Young Guest Doctoral Researchers in Norway) in 2010. He worked as research assistant professor at Department of Mechanical Engineering Vanderbilt University Faculty of Engineering Nashville/TN, USA from 2011 to 2012. His research areas are Biomechatronics systems, Lower limb Prosthesis, modeling, identification and control. Multivariable, Model Predictive Control, Data Acquisition Systems.

Publication Ethics

The journal publishes original papers in the extensive field of Electrical-electronics and Computer engineering. To that end, it is essential that all who participate in producing the journal conduct themselves as authors, reviewers, editors, and publishers in accord with the highest level of professional ethics and standards. Plagiarism or self-plagiarism constitutes unethical scientific behavior and is never acceptable.

By submitting a manuscript to this journal, each author explicitly confirms that the manuscript meets the highest ethical standards for authors and coauthors

The undersigned hereby assign(s) to *Balkan Journal of Electrical & Computer Engineering* (BAJECE) copyright ownership in the above Paper, effective if and when the Paper is accepted for publication by BAJECE and to the extent transferable under applicable national law. This assignment gives BAJECE the right to register copyright to the Paper in its name as claimant and to publish the Paper in any print or electronic medium.

Authors, or their employers in the case of works made for hire, retain the following rights:

1. All proprietary rights other than copyright, including patent rights.
2. The right to make and distribute copies of the Paper for internal purposes.
3. The right to use the material for lecture or classroom purposes.
4. The right to prepare derivative publications based on the Paper, including books or book chapters, journal papers, and magazine articles, provided that publication of a derivative work occurs subsequent to the official date of publication by BAJECE.
5. The right to post an author-prepared version or an official version (preferred version) of the published paper on an internal or external server controlled exclusively by the author/employer, provided that (a) such posting is noncommercial in nature and the paper is made available to users without charge; (b) a copyright notice and full citation appear with the paper, and (c) a link to BAJECE's official online version of the abstract is provided using the DOI (Document Object Identifier) link.



ISSN: 2147- 284X
Vol: 5
No:2
Year: September 2017

CONTENTS

- A. Bosakova-Ardenska**, One Approach for Parallel Algorithms Representation, ... 30-33
- H. Ozkan**, Rapid Diagnostic Lateral Flow Strip Test Reader, 34-39
- E. Oguz, Y. Oğuz and H.Çimen**, Simulation and Power Flow Control Using Switching's Method of Isolated Wind-Solar Hybrid Power Generation System with Battery Storage, 40-49
- B. Fincan, M. Yilmaz, A. Goynusen, and K. Erenay**, Design and Optimization of a High Power Density and Efficiency Boost PFC,..... 50-59
- D. Taskin**, Design of Bluetooth Low Energy Based Indoor Positioning System, 60-65
- F. Bulut, and S. Osmani**, Scene Change Detection using Different Color Pallets and Performance Comparison, 66-72
- M. Aydın, and G. Erdemir**, An Object Detection and Identification System for a Mobile Robot Control, 73-76
- J. A. Corea-Araujo, G. Guerra, J. A. Martínez-Velasco, and F. González-Molina**, Generation of Bifurcation Diagrams for Ferroresonance Characterization Using Parallel Computing,.....77-85
- B.B. Alagoz**, A Note on Commensurate-Order Characteristic Root Equivalency Class of Linear Time Invariant Systems,..... 86-96
- O. Ülker, G. Gökmen and E. Kaplanoğlu**, Emg Signal Classification Using Fuzzy Logic, 97-101

BALKAN JOURNAL OF ELECTRICAL & COMPUTER ENGINEERING

(An International Peer Reviewed, Indexed and Open Access Journal)

Contact

Istanbul Technical University
Department of Electrical Engineering,
Ayazaga Campus, Maslak, Istanbul-Turkey

Web: <https://www.bajece.com>
<http://dergipark.gov.tr/bajece>
e-mail: editor@bajece.com

